1996

Design Optimization of Indium-Gallium-Arsenide-Phosphide Multi-Quantum Well Electroabsorbtion Modulators

Gregory H. Ames
University of Rhode Island

DESIGN OPTIMIZATION OF INDIUM-GALLIUM-ARSENIDE-PHOSPHIDE MULTI-QUANTUM WELL ELECTROABSORPTION MODULATORS

BY

GREGORY H. AMES

A DISSERTATION SUBMITTED IN PARTIAL FULFILLMENT OF THE

REQUIREMENTS FOR THE DEGREE OF

DOCTOR OF PHILOSOPHY

IN

ELECTRICAL ENGINEERING

MAJOR PROFESSOR: PROFESSOR GABRIEL LENGYEL

UNIVERSITY OF RHODE ISLAND
1996

DOCTOR OF PHILOSOPHY DISSERTATION

OF

GREGORY H. AMES

Approved:

Dissertation Committee

Major Professor:

DEAN OF GRADUATE SCHOOL

UNIVERSITY OF RHODE ISLAND
1996

ABSTRACT

A theoretical analysis of the performance of InGaAsP multi-quantum well electro-absorption modulators is presented. A comprehensive model of the quantum confined Stark effect is described to determine the absorption and index change spectra versus applied field. This model is based on previously developed models for GaAs/AlGaAs structures, but includes improvements in the handling of exciton line broadening and the variation of exciton oscillator strength with field.

The analysis of line broadening due to composition fluctuations is presented, revealing a previously neglected factor. Two numerical methods for calculating the line broadening, based on the resonant tunneling method, are presented and compared. A theoretical analysis of barrier composition fluctuation broadening is presented, which separately calculates the contribution from the electron and hole and their different penetration into opposite barriers when field is applied. The total linewidth model is compared with published linewidth measurements.

Theoretical results of absorption spectra versus applied field were compared with two sets of experimental measurements. With appropriate choice of several unknown factors related to the quantum well fabrication quality, the theory and experimental data were well matched in shape of the absorption edge, shift of the edge with field, and decrease in the exciton oscillator strength with field.

The theoretical model was used to optimize modulator device design, through the calculation of thousands of design combinations of device length, well number, well width, barrier width, well composition, and applied voltage. For each design,

bandwidth, contrast ratio, loss, detuning, and several chirp parameters were calculated. It is shown that long distance transmission performance may be optimized with negative values of a specific chirp parameter called the 3dB Henry factor. Modulator design can be optimized for such values by operating close to the exciton and accepting high optical loss. Loss may be reduced by optimum choice of device length, well number, and barrier width, while it can be compensated by an optical amplifier.

The optimum design changes considerably when the requirement for negative chirp is eliminated. Such designs use more quantum wells and tune the device further from the exciton. Finally, the model provides a means to choose the optimum well width.

ACKNOWLEDGEMENT

Among the many people who supported this dissertation work, I would like to thank the staff of the Siemens Research Laboratory for permitting use of the experimental data on modulator devices fabricated at Siemens. I wish to thank the faculty of the Electrical Engineering Department of the University of Rhode Island and my co-workers at the Naval Undersea Warfare Center in New London for their encouragement during my graduate studies. I especially wish to thank my major professor, Dr. Gabriel Lengyel, for advice, guidance, encouragement, and the generous gift of his time and friendship. Finally, I wish to acknowledge my wife, Jan Ames, for loving support and patience.

PREFACE

There has been considerable interest in the development of external modulator devices for optical communications. The conventional methods based on direct modulation of a diode laser's drive current tend to be limited by the laser's frequency chirp associated with the modulation. This chirp results in system bandwidth limitations through pulse dispersion in long fiber optic links. With external modulation the laser is operated in a continuous output mode and modulation is provided by an external electro-optic modulator device. Laser chirp is eliminated and the system is limited instead by the lesser chirp introduced by the modulator. Elimination of the modulator function also allows optimization of the laser design for other performance aspects.

A key contender for the role of external modulator is the multiple quantum well (MQW) electro-absorption modulators based on the quantum confined Stark effect (QCSE). These devices have demonstrated high data rate capability and sufficient contrast ratio and loss performance.[1-3] Electro-absorption modulators operate at a wavelength which is in the transmissive wavelength region above the device's absorption edge in the "on" state. In the "off" state a voltage is applied which shifts the absorption edge and results in high absorption at the operating wavelength. With the QCSE the absorption edge of the semiconductor is considerably sharper or more abrupt with wavelength due to excitonic absorption. In a bulk semiconductor, Wannier excitons consist of an electron in the conduction band and a hole in the valence band which are bound together through their Coulomb interaction to form a state similar to a hydrogen atom. In a bulk semiconductor the excitons are seen only at low temperature and quickly disassociate with applied field. In a quantum well, the electrons and holes are confined in close proximity in one direction in the quantum well. The excitons persist at room

termperature and with high fields applied perpendicular to the quantum well layers. As field is applied, the shape of the potential wells for electron and hole changes and the sub-band levels within the well change. The result is that the energy of the exciton absorption shifts with applied field. This effect is known as the quantum confined Stark effect and it results in large movements of a sharp absorption edge, both aspects being conducive to good modulator performance.

Historically, these modulators were first developed in the GaAs/AlGaAs material system for use at wavelengths near 0.8 μm.[4-5] Given the importance of the low loss and low dispersion 1.3 μm and 1.55 μm communications windows in optical fiber, MQW modulator development for those wavelengths is necessary. The wavelength of absorption in such devices is a function of the semiconductor's bandgap and thus different material systems are required for operation at 1.3 and 1.55 μm. The quaternary $In_{1-x}Ga_xAs_yP_{1-y}$ system is a major contender.

Quaternary semiconductor systems give additional degrees of design freedom, allowing separate optimization of both the well width and the well/barrier compositions. Initial work by Nojima and Wakita[6] indicated that large well width leads to large exciton shift with field but decreased oscillator strength. It is very important to optimize this tradeoff as well as other tradeoffs of the various design parameters and performance factors. The potential appears to exist to greatly improve performance of InGaAsP MQW modulators through design optimization.

An adequate theoretical model of the basic electroabsorption properties in InGaAsP quantum wells is required as a basis for this optimization. The quantum confined Stark effect was first described in the GaAs/AlGaAs system by Miller et al. [4,5] Since that time the theoretical treatment of the electroabsorption in that material system has been extensively treated [7-17] and the best models describe the experimentally observed behavior quite well. In contrast, there have been few experimental measurements of InGaAsP MQW electroabsorption[18-21] and less work to theoretically

explain performance or to seek to optimize device performance.[6,22-23] Qualitatively, the electroabsorption characteristics of InGaAsP MQWs are quite different from those of GaAs/AlGaAs MQWs and further from optimum. Exciton absorption peaks in InGaAsP are less prominent and fade or broaden quickly with field. Exciton linewidths are increased, giving a less sharp absorption edge. Modulator performance depends on the absorption change which can be achieved with a given voltage. It is enhanced by prominent, sharp exciton peaks. The observed broadening and fading of InGaAsP excitons leads to reduced, though still usable, performance. It is therefore necessary to explore the applicability of those theoretical models developed for GaAs/AlGaAs to the InGaAsP system and to investigate modifications necessary to account for differences between the two systems.

The objective of this work has been two-fold. The first objective has been to develop a theoretical model of electroabsorption in InGaAsP MQW modulators to serve as the basis for design optimization of such modulators. The goal has been to develop a model which balances the requirement for accurate reproduction of experimental measurements of the exciton peak and absorption edge, with the requirement for computational simplicity to enable multi-parameter device design optimization. The basic approach has been to make use of previous theoretical work done for the GaAs/AlGaAs system, extending or modifying it as necessary to account for differences with the InGaAsP system. Results have been compared to several published experimental studies of InGaAsP devices and unpublished measurements available from Siemens researchers.

The second objective is to use the theoretical model as part of a multiple parameter device design optimization. To date there has been very little published work to optimize device design and that which has appeared has made use of overly simplistic models for the electroabsorption.[6,16,22-25] In addition, previous device optimization studies have focused on a limited number of performance parameters, usually some combination of bandwidth, drive voltage, loss, and extinction ratio. It is common to form composite

figures of merit from some of these performance parameters and to optimize the design for these figures of merit. However, when the figures of merit leave out key performance parameters or place undo emphasis on some parameters, the implications of the design optimization become misleading. Two examples are illustrative. The use of fiber optic amplifiers allows higher modulator insertion loss in some important applications. Figures of merit which over-emphasize low loss may lead to wrong design choices. Also, there has been no published study which considered the modulator chirp performance as part of the device optimization, yet chirp performance is a key parameter in long distance, high bit rate communications and is the primary reason driving the use of external modulators in the first place. The work presented herein considers device optimization across a full range of performance parameters, including chirp performance.

Chapter 1 presents a theoretical description of the unbounded conduction and valence band states and the exciton states in a quantum well (QW). Chapter 2 develops the theory for optical absorption associated with electron transitions between these states. Both continuum absorption due to unbounded states and exciton absorption is treated. Chapter 3 deals with the theoretical treatment of the various mechanisms responsible for line broadening in the QW electroabsorption. Chapter 4 combines results of the previous three chapters into a model of the absorption spectra and compares it with available experimental absorption spectra. Chapter 5 presents the model of the full MQW modulator device. Chapter 6 presents and discusses results of a multi-parameter design optimization. This program considered over 1400 design combinations at a time and evaluated four performance parameters.

TABLE OF CONTENTS

LIST OF TABLES

LIST OF FIGURES

CHAPTER 1

QUANTUM WELL STATES

Bloch States

Optical absorption occurs in a QW when an electron is excited from a valence band to the conduction band while absorbing an incident photon. Such transitions may occur between unbounded electron and hole states or involve transitions with excitons comprised of bound pairs of electron and hole states. The starting point for describing both is the Bloch wave solutions for the Schrödinger equation of an electron in an isotroptic infinite periodic crystal. It is well known that these solutions are of the Bloch wave form:

$$\Psi_B(\mathbf{k},\mathbf{r}) = u_B(\mathbf{k},\mathbf{r})e^{i(\mathbf{k}\cdot\mathbf{r})} \tag{1.1}$$

The solutions are labeled by the band index B and wavevector **k**. The Bloch functions u have the characteristic that they are periodic with the crystal lattice. Conduction and valence band Bloch functions are orthogonal and the Bloch functions are normalized:

$$\langle u|u\rangle = \frac{1}{V_{uc}} \int_{\text{unit cell}} u^* u d^3\mathbf{r} = 1 \tag{1.2}$$

where V_{uc} is the unit cell volume.

QW Single Particle States

In the QW structure, the particles are partially confined and their wavefunctions localized. The individual particles are confined in the growth (henceforward the z) direction by the potential difference between the well and barrier, giving localization in

the z direction. The localized functions may be described by a linear combination of the Bloch wave functions. In the general case of full three dimensional localization:

$$\Psi_B(\mathbf{k},\mathbf{r}) = \int D_B(\mathbf{k}) e^{i\mathbf{k}\cdot\mathbf{r}} u_B(\mathbf{k},\mathbf{r}) d^3\mathbf{k} \tag{1.3}$$

The various $D_B(\mathbf{k})$ are the coefficients of this expansion.

When localization is only in the z direction, the functions may be expressed as:

$$\Psi_B(\mathbf{k},\mathbf{r}) = e^{i\mathbf{k}_\parallel\cdot\mathbf{r}_\parallel} u_B(\mathbf{k}_\parallel,\mathbf{r}_\parallel) \int D_B(k_z) e^{ik_z\cdot z} u_B(k_z,z) dk_z \tag{1.4}$$

where $\mathbf{r}_\parallel$ and $\mathbf{k}_\parallel$ are the position vector and wavevector in the x,y plane of the QW layer, respectively. In the effective mass or envelope function approximation, a major assumption is that the Bloch functions are not strong functions of $\mathbf{k}$ and can be approximated by their value at the band edge $\mathbf{k}$=0. Thus:

$$\begin{aligned}\Psi_B &\approx e^{i\mathbf{k}_\parallel\cdot\mathbf{r}_\parallel} u_B(0,\mathbf{r}) \int D_B(k_z) e^{ik_z\cdot z} dk_z \\ &= e^{i\mathbf{k}_\parallel\cdot\mathbf{r}_\parallel} u_B(0,\mathbf{r}) \Psi_B^n(z) \\ &= u_B(0,\mathbf{r}) F_B(\mathbf{r})\end{aligned} \tag{1.5}$$

The full wavefunction is described as the product of the band edge Bloch functions and the envelope wavefunction $F_B(\mathbf{r})$. The envelope function is the solution of the effective mass equation rather than the full Schrödinger equation :

$$(H_{KE} + V) F_B(\mathbf{r}) = E_B F_B(\mathbf{r}) \tag{1.6}$$

Since absorption near the band edge is of primary interest, parabolic dispersion relationships are usually assumed for each band.

$$H_{KE} = E_{B0} - \frac{\hbar^2}{2m_B^*}\nabla^2 \tag{1.7}$$

Here m_B^* is the effective mass for band B, $E_{B,0}$ is the band edge energy, and V is the macroscopic potential (which may include the potential due to any applied field but doesn't include the lattice potential). For the MQW, the envelope function $\Psi_B^n(z)$ in the z direction is just the solution of the one dimensional "particle in a box" problem. V is the confining potential of the well defined by the bandgap difference between barrier and well and the splitting of that difference between conduction and valence band. It may also include any field applied in the z direction. The splitting in InGaAsP is often assumed to

be 60%:40% between valence and conduction band, respectively. The envelope function is labeled with the band index B and the subband index n labeling the various solutions of the "particle in a box" problem.

The InGaAsP valence band structure is complicated by a light and heavy hole band degenerate at zone center, and the split off band as shown in Figure 1.1. The exciton binding energy is much less than the energy gap to the split off band and this band is usually ignored. The reduction in symmetry in the QW and the band discontinuities lifts the degeneracy of the light and heavy hole bands at zone center. Provided the wells are sufficiently narrow, the subband separation is greater than the exciton binding energy and there is very little coupling between bands. In this case the heavy and light hole bands can be treated separately. Several authors have included band coupling in more complicated theoretical treatments.[26-28] Their results showed that including such effects gave only small corrections, these corrections becoming negligible as field was applied. In what follows, coupling between bands is ignored and each band can be solved separately.

Resonant Tunneling Method (RTM)

It is necessary to calculate the electron and hole energy subband levels in the one dimensional quantum wells both with and without applied field. Associated with this is the task of determining the electron and hole z direction envelope wavefunctions. Numerous techniques have been used for this purpose, including perturbation methods[17], variational methods[10], exact Airy function solutions[12,29], infinite potential well solutions with modified effective well width[5], and Monte Carlo methods[14,30]. One of the most useful is the resonant tunneling method (RTM)[31] in that it easily gives both energy levels and wavefunctions, it can handle arbitrary potential profiles, it easily incorporates the effective mass changes between well and barrier, and it gives the tunneling through the barriers.

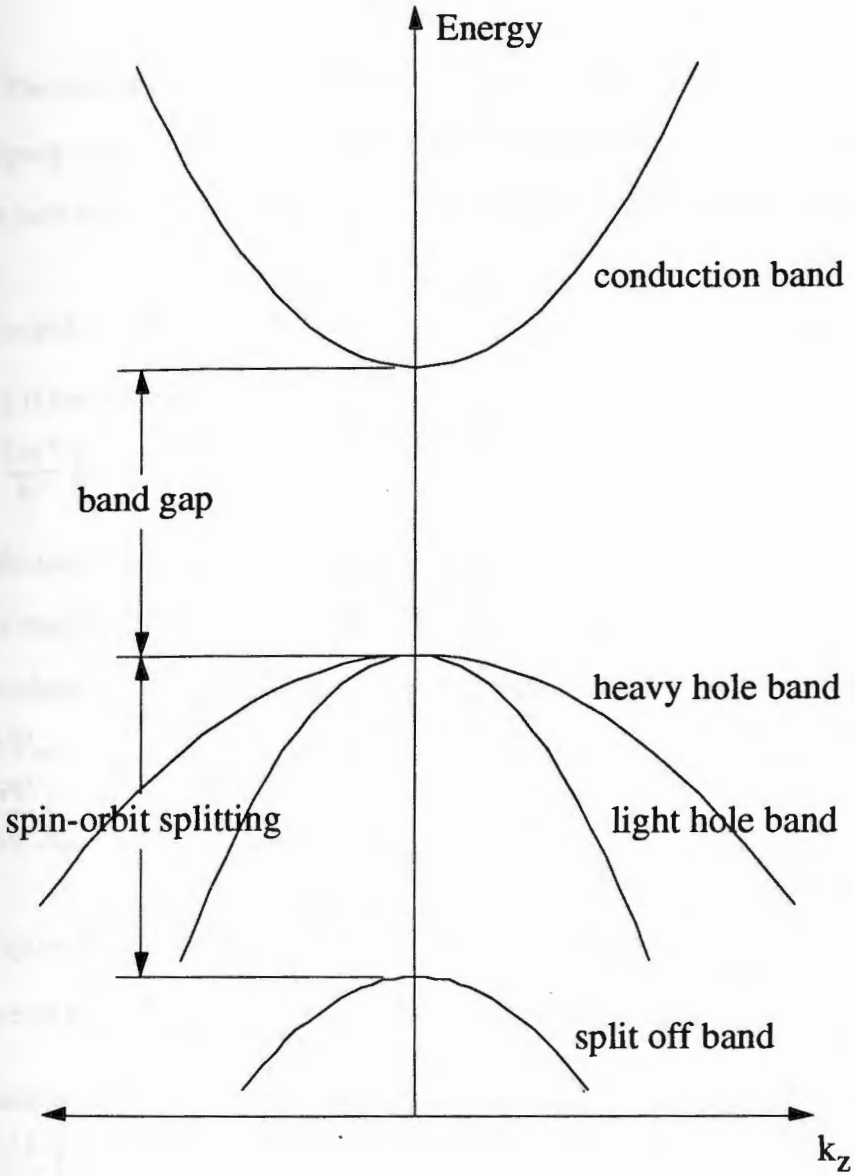

Figure 1.1. Sketch of the band structure in bulk InGaAsP near the Γ point (**k**=0).

The resonant tunneling method is used within the effective mass approximation. The sloping potential due to an applied field is approximated by small steps as in Figure 1.2. In each step the particle envelope wavefunction is written in terms of plane wave states:

$$\Psi = A\exp(kz) + B\exp(-kz) \tag{1.8}$$

where k is the complex wave number:

$$k = \left[\left(\frac{2m^*}{\hbar^2}\right)(V_0 - E)\right]^{1/2} \tag{1.9}$$

m^* is the particle effective mass, V_0 is the potential, and E is the total particle energy. A transfer matrix is derived to describe transmission across a potential step by requiring that the wavefunction and probability flux on each side matches at the interface. At x=p:

$$\Psi_{left} = \Psi_{right} \tag{1.10}$$

$$\left(\frac{1}{m^*}\frac{\partial\Psi}{\partial z}\right)_{left} = \left(\frac{1}{m^{*'}}\frac{\partial\Psi}{\partial z}\right)_{right} \tag{1.11}$$

Thus:

$$\begin{aligned} &A\exp(kp) + B\exp(-kp) = C\exp(k'p) + D\exp(-k'p) \\ &\frac{k}{m^*}\left(A\exp(kp) - B\exp(-kp)\right) = \frac{k'}{m^{*'}}\left(C\exp(k'p) - D\exp(-k'p)\right) \end{aligned} \tag{1.12}$$

This leads to the transfer matrix equation:

$$\begin{pmatrix} A \\ B \end{pmatrix} = \left(\frac{1}{2}\right)\begin{pmatrix} \alpha\exp(p(k'-k)) & \beta\exp(-p(k'+k)) \\ \beta\exp(p(k'+k)) & \alpha\exp(-p(k'-k)) \end{pmatrix}\begin{pmatrix} C \\ D \end{pmatrix} \tag{1.13}$$

where $\alpha = 1 + (m^* k'/m^{*'} k)$ and $\beta = 1 - (m^* k'/m^{*'} k)$.

To find the subband energy levels one determines the transmission of the structure versus energy for a wave traveling from left to right. However, one starts with the exiting wave (C,D)=(1,0) at the far right and propagates backward through the structure from right to left using the transfer matrices at each step. Wavefunction coefficients (A,B) are obtained at each step. The transmission coefficient for the structure is:

$$T = \left|\frac{1}{A_{left}}\right|^2 \left|\frac{k_{right}}{k_{left}}\right| \left(\frac{m^*_{left}}{m^*_{right}}\right) \tag{1.14}$$

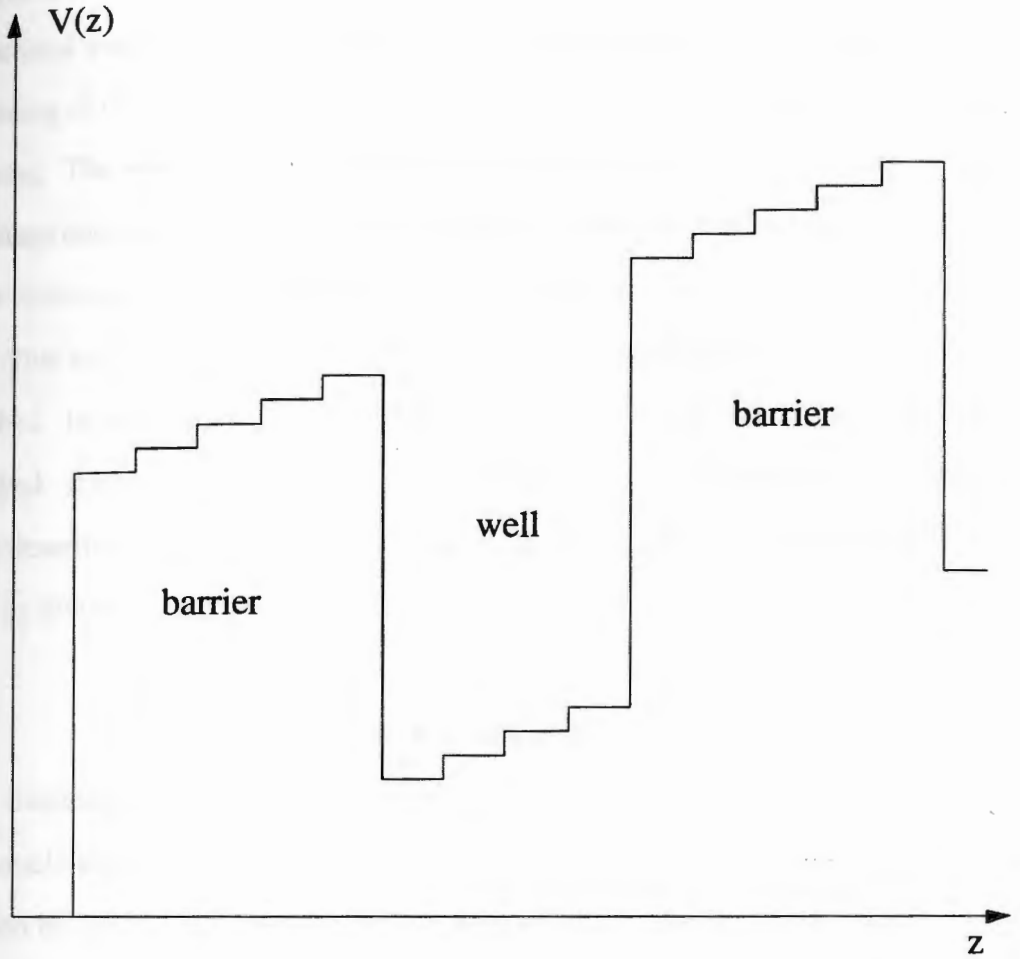

Figure 1.2. Representation of the quantum well potential with an applied electric field in the resonant tunneling method. Step size has been exaggerated for clarity. The actual number of steps is much greater.

where left and right refer to far sides of the entire structure. This calculation is performed for various particle energies E and a plot of transmission vs. energy is obtained as in Figure 1.3. The resonant peaks in this plot correspond to the subband energy levels of the quantum well, labeled by the index n. Various step sizes were used and the energy levels converged on fixed values as the step size was reduced. Steps of 5 angstroms were found to be sufficient to give accurate subband energy levels. At the resonant

energy, the coefficients (A,B) at each step in the structure give the particle one dimensional wavefunction as in Figure 1.4. Finally, the method also gives the broadening of the energy level due to the limited lifetime of the particle in the well due to tunneling. The resonant peak is approximately Lorentzian in shape as seen in Figure 1.5. This shape corresponds to the tunneling induced broadening of the energy level. As the barrier thickness is reduced and tunneling is increased, the resonance becomes broader.

This method may be utilized for multiple wells and coupling between wells is well described. In the rest of this work, however, only calculations with single wells will be employed. It is assumed that coupling is sufficiently low that the MQW characteristics can be described by calculations for a single well. The tunneling linewidth will serve as a check on this assumption.

QW Exciton States

Excitons are bound pairs of electron and hole states. The exciton states are thus two particle states. In the exciton, the wavefunctions are further localized in the x,y direction by their mutual interaction. In the effective mass approximation the Schrödinger-like equation for the envelope wavefunction of the exciton is written by combining the equations for electron and hole and including the Coulomb interaction.[32] As noted before, the heavy and light holes will be treated as separate exciton systems. It is assumed that the barriers are thick enough that coupling is negligible between neighboring wells and the MQW can be described by considering the action of a single well. For the electron:

$$(H_{KEe} + V_e - eF_\perp z_e)\Psi_e(\mathbf{r_e}) = E_c\Psi_e(\mathbf{r_e}) \tag{1.15}$$

For the hole:

$$(H_{KEh} + V_h + eF_\perp z_h)\Psi_h(\mathbf{r_h}) = -E_v\Psi_h(\mathbf{r_h}) \tag{1.16}$$

Since absorption near the band edge is of interest parabolic dispersion relationships are assumed for each band.

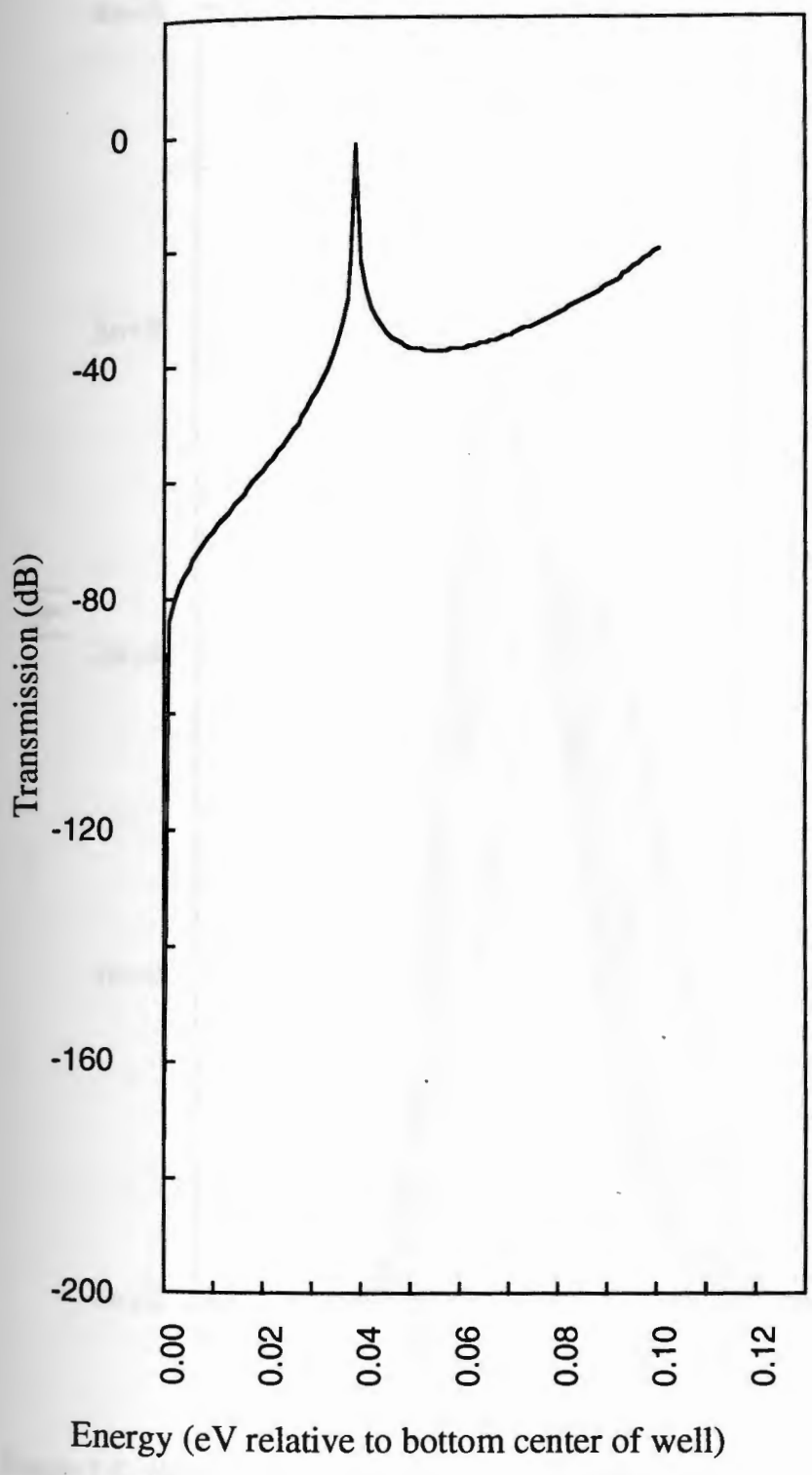

Figure 1.3. Typical RTM transmission plot for an electron in a quantum well.

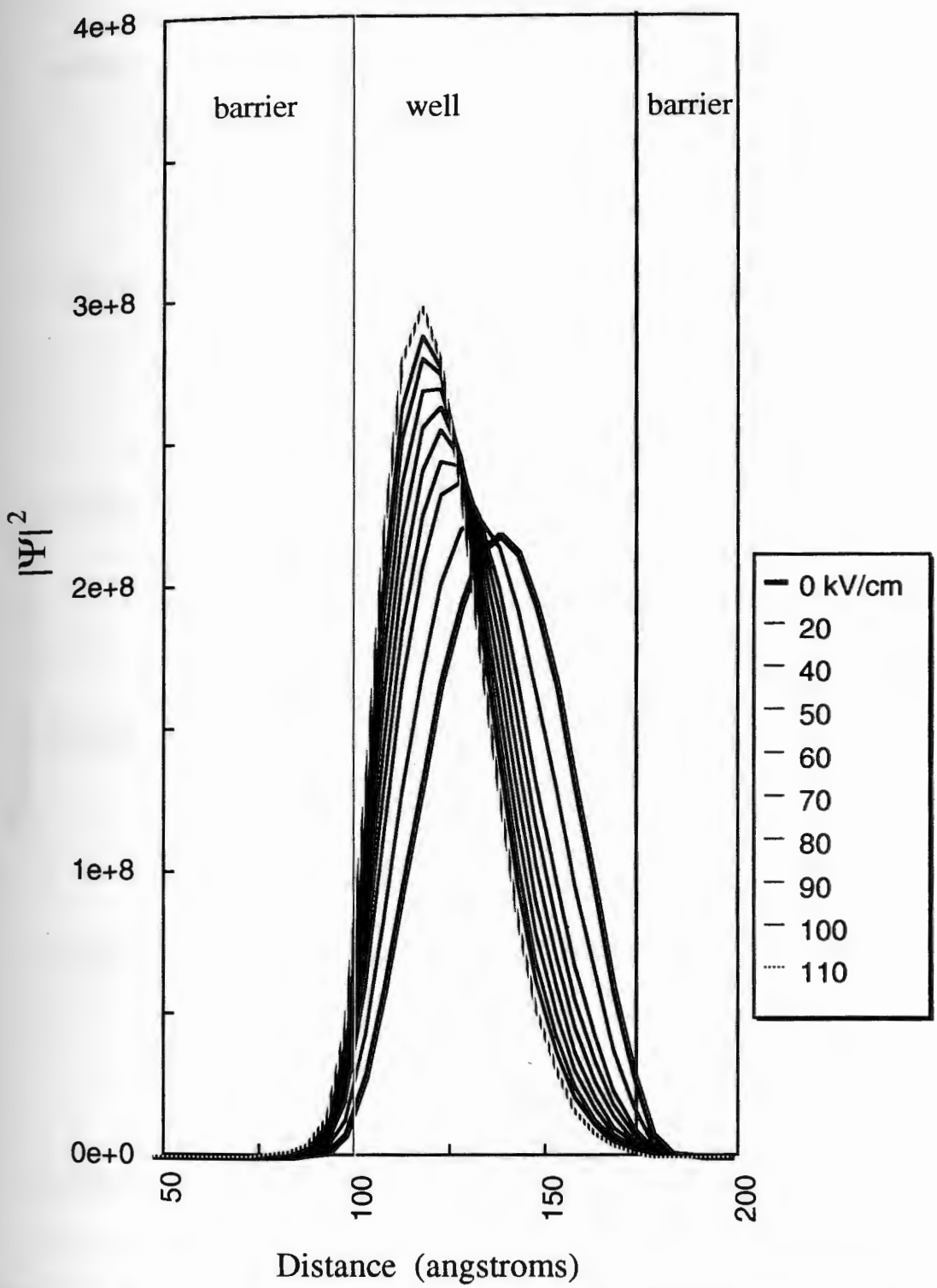

Figure 1.4. Heavy hole wavefunction in a QW versus applied field. Well width is 75 angstroms. Barrier width is 100 angstroms. Well depth is 150.8 meV.

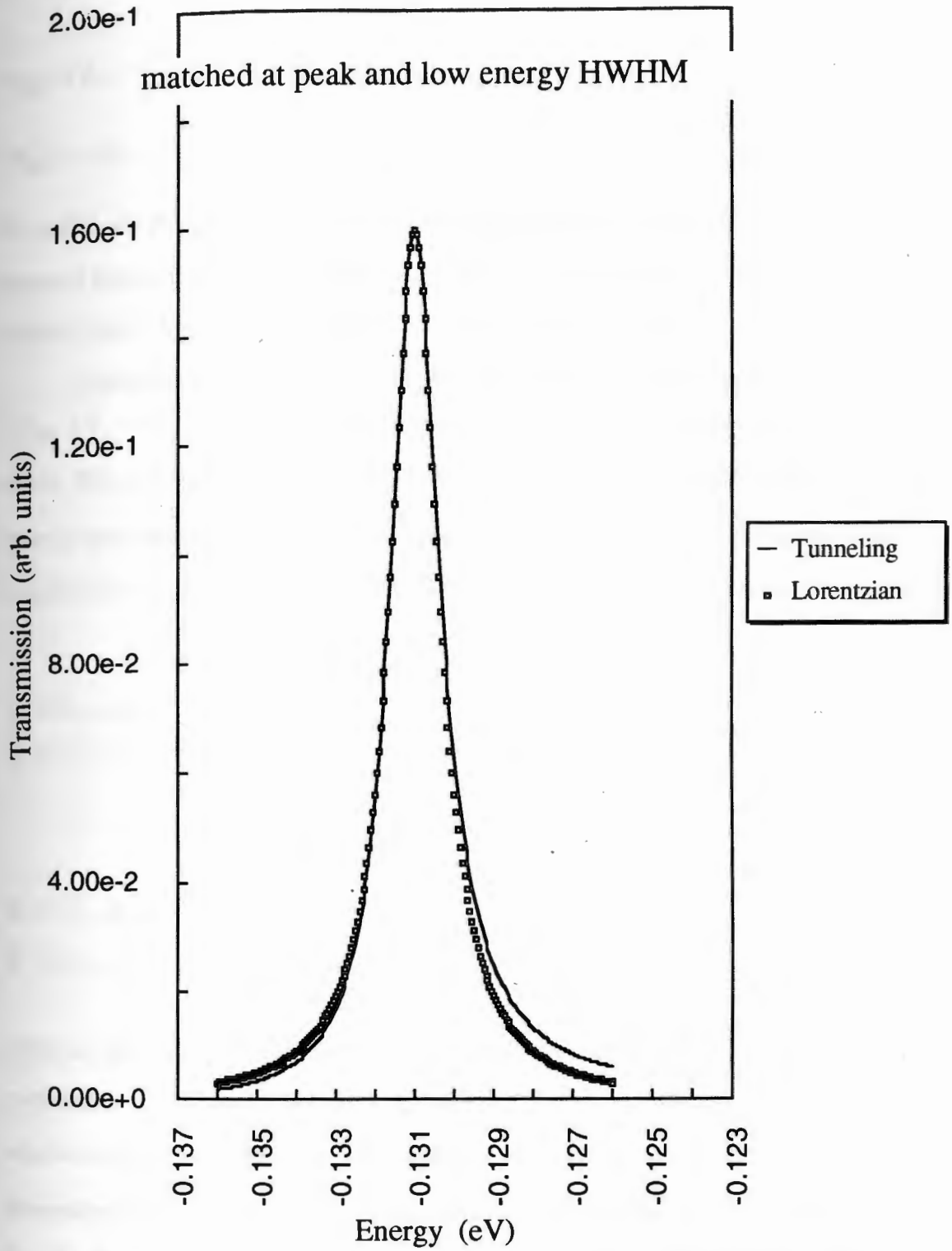

Figure 1.5. Resonance lineshape for electron. Well=7.5 nm, barrier=10 nm, well composition y=.82, barrier y=.23, field=120 kV/cm.

$$H_{KEe} = E_{c0} - \frac{\hbar^2}{2m_c^*}\nabla_e{}^2$$
$$H_{KEh} = -E_{v0} - \frac{\hbar^2}{2m_v^*}\nabla_h{}^2 \qquad (1.17)$$

V_e and V_h are the confining potentials of the wells defined by the bandgap difference between barrier and well and the splitting of that difference between conduction and valence band. The field applied perpendicular to the MQW layer is $F_\perp$.

Combining (1.15) and (1.16), and including the Coulomb interaction, $V_{e\text{-}h}$:

$$\left(H_{KEe} + V_e - eF_\perp z_e + H_{KEh} + V_h + eF_\perp z_h + V_{e-h}(\mathbf{r_e},\mathbf{r_h})\right)\Psi(\mathbf{r_e},\mathbf{r_h}) = E\Psi(\mathbf{r_e},\mathbf{r_h}) \qquad (1.18)$$

where $\Psi(r_e, r_h)$ is the two particle envelope wavefunction for the exciton. The coulomb term couples the electron and hole coordinates and the problem is no longer separable. It is useful to transform to center of mass coordinates in the plane of the layer.

$$\begin{aligned} \mathbf{r_e} &= (x_e, y_e, z_e) \\ \mathbf{r_h} &= (x_h, y_h, z_h) \end{aligned} \quad \rightarrow \quad \begin{aligned} &\mathbf{R} \\ &\mathbf{r} \\ &z_e \\ &z_h \end{aligned} \qquad (1.19a)$$

$$\begin{aligned} \mathbf{k}_e &= (k_{x,e}, k_{y,e}, k_{z,e}) \\ \mathbf{k}_h &= (k_{x,h}, k_{y,h}, k_{z,h}) \end{aligned} \quad \rightarrow \quad \begin{aligned} &\mathbf{K}_\parallel \\ &\mathbf{k}_\parallel \\ &\mathbf{k}_{z,e} \\ &\mathbf{k}_{z,h} \end{aligned} \qquad (1.19b)$$

where $\mathbf{r}_e$ and $\mathbf{r}_h$ are the three dimensional position vectors for the electron and hole with coordinates $x_{e,h}, y_{e,h}, z_{e,h}$ and $\mathbf{R}$ and $\mathbf{r}$ are the two dimensional center of mass and relative coordinates in the plane of the layer, respectively. $\mathbf{k}_e$ and $\mathbf{k}_h$ are the three dimensional wavevectors for the electron and hole, respecitviely, with components $\mathbf{k}_{x,e}, \mathbf{k}_{y,e}, \mathbf{k}_{z,e}$ and $\mathbf{k}_{x,h}, \mathbf{k}_{y,h}, \mathbf{k}_{z,h}$. $\mathbf{K}_\parallel$ and $\mathbf{k}_\parallel$ are the two dimensional in-plane center of mass and relative wavevectors respectively. If ρ_e and ρ_h are the in-plane radial position

vectors of the electron and hole respectively, and $\mathbf{k}_{e\parallel}$ and $\mathbf{k}_{h\parallel}$ are the in-plane radial wavevectors, the transformation is:

$$\mathbf{R} = \frac{m^*_{c,\parallel}\rho_e + m^*_{v,\parallel}\rho_h}{m^*_{c,\parallel} + m^*_{v,\parallel}}$$

$$\mathbf{r} = \rho_e - \rho_h$$

$$\mathbf{k}_\parallel = \frac{m^*_{c,\parallel}\mathbf{k}_{e\parallel} + m^*_{v,\parallel}\mathbf{k}_{h\parallel}}{m^*_{c,\parallel} + m^*_{v,\parallel}}$$

$$\mathbf{K}_\parallel = \mathbf{k}_{e\parallel} - \mathbf{k}_{h\parallel} \tag{1.20}$$

It should be noted that this represents a change in notation. The relative position vector $\mathbf{r}$ in the plane of the layer should not be confused with the previous general three dimensional one particle position vector $\mathbf{r}$. It can be shown that:

$$-\frac{\hbar^2}{2m^*_c}\nabla_e^{\,2} - \frac{\hbar^2}{2m^*_v}\nabla_h^{\,2} = -\frac{\hbar^2}{2m^*_{c,\parallel}}\nabla_{e,\parallel}^{\,2} - \frac{\hbar^2}{2m^*_{c,\perp}}\frac{\partial^2}{\partial z_e^{\,2}} - \frac{\hbar^2}{2m^*_{v,\parallel}}\nabla_{h,\parallel}^{\,2} - \frac{\hbar^2}{2m^*_{v,\perp}}\frac{\partial^2}{\partial z_h^{\,2}} \tag{1.21}$$

is transformed to:

$$-\frac{\hbar^2}{2M_\parallel}\nabla_R^{\,2} - \frac{\hbar^2}{2\mu_\parallel}\nabla_r^{\,2} - \frac{\hbar^2}{2m^*_{c,\perp}}\frac{\partial^2}{\partial z_e^{\,2}} - \frac{\hbar^2}{2m^*_{v,\perp}}\frac{\partial^2}{\partial z_h^{\,2}} \tag{1.22}$$

where

$$M_\parallel = m^*_{c,\parallel} + m^*_{v,\parallel}$$

$$\frac{1}{\mu_\parallel} = \frac{1}{m^*_{c,\parallel}} + \frac{1}{m^*_{v,\parallel}} \tag{1.23}$$

Thus (1.18) may be written as:

$$\begin{pmatrix} E_g + H_{KE,ze} + V_e - eF_\perp z_e + H_{KE,zh} + V_h + eF_\perp z_h \\ + H_{KE,R} + H_{KE,r} + V_{e-h}(\mathbf{r}_e, \mathbf{r}_h) \end{pmatrix} \Psi(\mathbf{R}, \mathbf{r}, z_e, z_h) = E\Psi(\mathbf{R}, \mathbf{r}, z_e, z_h) \tag{1.24}$$

where:

$$H_{KE,R} = -\frac{\hbar^2}{2M_\parallel}\nabla_R^{\,2}$$

$$H_{KE,r} = -\frac{\hbar^2}{2\mu_\parallel}\nabla_r^{\,2}$$

$$H_{KE,zh} = -\frac{\hbar^2}{2m^*_{v,\perp}}\frac{\partial^2}{\partial z_h^{\,2}}$$

$$H_{KE,ze} = -\frac{\hbar^2}{2m^*_{c,\perp}}\frac{\partial^2}{\partial z_e^{\,2}} \tag{1.25}$$

$$E_g = E_{c0} - E_{v0}$$

The coulomb interaction term is:

$$V_{e-h} = \frac{-e^2}{4\pi\varepsilon}\frac{1}{\left[r^2 + (z_e - z_h)^2\right]^{1/2}} \tag{1.26}$$

Exact solution of (1.24) is not possible. Analytic solutions are only possible for the two extreme cases of the bulk semiconductor exciton or the pure two dimensional exciton. Numerous numerical approaches have been implemented to approximate the MQW solution. Most of these assume some sort of separable trial wave function, separating it into functions perpendicular and parallel to the MQW layer. Most approaches have used some sort of variational technique.

A common simplification[5] is to ignore the coulomb effect in the z direction, assuming it to be insignificant in comparison to the confining potential of the well. The single particle z direction envelope wavefunctions are then used unchanged. The variational minimization is performed on only one variational parameter in the plane of the layer. A separable trial wavefunction of the following form is used:

$$\Psi(\mathbf{R},\mathbf{r},z_e,z_h) \approx \Psi_e(z_e)\Psi_h(z_h)\Phi(\mathbf{r}) \tag{1.27}$$

The motion of the center of mass is ignored in the following. The photon momentum is too small to significantly affect it. The z direction wavefunctions Ψ_e and Ψ_h are given by the solution of the one dimensional single particle equations:

$$\begin{aligned}\left(H_{KE,ze} + V_e(z_e) - eF_\perp z_e\right)\Psi_e &= E_e\Psi_e \\ \left(H_{KE,zh} + V_h(z_h) + eF_\perp z_h\right)\Psi_h &= E_h\Psi_h\end{aligned} \tag{1.28}$$

Assuming this form for the wavefunction in effect assumes that the coulomb interaction in the z direction is insignificant in comparison to the well confinement and does not alter the wavefunctions from those of the single particle case. The coulomb interaction is only

accounted for in the x-y plane. The radial envelope wavefunction is a solution of the two dimensional hydrogenic problem, labeled by index n. In the following only the 1-S like state is considered:

$$\Phi(\mathbf{r}) = \sqrt{\frac{2}{\pi}}\frac{1}{\lambda}e^{-r/\lambda} \tag{1.29}$$

where λ is the variational parameter.

The expectation value of the exciton Hamiltonian is evaluated to find the exciton energy.

$$\begin{aligned}\langle\Psi|H|\Psi\rangle &= E_g + \langle\Psi|H_{KE,ze} + V_e - eF_\perp z_e|\Psi\rangle + \langle\Psi|H_{KE,zh} + V_h + eF_\perp z_h|\Psi\rangle \\ &\quad + \langle\Psi|H_{KE,R}|\Psi\rangle + \langle\Psi|H_{KE,r} + V_{e-h}|\Psi\rangle \\ &\approx E_g + E_e + E_h + E_b\end{aligned} \tag{1.30}$$

The kinetic energy of the total mass has been ignored in the last statement. E_g is the basic energy gap of the well material. E_e and E_h are the electron and hole subband energies in their respective wells. E_b is the binding energy of the exciton.

Binding Energy and λ

The variational method of Miller et al.[5] is used to find the binding energy. The variational parameter λ is varied and the corresponding binding energy is calculated. The actual binding energy is the minimum value so obtained and the associated λ gives the lateral size of the exciton.

The binding energy is a combination of the kinetic energy of the relative electron-hole motion in the layer and the Coulomb potential of the electron-hole motion:

$$E_b = E_{KE,r} + E_{PE,r} \tag{1.31}$$

where:

$$E_{KE,r} = \langle \Phi | H_{KE,r} | \Phi \rangle = \frac{\hbar^2}{2\mu\lambda^2} \tag{1.32}$$

$$E_{PE,r} = \langle \Psi | V_{e-h} | \Psi \rangle$$

The potential energy may be written as:

$$E_{PE,r} = \frac{-e^2}{2\pi^2 \varepsilon \lambda^2} \int_{\theta=0}^{2\pi} \int_{z_e} \int_{z_h} |\Psi_e|^2 |\Psi_h|^2 \int_{r=0}^{\infty} \frac{r \exp\left(-2r/\lambda\right)}{\left[(z_e - z_h)^2 + r^2\right]} dr dz_e dz_h d\theta \tag{1.33}$$

The integral over θ is trivial and the integral over r can be handled separately. Equation 1.33 becomes:

$$E_{PE,r} = \frac{-e^2}{2\pi\,\varepsilon\lambda} \int_{z_e} \int_{z_h} |\Psi_e|^2 |\Psi_h|^2 G(\gamma) dz_e dz_h \tag{1.34}$$

where:

$$G(\gamma) \equiv \frac{2}{\lambda} \int_{r=0}^{\infty} \frac{r \exp(-2r/\lambda)}{\sqrt{\gamma^2 + r^2}} dr \tag{1.35}$$

Miller et al. show that G(γ) can be solved as:

$$G(\gamma) = \frac{2|\gamma|}{\lambda} \left\{ \frac{\pi}{2} \left[H_1\left(\frac{2|\gamma|}{\lambda}\right) - N_1\left(\frac{2|\gamma|}{\lambda}\right) \right] - 1 \right\} \tag{1.36}$$

H_1 is the first order Struve function calculated directly by a power series expansion:

$$H_1(z) = \frac{2}{\pi} \left[\frac{z^2}{1^2 \cdot 3} - \frac{z^4}{1^2 \cdot 3^2 \cdot 5} + \frac{z^6}{1^2 \cdot 3^2 \cdot 5^2 \cdot 7} - \bullet \;\; \bullet \;\; \bullet \right] \tag{1.37}$$

N_1 is the first order Neumann function or Bessel function of the second kind. It is calculated from the Wronskian relation:

$$J_1(z) N_0(z) - J_0(z) N_1(z) = \frac{2}{\pi z} \tag{1.38}$$

The first and zeroth order Bessel function of the first kind and the zeroth order Bessel function of the second kind are found from power series expansions.

The calculation of $E_{PE,r}$ is modified from that of Miller et al.[5] in that the electron and hole one dimensional wavefunctions from the resonant tunneling calculation, Ψ_e and

Ψ_h, are utilized rather than approximate analytic forms used by Miller et al. The double integral over z_e and z_h is evaluated numerically using Simpson's rule.

As field is applied, the electron and hole are pulled to opposite sides of the well and the exciton is less strongly bound. This effect enters the calculation through the use of the resonant tunneling electron and hole wavefunctions. As a result, the exciton lateral size is increased. This effect gives a small correction on the exciton energies. More importantly, the exciton size will be found to be important for determining the inhomogeneous linewidth broadening and the oscillator strength.

CHAPTER 2

QW ABSORPTION SPECTRA

Absorption Coefficient

The absorption coefficient for the QW material is derived using first order time dependent perturbation theory[32,33]. Fermi's golden rule gives the probability per unit time for the electric field perturbation of the photon to induce a transition from an initial state $|i\rangle$ of energy E_i to a final state $|f\rangle$ of energy E_f, where $|i\rangle$ and $|f\rangle$ are eigenfunctions of the original unperturbed Hamiltonian. The total transition rate per unit time per unit volume is obtained by summing over all states $|i\rangle$ and $|f\rangle$ in the unit volume.

$$W(\omega)=\frac{2\pi}{\hbar}\left(\frac{eA_0}{m_0}\right)^2\sum_i\sum_f\left|\langle f|e^{i\beta\cdot\mathbf{r}}\mathbf{e}_v\cdot\mathbf{p}|i\rangle\right|^2\delta\left(E_f-E_i-\hbar\omega\right) \tag{2.1}$$

where A_0 is the amplitude and $\mathbf{e}_v$ is the unit polarization vector of the electromagnetic vector potential given by:

$$\mathbf{A}=A_0\mathbf{e}_v\exp(i\beta\cdot\mathbf{r}-i\omega t) \tag{2.2}$$

and where $\mathbf{p}=-i\hbar\nabla$.

The absorption coefficient is given by:

$$\alpha=\frac{\hbar\omega W(\omega)}{(c/n)U} \tag{2.3}$$

where U is the energy density of the electric field and (c/n)U is the energy flux. The amplitude of the electric field is obtained by equating the energy in the field to $\hbar\omega$, finally obtaining:

$$\alpha=\frac{\pi e^2}{m_o\varepsilon\omega(c/n)}\sum_i\sum_f\frac{1}{\Omega}\left|\langle f|e^{i\beta\cdot\mathbf{r}}\mathbf{e}_v\cdot\mathbf{p}|i\rangle\right|^2\delta\left(E_f-E_i-\hbar\omega\right) \tag{2.4}$$

where ε is the dielectric constant and Ω is the volume.

The MQW absorption spectra exhibit both sharp resonances due to excitons and a broad continuum absorption due to band to band transitions between unbounded valence and conduction band states. The above equation may be used for evaluating both the continuum absorption due to the unbounded electron and hole states and the exciton absorption due to the exciton states. It is necessary to use the correct forms for the initial and final states and determine the matrix elements for the specific case of interest.

QW Continuum Absorption

As shown in Chapter 1, the total wavefunction for either conduction or valence band states may be expressed as:

$$\begin{aligned}\Psi_B^n(z,\mathbf{r}_\parallel) &= e^{i\mathbf{k}_\parallel\cdot\mathbf{r}_\parallel}u_B(0,\mathbf{r})\Psi_B^n(z)\\ &= e^{i\mathbf{k}_\parallel\cdot\mathbf{r}_\parallel}u_{Bz}(0,z)u_{B\parallel}(0,\mathbf{r}_\parallel)\Psi_B^n(z)\end{aligned} \tag{2.5}$$

where $\mathbf{r}_\parallel$ is the in-plane position vector and the periodic Bloch function has been split into separate functions with z and x,y dependence.

The matrix element is separable as:

$$\langle f|e^{i\beta\cdot\mathbf{r}}\mathbf{e}_v\cdot\mathbf{p}|i\rangle = \langle f_z|e^{i\beta\cdot z}\mathbf{e}_v\cdot\mathbf{p}_z|i_z\rangle\langle f_\parallel|e^{i\beta\cdot\mathbf{r}_\parallel}\mathbf{e}_v\cdot\mathbf{p}_\parallel|i_\parallel\rangle \tag{2.6}$$

The in-layer part is handled first. An electron transitions from a valence band state to the conduction band in the process of absorbing a photon.

$$\langle f_\parallel|e^{i\beta\cdot\mathbf{r}_\parallel}\mathbf{e}_v\cdot\mathbf{p}_\parallel|i_\parallel\rangle = \left\langle e^{i\mathbf{k}_\parallel'\cdot\mathbf{r}_\parallel}u_{c,\parallel}\left(\mathbf{k}_\parallel',\mathbf{r}_\parallel\right)\middle|e^{i\beta\cdot\mathbf{r}_\parallel}\mathbf{e}_v\cdot\mathbf{p}_\parallel\middle|e^{i\mathbf{k}_\parallel\cdot\mathbf{r}_\parallel}u_{v,\parallel}(\mathbf{k}_\parallel,\mathbf{r}_\parallel)\right\rangle \tag{2.7}$$

It can be shown that:

$$\langle f_\parallel|e^{i\beta\cdot\mathbf{r}_\parallel}\mathbf{e}_v\cdot\mathbf{p}_\parallel|i_\parallel\rangle = \langle u_{c,\parallel}|\mathbf{e}_v\cdot\mathbf{p}_\parallel|u_{v,\parallel}\rangle\delta_{\mathbf{k}_\parallel\mathbf{k}_\parallel'} \tag{2.8}$$

where the photon momentum has been neglected as insignificant, $\beta \approx 0$, so that the momentum conservation requirement becomes: $\mathbf{k}_\parallel \approx \mathbf{k}_\parallel'$.

Next the z dependent part is solved.

$$\langle f_z|e^{i\beta\cdot z}\mathbf{e}_v\cdot\mathbf{p}_z|i_z\rangle = \left\langle\Psi_c^n(z_e)u_{c,z}(0,z)\middle|e^{i\beta\cdot z}\mathbf{e}_v\cdot\mathbf{p}_z\middle|\Psi_v^m(z_h)u_{v,z}(0,z)\right\rangle \tag{2.9}$$

The same procedure is followed as with the in-layer part and it can be shown that:

$$\langle f_z | e^{i\beta \cdot z} \mathbf{e}_v \cdot \mathbf{p}_z | i_z \rangle = \langle u_{c,z} | \mathbf{e}_v \cdot \mathbf{p}_z | u_{v,z} \rangle \langle \Psi_c^n | \Psi_v^m \rangle \tag{2.10}$$

Finally, equations 2.4, 2.6 , 2.8, and 2.10 are combined. The sum over initial and final states becomes a sum over the various conduction and valence subbands, over spin, and over all $\mathbf{k}_{\|}$ in the Brillouin zone.

$$\alpha_{cont} = \frac{\pi e^2}{m_o \varepsilon \omega (c/n)} \sum_c \sum_v \sum_n \sum_m \left| \langle \Psi_c^n | \Psi_v^m \rangle \right|^2 \left| P_{cv} \right|^2 (2) \sum_{\mathbf{k}_{\|}} \frac{1}{\Omega} \delta(E_f - E_i - \hbar\omega) \tag{2.11}$$

Here the two in parenthesis is due to spin. The optical matrix element P_{CV} comes from combining the z and in-plane matrix elements as:

$$P_{cv} \equiv \langle u_{c,z} | \mathbf{e}_v \cdot \mathbf{p}_z | u_{v,z} \rangle \langle u_{c,\|} | \mathbf{e}_v \cdot \mathbf{p}_{\|} | u_{v,\|} \rangle \tag{2.12}$$

Next, the summation over $\mathbf{k}_{\|}$ is converted into an integral and cylindrical coordinates are used. Given that the main interest is in the lowest energy transitions near zone center, the bands may be assumed to have approximately parabolic dispersion relations:

$$E_B(k) = E_{B0} \pm \frac{\hbar^2 k^2}{2m_B^*} \tag{2.13}$$

Finally:

$$\alpha_{cont} = \frac{\pi e^2}{m_o \varepsilon \omega (c/n)} \sum_c \sum_v \sum_n \sum_m \left| \langle \Psi_c^n | \Psi_v^m \rangle \right|^2 \left| P_{cv} \right|^2 \left(\frac{\mu_{c,v,n,m}}{\pi \hbar^2} \right) \int dE \delta(E_f - E_i - \hbar\omega) \tag{2.14}$$

where the reduced mass is given by:

$$\frac{1}{\mu} = \frac{1}{m_c^*} + \frac{1}{m_v^*} \tag{2.15}$$

To study the absorption near the band edge only a limited number of valence and conduction subbands will be considered in practice.

QW Exciton Absorption

The derivation of exciton absorption is similar in approach to the continuum absorption. The initial state consists of a hole in the conduction band and an electron in the valence band. The final state is an exciton state with an electron in the conduction band bound to a hole in the valence band. The initial state is a combination of two single particle states. The expression for an electron in the conduction band is:

$$\Psi_c = \Psi_e(z_e)e^{i\mathbf{k}_{\parallel e}\cdot\mathbf{r}_{\parallel e}}u_{\parallel,c}(0,\mathbf{r}_{\parallel e})u_{z,c}(0,z_e) \tag{2.16}$$

where the periodic function u has been separated into parts perpendicular and parallel to the QW layer. The actual initial state has a hole in the conduction band:

$$\Psi_c = \Psi_e^*(z_e)e^{-i\mathbf{k}_{\parallel e}\cdot\mathbf{r}_{\parallel e}}u_{\parallel,c}(0,\mathbf{r}_{\parallel e})u_{z,c}(0,z_e) \tag{2.17}$$

A hole in the valence band may be expressed as:

$$\Psi_v = \Psi_h(z_h)e^{-i\mathbf{k}_{\parallel h}\cdot\mathbf{r}_{\parallel h}}u_{\parallel,v}(0,\mathbf{r}_{\parallel h})u_{z,v}(0,z_h) \tag{2.18}$$

Actually start with an electron in valence band:

$$\Psi_v = \Psi_h^*(z_h)e^{i\mathbf{k}_{\parallel h}\cdot\mathbf{r}_{\parallel h}}u_{\parallel,v}(0,\mathbf{r}_{\parallel h})u_{z,v}(0,z_h) \tag{2.19}$$

Combining (2.17) and (2.19) to get the initial state:

$$\Psi_i = \Psi_c\Psi_v = e^{-i(\mathbf{k}_{\parallel e}\cdot\mathbf{r}_{\parallel e}-\mathbf{k}_{\parallel h}\cdot\mathbf{r}_{\parallel h})}\Psi_e^*(z_e)\Psi_h^*(z_h)u_{\parallel,c}u_{\parallel,v}u_{z,c}u_{z,v}, \tag{2.20}$$

Converting to center of mass coordinates in the x,y plane:

$$\Psi_i = e^{-i\mathbf{K}_{\parallel}\cdot\mathbf{R}}e^{-i\mathbf{k}_{\parallel}\cdot\mathbf{r}}\Psi_e^*(z_e)\Psi_h^*(z_h)u_{\parallel,c}u_{\parallel,v}u_{z,c}u_{z,v} \tag{2.21}$$

As before, the center of mass part will be ignored in the following.

The final exciton state is expressed as:

$$\Psi_f = \Psi_e(z_e)\Psi_h(z_h)\Phi_n(\mathbf{r})u_{\parallel,c}u_{\parallel,v}u_{z,c}u_{z,v} \tag{2.22}$$

The matrix element is again separable as:

$$\langle f|e^{i\beta\cdot\mathbf{r}}\mathbf{e}_v\cdot\mathbf{p}|i\rangle = \langle f_z|\mathbf{e}_v\cdot\mathbf{p}_z|i_z\rangle\langle f_{\parallel}|\mathbf{e}_v\cdot\mathbf{p}_{\parallel}|i_{\parallel}\rangle \tag{2.23}$$

The photon momentum term was dropped because, as was seen in the continuum case, it does not affect the results of interest.

Considering the z problem first:

$$\langle f_z|\mathbf{e}_v\cdot\mathbf{p}_z|i_z\rangle = \langle\Psi_e(z_e')\Psi_h(z_h')u_{z,c},u_{z,v}|\mathbf{e}_v\cdot\mathbf{p}_z|\Psi_e^*(z_e)\Psi_h^*(z_h)u_{z,c}u_{z,v}\rangle \tag{2.24}$$

However, the transition from a hole in the conduction band and electron in the valence band to an electron in the conduction band and a hole in the valence band is the same thing as an electron transitioning from valence to conduction band.

$$\langle f_z|\mathbf{e}_v\cdot\mathbf{p}_z|i_z\rangle = \langle\Psi_e(z_e)u_{z,c}|\mathbf{e}_v\cdot\mathbf{p}_z|\Psi_h^*(z_h)u_{z,v}\rangle \tag{2.25}$$

Following the same derivation as used earlier for the continuum, it can be shown that:

$$\langle f_z|\mathbf{e}_v\cdot\mathbf{p}_z|i_z\rangle = \langle\Psi_e|\Psi_h\rangle\langle u_{z,c}|\mathbf{e}_v\cdot\mathbf{p}_z|u_{z,v}\rangle \tag{2.26}$$

Next, considering the part in the layer:

$$\langle f_{\parallel}|\mathbf{e}_v \cdot \mathbf{p}_{\parallel}|i_{\parallel}\rangle = \langle \Phi_n(\mathbf{r}) u_{\parallel,c} u_{\parallel,v} |\mathbf{e}_v \cdot \mathbf{p}_{\parallel}| e^{-i\mathbf{k}_t \cdot \mathbf{r}} u_{\parallel,c} u_{\parallel,v} \rangle \tag{2.27}$$

The two dimensional hydrogen-like wave function in the x-y plane is next expanded in terms of the in-plane $k_{\parallel}$ plane wave states:

$$\Phi_n(\mathbf{r}) = \sum_{k_{\parallel}} \phi_{n,k\parallel} e^{i\mathbf{k}_t \cdot \mathbf{r}} \tag{2.28}$$

Thus:

$$\begin{aligned}\langle f_{\parallel}|\mathbf{e}_v \cdot \mathbf{p}_{\parallel}|i_{\parallel}\rangle &= \sum_{k_t'} \phi_{n,k_t'} \langle u_{\parallel,c} u_{\parallel,v} | e^{i(\mathbf{k}_t' - \mathbf{k}_t)\cdot \mathbf{r}} (\mathbf{e}_v \cdot \mathbf{p}_{\parallel} - i\mathbf{k}_{\parallel}) | u_{\parallel,c} u_{\parallel,v} \rangle \\ &= \sum_{k_t'} \phi_{n,k_t'} \delta_{\mathbf{k}_t' \mathbf{k}_t} \langle u_{\parallel,c} u_{\parallel,v} | \mathbf{e}_v \cdot \mathbf{p}_{\parallel} | u_{\parallel,c} u_{\parallel,v} \rangle \\ &= \sum_{k_{\parallel}} \phi_{n,k_t} \langle u_{\parallel,c} | \mathbf{e}_v \cdot \mathbf{p}_{\parallel} | u_{\parallel,v} \rangle\end{aligned} \tag{2.29}$$

It is noted that:

$$\Phi_n(\mathbf{r}=0) = \sum_{k_{\parallel}} \phi_{n,k\parallel} \tag{2.30}$$

Thus:

$$\langle f_{\parallel}|\mathbf{e}_v \cdot \mathbf{p}_{\parallel}|i_{\parallel}\rangle = \Phi_n(0) \langle u_{\parallel,c} |\mathbf{e}_v \cdot \mathbf{p}_{\parallel}| u_{\parallel,v} \rangle \tag{2.31}$$

Finally, combining (2.26) and (2.31):

$$\begin{aligned}\langle f_{\parallel}|\mathbf{e}_v \cdot \mathbf{p}_{\parallel}|i_{\parallel}\rangle &= \Phi_n(0) \langle \Psi_e | \Psi_h \rangle \langle u_{\parallel,c} |\mathbf{e}_v \cdot \mathbf{p}_{\parallel}| u_{\parallel,v} \rangle \langle u_{z,c} |\mathbf{e}_v \cdot \mathbf{p}_z| u_{z,v} \rangle \\ &= \Phi_n(0) \langle \Psi_e | \Psi_h \rangle \langle u_c |\mathbf{e}_v \cdot \mathbf{p}_{\parallel}| u_v \rangle \\ &= \Phi_n(0) \langle \Psi_e | \Psi_h \rangle P_{cv}\end{aligned} \tag{2.32}$$

where in the last statement attention is restricted to near zone center where the coupling is assumed independent of k.

Finally, in determining the absorption, the sum over initial and final states becomes a sum over the various conduction and valence subbands, over spin, and over index n.

$$\alpha_{excitons} = \frac{\pi e^2}{m_o \varepsilon \omega (c/n)} \sum_c \sum_v |\langle \Psi_c | \Psi_v \rangle|^2 |P_{cv}|^2 (2) \sum_n |\Phi_n(0)|^2 \delta(E_{n0} - \hbar\omega) \tag{2.33}$$

CHAPTER 3

LINEWIDTH

The calculation of proper linewidth is of major importance for optimizing modulator design because modulator performance is critically affected by the steepness of the absorption edge. Design choices which adversely affect linewidth will degrade performance and this must be modeled accurately to determine which tradeoffs are profitable. Previous efforts to optimize modulator device design have relied upon simplified empirical expressions for the linewidth based on measured values.[16,23] More extensive theoretical treatments of linewidth factors are available, and this study will use or modify such treatments to derive expressions for the various components of linewidth and their dependence upon quantum well design and applied field. Several factors influence the linewidth and many of them can be of the same order of magnitude. Early theoretical treatments neglected some of the key factors and there has been considerable confusion in the literature concerning which factors can be expected to contribute significantly.[34]

There has also been a variety of methods by which the various mechanism's linewidths are combined and considerable differences in the lineshapes used for various mechanisms. Several authors have pointed out that mechanisms with different lineshapes should be combined by convolution of the lineshapes.[16,23] This study will follow this approach. The total linewidth (full width half maximum, FWHM) for a combination of multiple Gaussian lineshapes can be calculated from the individual linewidths (FWHM) as:

$$FWHM_{tot} = \sqrt{\sum_{i=1}^{n} FWHM_i^2} \tag{3.1}$$

This study considered the following linewidth factors: (1) Lorentzian homogeneous broadening due to tunneling of electrons and holes, (2) Gaussian thermal

broadening, (3) Gaussian inhomogeneous broadening due to random alloy compositional disorder in both wells and barriers, and (4) inhomogeneous broadening due to random variations in well width. The first two are intrinsic, while the second two will be sample dependent.

Tunneling Broadening

It has already been shown in Chapter 1 that the resonant tunneling method well describes the linewidth broadening due to tunneling. Figure 1.5 indicates that this broadening is well described by a Lorentzian lineshape.

Thermal Broadening

Measurements of exciton linewidth versus temperature were reported by Chemla et al.[35] for GaAs/AlGaAs multi-quantum wells and by Sugawara et al.[33,36] for InGaAsP/InP. Their results were well described as broadening due to exciton ionization due to interaction with longitudinal optical (LO) phonons. The linewidth is proportional to the density of LO phonons, described by Bose-Einstein statistics as:[35]

$$\sigma_T = \frac{\sigma_{ph}}{\left[\exp(\hbar\omega_{LO}/k_B T) - 1\right]} \tag{3.2}$$

where $\hbar\omega_{LO}$ = 32 meV is the LO phonon energy, k_B is Boltzmann's constant, T is the temperature, and σ_{ph} is the coupling constant between phonon and exciton. It is assumed that this broadening does not change with applied field. Sugawara et al.[36] found room temperature linewidth (FWHM) of approximately 9 meV in InGaAsP/InP multi-quantum wells with various compositions. Sugawara et al.[36] and Chemla et al.[35] both found that a Gaussian lineshape best fits the measured spectra.

Composition Broadening

In quaternary and ternary semiconductor alloys, local variations in alloy composition are a source of inhomogeneous broadening of the exciton linewidth. These

variations may be totally random or include clustering effects and long range fluctuations. The first theoretical derivation of this broadening in bulk semiconductors was done by Goede.[37] Apparently unaware of this work, both Schubert et al.[38] and Singh and Bajaj[39] independently derived matching results which each differed from that of Goede. Singh and Bajaj[40] later presented a quantum mechanical correction to this theory which brought it into closer agreement with Goede's work. However, numerous researchers have followed Schubert et al. and continue to neglect this correction factor. Hong and Singh[34] later modified Singh and Bajaj's theory for use with multi-quantum wells. The general approach in this work was to extend and correct the approach of Hong and Singh and implement the calculations using the RTM. Because of the great computational complexity of implementing such a calculation, this method was not suitable for use as part of the larger modulator optimization model. An approximation, loosely based on work by Sugawara et al.,[33] is presented which greatly simplified calculations and yielded adequate accuracy. Both methods are presented in what follows.

An alloy composition change in some region of the well or barrier can change the energy of the exciton. Both the bandgap and effective masses for the material are affected by a composition change. The bandgap in turn alters the potential well and hence the electron and hole subband levels as well as the basic energy gap to which these are referenced. The exciton energy shift from a fluctuation in composition ΔC over a volume V may be written:

$$\begin{aligned}\Delta E &= (C - C_0)\frac{\delta E_{exc}}{\delta C}\bigg|_{C_0} \int_V |\Psi(\mathbf{r})|^2 d^3r \\ &= \Delta C \frac{\delta E_{exc}}{\delta C}\bigg|_{C_0} \langle \Psi | \Psi \rangle_V\end{aligned} \tag{3.3}$$

where C is the new concentration and C_0 is the average concentration. Actually the wavefunction is a two particle wavefunction and it is appropriate to consider separately

how the composition affects the electron and hole. Recalling the previous form of the wavefunction from equation 1.27 the following is obtained:

$$\Delta E = \Delta C\left[\frac{\delta E_{elec}}{\delta C}\left\langle\phi(r)\psi_e(z_e)|\psi_e(z_e)\phi(r)\right\rangle_V + \frac{\delta E_{hole}}{\delta C}\left\langle\phi(r)\psi_h(z_h)|\psi_h(z_h)\phi(r)\right\rangle_V\right] \quad (3.4)$$

For a purely random alloy or one with random clustering, the probability of a composition fluctuation ΔC occurring over a volume V is governed by binomial statistics. This probability has been derived by both Schubert et al.[38] and Singh and Bajaj[39]. Schubert notes that the binomial distribution can be approximated by a Gaussian distribution, the necessary condition being met throughout the composition range of interest. When this is done the full width at half maximum (FWHM) of such a distribution is given by Singh and Bajaj as[40]:

$$FWHM(\Delta C, V) = 2\sqrt{\frac{1.4C_0(1-C_0)V_c}{V}} \quad (3.5)$$

where V_c is the cluster volume or the minimum volume over which a concentration fluctuation can occur. For a purely random alloy without clustering, the cluster volume is the volume per cation or anion. Combining the above:

$$FWHM(\Delta E, V) = 2\sqrt{\frac{1.4C_0(1-C_0)V_c}{V}}\left[\frac{\delta E_{elec}}{\delta C}\left\langle\phi\psi_e|\psi_e\phi\right\rangle_V + \frac{\delta E_{hole}}{\delta C}\left\langle\phi\psi_h|\psi_h\phi\right\rangle_V\right] \quad (3.6)$$

The exciton linewidth is found by considering all possible volumes V to find those configurations which maximize the shift ΔE.

$$FWHM = \max_V\left\{FWHM(\Delta E, V)\right\}$$

$$= 2\sqrt{1.4C_0(1-C_0)V_c}\max_V\left\{\frac{\delta E_{elec}}{\delta C}\frac{\left\langle\phi\psi_e|\psi_e\phi\right\rangle_V}{\sqrt{V}} + \frac{\delta E_{hole}}{\delta C}\frac{\left\langle\phi\psi_h|\psi_h\phi\right\rangle_V}{\sqrt{V}}\right\} \quad (3.7)$$

Next, cylindrical volumes are considered, with variable height β (not related to photon wavevector β) and radius r with variable parameter γ such that :

$$r = \gamma\lambda$$

$$V = \pi\gamma^2\lambda^2\beta \quad (3.8)$$

Using such a volume and the separability of the wavefunctions, the linewidth is given by:

$$FWHM = 2\sqrt{1.4C_0(1-C_0)V_c}\max_V\left\{\frac{\delta E_{elec}}{\delta C}\frac{\langle\psi_e|\psi_e\rangle_V}{\sqrt{\pi\lambda^2\beta}}\frac{\langle\phi|\phi\rangle_V}{\gamma}+\frac{\delta E_{hole}}{\delta C}\frac{\langle\psi_h|\psi_h\rangle_V}{\sqrt{\pi\lambda^2\beta}}\frac{\langle\phi|\phi\rangle_V}{\gamma}\right\}$$

$$=2\sqrt{\frac{1.4C_0(1-C_0)V_c}{\pi\lambda^2}}\max_\beta\left\{\frac{\delta E_{elec}}{\delta C}\frac{\langle\psi_e|\psi_e\rangle_V}{\sqrt{\beta}}+\frac{\delta E_{hole}}{\delta C}\frac{\langle\psi_h|\psi_h\rangle_V}{\sqrt{\beta}}\right\}\max_\gamma\left\{\frac{\langle\phi|\phi\rangle_V}{\gamma}\right\} \tag{3.9}$$

First consider the optimization over the plane of the layers. The wavefunction is given by:

$$\phi(r)=\left(\frac{2}{\pi}\right)^{1/2}\frac{1}{\lambda}\exp\left(-r/\lambda\right) \tag{3.10}$$

Thus:

$$\max_\gamma\left\{\frac{\langle\phi|\phi\rangle_V}{\gamma}\right\}=\max_\gamma\left\{\frac{1}{\gamma}\int_0^{2\pi\gamma\lambda}\int_0\frac{2}{\pi\lambda^2}\left|\exp(-r/\lambda)\right|^2 rdrd\theta\right\}$$

$$=\max_\gamma\left\{\frac{1}{\gamma}\left[1-\exp(-2\gamma)(2\gamma+1)\right]\right\} \tag{3.11}$$

This is maximized for γ=0.9 at which the value is 0.59685. This is the QW version of the quantum mechanical correction factor first introduced for bulk semiconductors by Singh and Bajaj.[40] This has previously been wrongly omitted by other authors.[34] Incorporating this factor into equation 3.9:

$$FWHM = 2(Clus)\sqrt{\frac{1.4C_0(1-C_0)V_{wig}}{\pi\lambda^2}}\max_\beta\left\{\frac{\delta E_{elec}}{\delta C}\frac{\langle\psi_e|\psi_e\rangle_\beta}{\sqrt{\beta}}+\frac{\delta E_{hole}}{\delta C}\frac{\langle\psi_h|\psi_h\rangle_\beta}{\sqrt{\beta}}\right\}(0.59685) \tag{3.12}$$

V_{wig} is the Wigner-Seitz cell volume, which is the smallest volume over which a composition fluctuation can occur. "Clus" is the cluster factor which describes additional clustering of the composition variations.

This equation can be applied to both well and barrier composition broadening by altering the composition over appropriate regions. The above equation is for fluctuations of a single species of the alloy. In a quaternary alloy like $In_xGa_{1-x}As_yP_{1-y}$ both x and y can vary, presumably independently. Given Gaussian distributions their linewidths can be combined as:

$$FWHM_{tot} = \sqrt{FWHM_x^2 + FWHM_y^2} \tag{3.13}$$

Two methods were used to evaluate equation 3.12. The first utilizes the RTM to analyze the energy shifts when composition is changed in regions of various height, β. Because the method is computationally intensive and must be done numerous times (left barrier, right barrier, well; x and y; three exciton types; multiple fields) it is too involved for use in a modulator design optimization model. The second model is a first order approximation. Both will be described and the results compared.

Well Composition Broadening

RTM Method

The RTM is capable of handling an arbitrarily complex stack of semiconductor layers. It is thus possible to alter the composition slightly in a small region of either the well or barrier and recalculate the electron and hole energy levels. Comparison with the levels from the normal configuration gives the shift associated with the composition change. It is noted that this is not a first order approximation because the RTM completely recalculates the problem, determining both new subband levels and new wavefunctions. It takes into account changes in both bandgap and effective mass associated with the composition change. The RTM automatically takes into account the wavefunction weighting of the perturbation:

$$\left.\frac{\delta E_{elec}}{\delta C}\right|_{\beta,RTM} = \frac{\delta E_{elec}}{\delta C}\langle\psi_e|\psi_e\rangle_\beta$$
$$\left.\frac{\delta E_{hole}}{\delta C}\right|_{\beta,RTM} = \frac{\delta E_{hole}}{\delta C}\langle\psi_h|\psi_h\rangle_\beta \quad (3.14)$$

where $\left.\frac{\delta E_{elec}}{\delta C}\right|_{\beta,RTM}$ and $\left.\frac{\delta E_{hole}}{\delta C}\right|_{\beta,RTM}$ are the change in the electron and hole subband energy levels, calculated with the RTM by varying the composition over a region of height β.

Equation 3.12 involves an optimization over volumes with various β. The simplest method to implement this is to perform RTM calculations for multiple regions to find that which maximizes the total of the electron and hole subband level shifts, and hence the linewidth. This does not prove generally feasible, given that separate RTM calculations must be done for multiple β's, for x and y composition shifts, for heavy, light, and second heavy hole excitons, and for multiple fields. Hong and Singh[34] only used a single region comprising the entire well, arguing that the exciton was almost completely contained in the well. However, this is not as true for the InGaAsP system with its lesser electron confinement, and it is not true if applied fields are considered. In this work, optimization over regions of various β in the well is considered. A first simplification is to assume that the effect of a composition shift in a particular volume is proportional to the probability that the particle is found in that volume. Thus a single RTM calculation can be done for the case in which the entire well composition is altered, and the effect of regions of different β can be calculated from knowledge of the wavefunction.

It is necessary to judiciously choose appropriate regions. The chosen regions are centered in the well and a series of different thicknesses is used. This is depicted in figure 3.1 for the conduction band. The case of the valence band is similar. Different size steps in height, β, were tried to ensure that the derivative converged. It was found that 1.0 nm steps were adequate. An RTM calculation of the altered electron and hole subband

levels is performed for the case in which the entire well composition is changed. This is shown as the top diagram of figure 3.1. This is repeated for both a composition change in x and for a y change. The amount of composition shift for the RTM calculation was varied to ensure that the derivative converged. The final program altered the composition by 2 percent in x or y. The subband level shifts for the various regions are calculated as:

$$\left.\frac{\delta E_{elec}}{\delta C}\right|_{\beta,RTM} = \left.\frac{\delta E_{elec}}{\delta C}\right|_{entire\ well\ altered,RTM} \frac{\langle \Psi_e | \Psi_e \rangle_\beta}{\langle \Psi_e | \Psi_e \rangle_{entire\ well}}$$
$$\left.\frac{\delta E_{hole}}{\delta C}\right|_{\beta,RTM} = \left.\frac{\delta E_{hole}}{\delta C}\right|_{entire\ well\ altered,RTM} \frac{\langle \Psi_h | \Psi_h \rangle_\beta}{\langle \Psi_h | \Psi_h \rangle_{entire\ well}} \qquad (3.15)$$

Because the fluctuations involved are small, the binding energy and exciton size λ are assumed to be unaffected by the composition perturbations and are not recalculated.

First Order Approximation

The linewidths may be approximated by assuming that the change in energy levels is directly related to the energy gap change alone:[33]

$$\frac{\delta E_{elec}}{\delta C} \approx 0.4 \frac{\delta E_g}{\delta C}$$
$$\frac{\delta E_{hole}}{\delta C} \approx 0.6 \frac{\delta E_g}{\delta C} \qquad (3.16)$$

Here 0.4 and 0.6 are the assumed factors for splitting the bandgap change between conduction and valence bands. With this approximation the energy shifts can be calculated directly with only a single RTM calculation. The regions chosen are similar to those used in the previous method.

Comparison

The two methods were compared for the case of a MQW with 7.5 nanometer InGaAsP well and 10 nanometer InGaAsP barrier. The well y value was 0.846 and the x

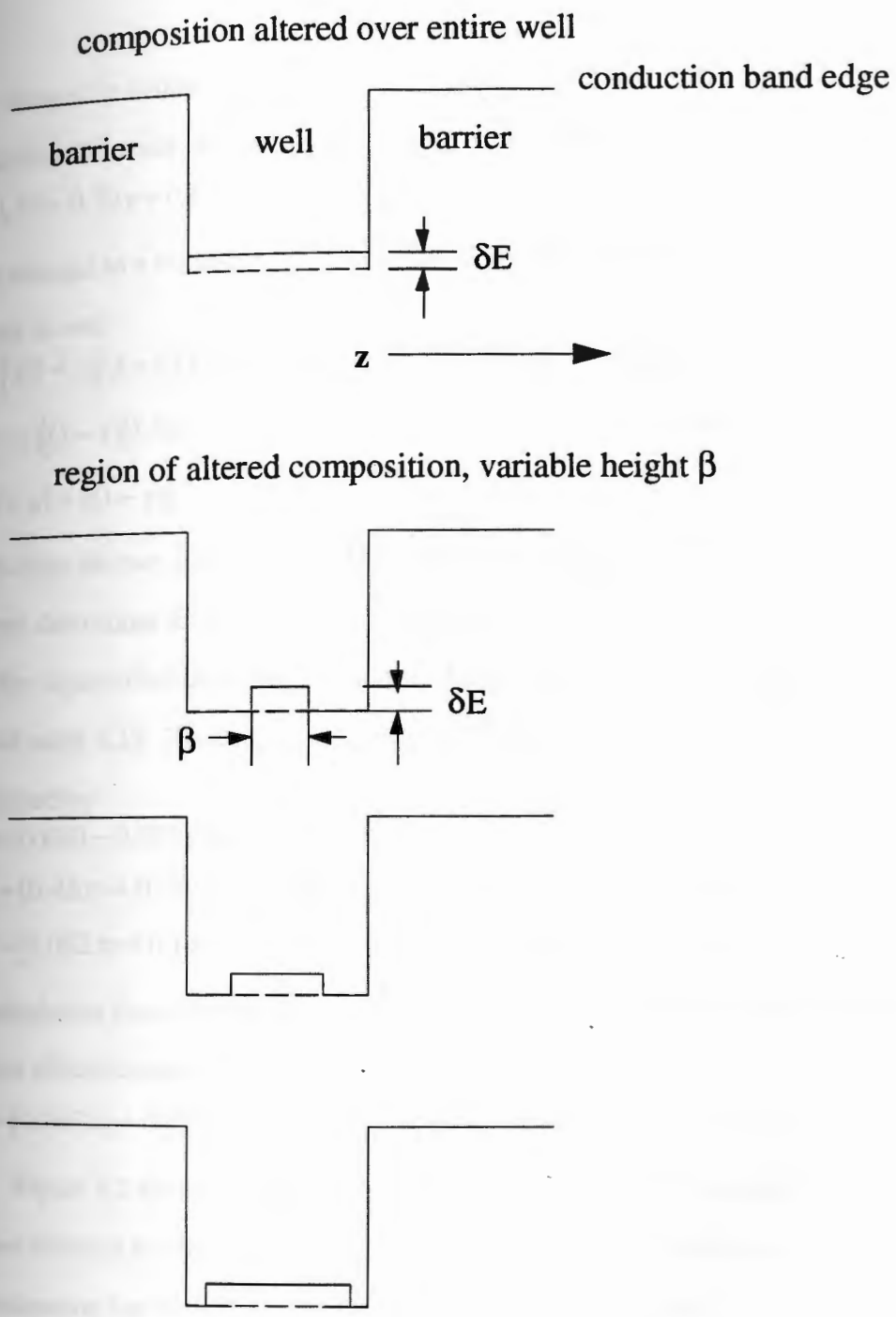

Figure 3.1. Depiction of the regions of altered composition used in the calculation of well composition broadening.

value chosen for lattice matching to an InP substrate. The barrier y was .405.

Throughout this study the energy gap is given by the empirical relation:

$$E_g = 1.35 - 0.72y + 0.12y^2 \tag{3.17}$$

When changes in x composition are considered, the less-accurate, two-way interpolation formula is used:

$$\begin{aligned} E_g = &\left\{x(1-x)\left[(1-y)\left(1.35+0.643x+0.786x^2\right)+y\left(0.36+0.505x+0.555x^2\right)\right]\right. \\ &\left.+y(1-y)\left[(1-x)\left(1.35-1.083y+0.091y^2\right)+x\left(2.74-1.473y+0.146y^2\right)\right]\right\} \\ &\times\left[x(1-x)+y(1-y)\right]^{-1} \end{aligned} \tag{3.18}$$

Levels from the two equations cannot be compared without errors. Thus, when the RTM program determines level shifts due to x fluctuations it is necessary to compare levels from the unperturbed case derived using 3.18 and the levels of the perturbed case, also derived using 3.18. The effective masses for electron, heavy hole, and light hole are determined by:

$$\begin{aligned} m^*_e &= (0.080 - 0.039y)m_0 \\ m^*_{hh} &= \left[0.45xy + 0.79x(1-y) + 0.40(1-x)y + 0.45(1-x)(1-y)\right]m_0 \\ m^*_{lh} &= \left[0.082xy + 0.14x(1-y) + 0.026(1-x)y + 0.12(1-x)(1-y)\right]m_0 \end{aligned} \tag{3.19}$$

For calculating linewidths for x , the alternate interpolation formula is used for the electron effective mass:

$$m^*_e = \left[0.067xy + 0.082x(1-y) + 0.023(1-x)y + 0.077(1-x)(1-y)\right]m_0 \tag{3.20}$$

Figure 3.2 shows a comparison of the well composition broadening calculated by the two methods for this case. The variation between the RTM method and the first order approximation for the heavy hole runs from 2% to 7% with fields from 0 to 120 kV/cm. Agreement is good for the light and second heavy hole excitons as well. Given the limited accuracy in determining exciton linewidths and the lesser importance in comparison with other broadening factors, this level of accuracy is sufficient. The first order approximation was therefore used in the modulator design optimization.

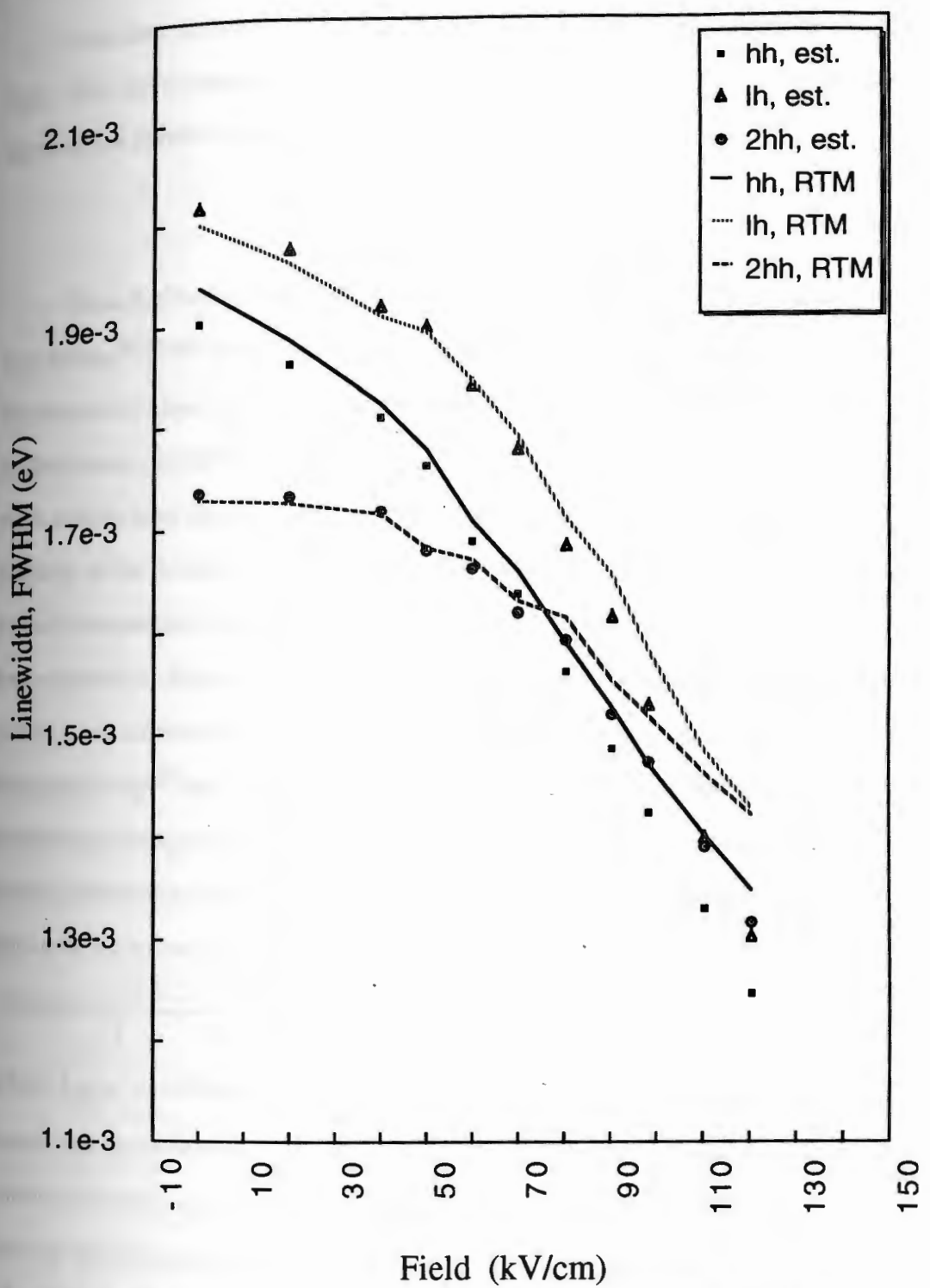

Figure 3.2. Well composition linewidth for the RTM method and the first order approximation method.

Note that this linewidth broadening mechanism actually improves with applied field. This occurs because high applied fields drive the particles toward the barriers, reducing the portion of the wavefunction within the well.

Barrier Composition Broadening

There has been significantly less theoretical work on barrier composition broadening.[34,41-42] The GaAs/AlGaAs material system has AlGaAs barriers which can be expected to have alloy composition fluctuations. Given the high exciton confinement in this system, however,

most authors have chosen to neglect barrier composition linewidth broadening. A majority of the devices made in the InGaAsP system use InP barriers. In such cases barrier composition broadening is irrelevant and researchers working with such devices have ignored it. Some researchers, however, find various advantages in using InGaAsP barriers, and calculation of barrier composition linewidths is necessary in such cases. Hong and Singh[34] are the only authors to have theoretically considered barrier broadening, doing so for the InAlAs/InGaAs material system. However, there are several problems in interpreting their results. They give the following equation for the linewidth due to barrier composition fluctuations:

$$FWHM = 2\sqrt{\frac{1.4C_0(1-C_0)V_{wig}}{3\pi L_{eff}}}\frac{\partial E_{exciton}}{\partial C} \tag{3.21}$$

where L_{eff} is "an effective length to which the exciton wave function penetrates into the barrier and has to be calculated numerically". This definition indicates that they did not consider the composition effects on electron and hole separately. This is further indicated because they considered both barriers together rather than separately. This is inappropriate. The two barriers are not equivalent except at zero field. As field is applied, the electron shifts into one barrier while the holes shift into the opposite barrier. The linewidth contributions will differ from one barrier to the other. This study has treated

the two barriers separately. A comparison of equation 3.21 with 3.12 indicates that they have also failed to include the 0.59685 quantum mechanical correction factor.

The difference in linewidth contribution from one barrier to another and from electron to hole can be seen by looking at just the subband shifts that result when the entire barrier is changed in composition, one barrier at a time. This was done for the previous example of the 7.5 nm well and 10 nm barrier. The result is shown in Figure 3.3. The subband shift is greatest for the electron since it penetrates further into the barrier. At zero applied field the shifts due to left or right barrier changes are equivalent. As field is applied the electron moves into the right barrier and its contribution to subband shift dominates. Likewise, the hole moves into the left barrier and its contribution grows.

In the barrier, the wavefunctions generally fall off in an exponential manner. For this reason, the regions of altered composition start at the well/barrier interface and different thicknesses are used. The regions used are depicted in Figure 3.4 for the conduction band. An RTM calculation is done to determine the subband level shifts for each of four beta thicknesses. To generate smaller β steps, a curve of subband shift vs. β is piecewise quadratically fit to the four RTM calculated cases and used to generate the shifts for β regions in between. The β regions were calculated with steps of single monolayers, 2.88 Angstroms. Again, the calculations must be performed for composition changes in both x and y. The valence band is similar.

The barrier calculation is very computationally intensive. Separate RTM subband level calculations must be done for the following:

the basic composition

left barrier, x altered, four different β regions

left barrier, y altered, four different β regions

right barrier, x altered, four different β regions

right barrier, y altered, four different β regions

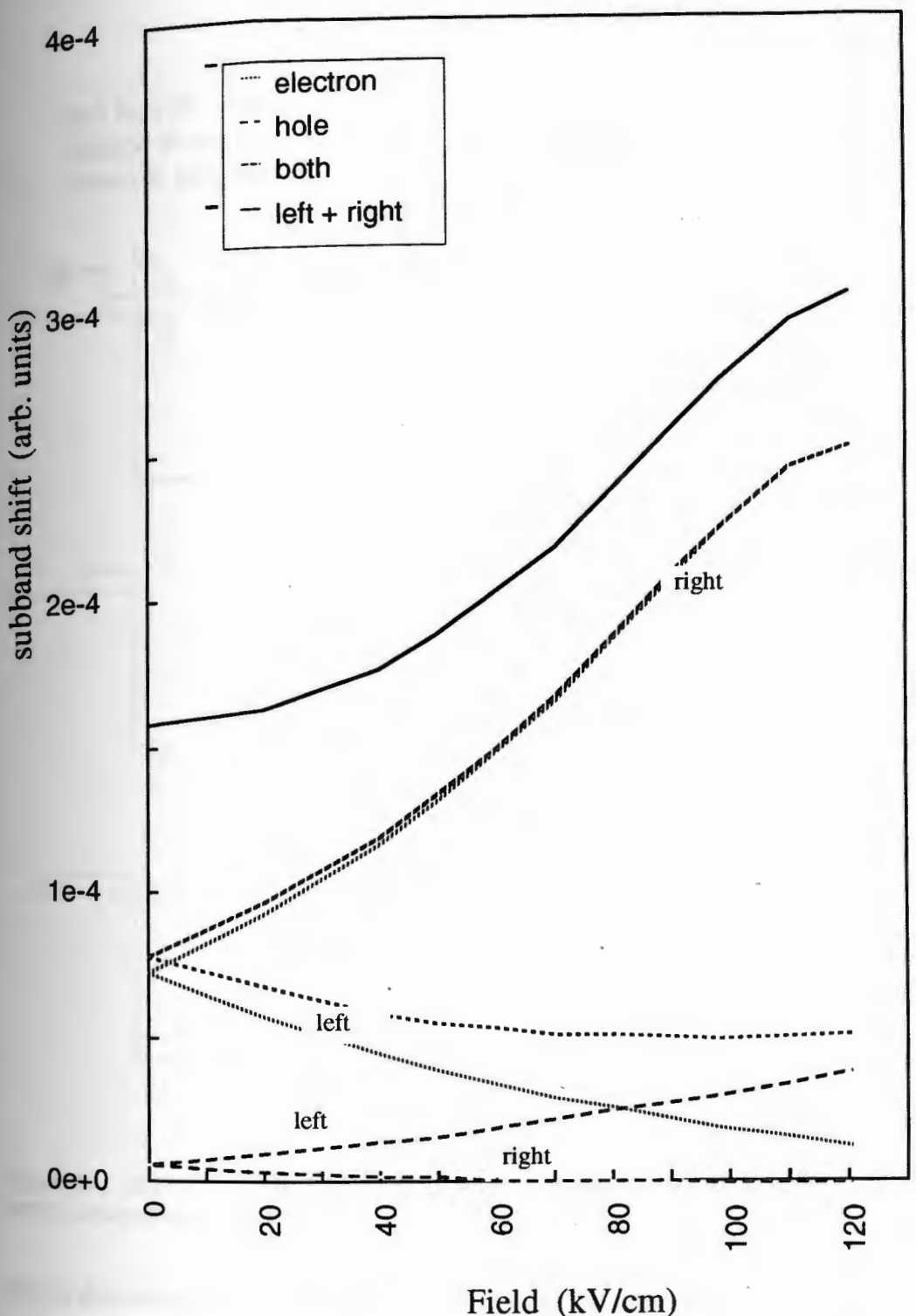

Figure 3.3. RTM subband shifts from composition changes of an entire barrier.

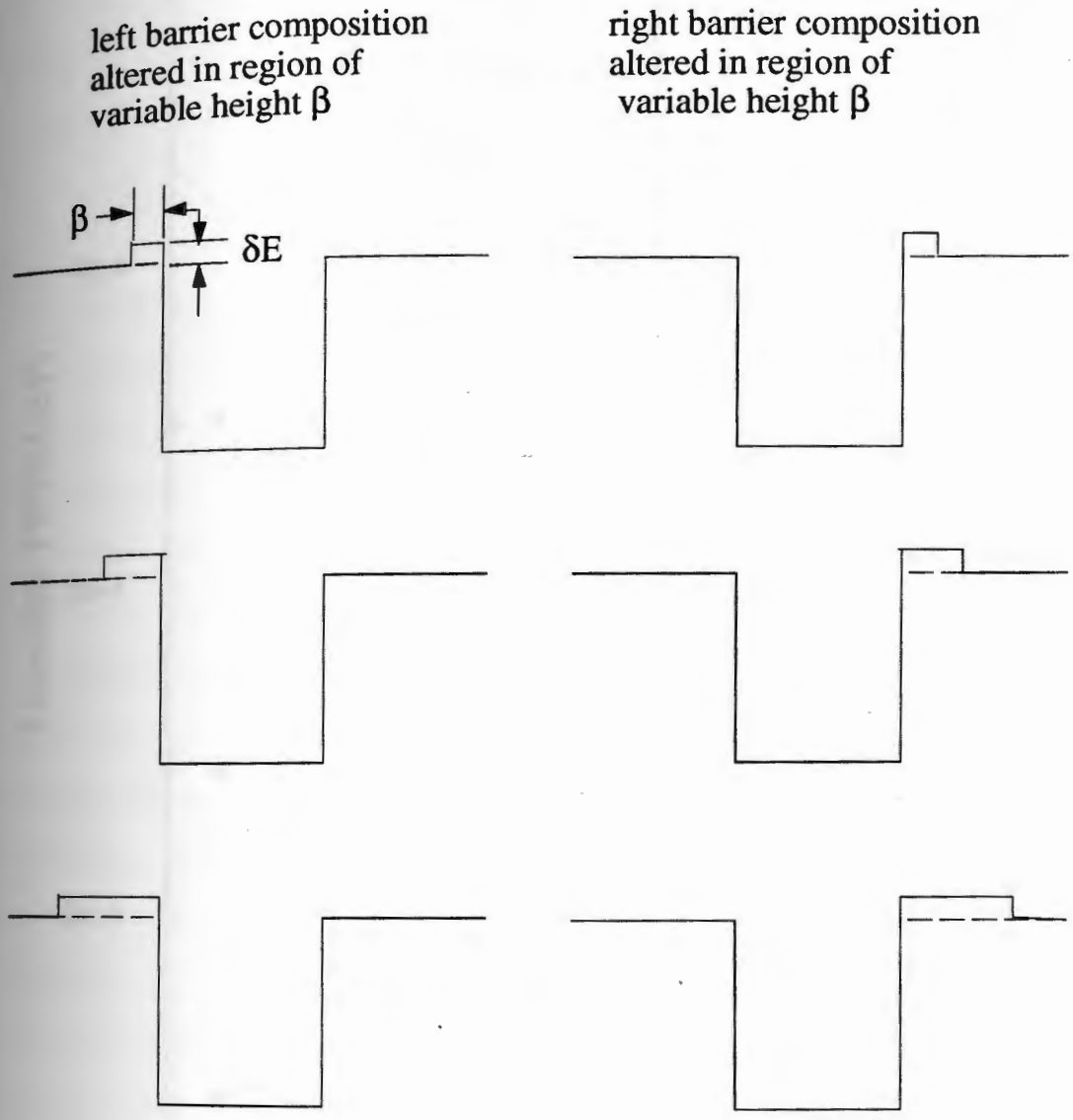

Figure 3.4. Depiction of the regions of altered composition used in the calculation of barrier composition broadening.

It is for this reason that this method was not considered appropriate for the design optimization program and a simpler approximation was sought. The first order approximation was applied by using equations 3.16 and 3.12 with the same barrier β regions as described above. Results of the two methods are shown in Figure 3.5. They

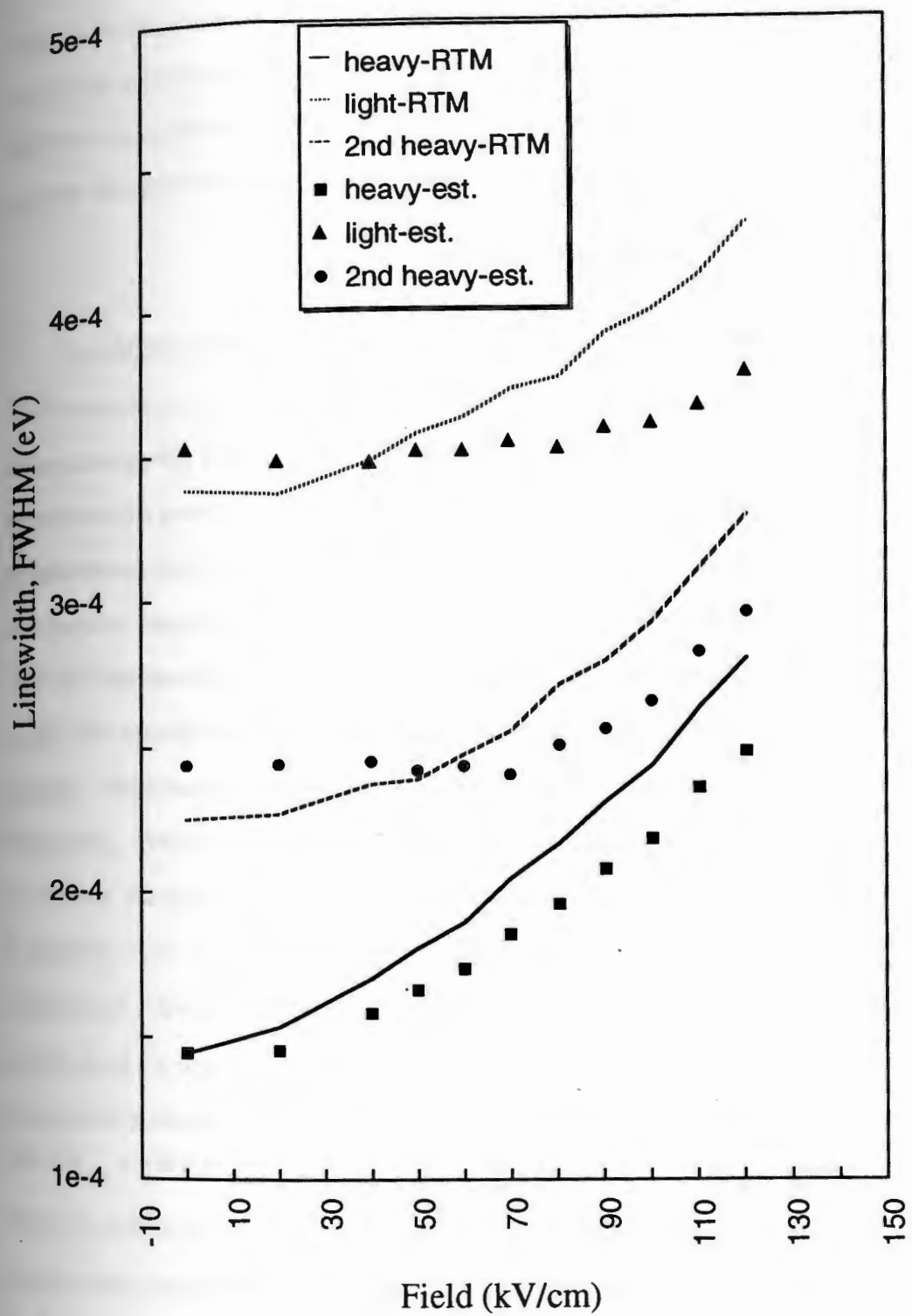

Figure 3.5. Barrier composition linewidth for the RTM method and the first order approximation.

agree surprisingly well when it is considered that the first order approximation effectively ignores the quantum well confinement nature of the problem. The agreement is also sufficient that, given the small linewidth contribution relative to other broadening sources, the estimate is acceptable for use in the modulator design optimization.

Macroscopic Composition Fluctuations

In addition to the pure or clustered alloy disorder presented thus far, there may also be macroscopic composition fluctuations where the average composition varies over dimensions greatly exceeding those of the exciton. Several authors have briefly mentioned this possibility,[37,38,43] but only one group has made experimental measurements and only one has considered these variations theoretically.[33,36,44] In the next section, analysis of Sugawara et al.'s measured linewidths for a series of quantum well and bulk samples will demonstrate the need for an additional broadening source to explain the smooth transition of linewidth from increasingly wide quantum wells to bulk samples. Macroscopic composition fluctuations is a likely candidate for such broadening. When the composition varies over dimensions greatly exceeding those of the exciton, the exciton size relative to the fluctuation size is no longer important, as it is in equation 3.12. Different excitons in different parts of the material see the local composition. Given the large number of factors that may cause composition fluctuations and the need for simplicity, a Gaussian distribution of macroscopic composition fluctuations is assumed. The resultant linewidth may be written as:

$$FWHM_{mac} = FWHM_{comp}\left[0.4\langle\psi_e|\psi_e\rangle_v + 0.6\langle\psi_h|\psi_h\rangle_v\right] \tag{3.22}$$

where v= well or barrier and $FWHM_{comp}$ is the FWHM of the gaussian distribution of macroscopic composition fluctuations. This equation was presented by Sugawara et al.,[33] though in fitting to their experimental data of linewidth versus well width they apparently neglected the wavefunction weighting and used a form that was constant with well width. The above form will vary with well width according to $\langle\psi_e|\psi_e\rangle_v$ and

$\langle \psi_h | \psi_h \rangle_v$. Thus as the well width shrinks and more of the exciton is in the barrier, the well composition broadening will decline and the barrier composition broadening increase. Sugawara et al. did not consider the application of field, but inclusion of the above factors also captures the field effect of pushing the excitons into the barriers.

Bulk Composition Fluctuations

As mentioned above, the linewidth models will later be compared to experimental data that includes quantum wells of various thicknesses and bulk semiconductors. Therefore it is necessary to derive the composition broadening for bulk semiconductors. The derivation of Singh and Bajaj[40] is presented. Returning to equation 3.3:

$$\Delta E_v = \Delta C \frac{\delta E_{exc}}{\delta C} \langle \Psi | \Psi \rangle_v \tag{3.23}$$

As before:

$$\begin{aligned} FWHM(\Delta E, V) &= 2\sqrt{\frac{1.4 C_0 (1-C_0) V_c}{V}} \frac{\delta E_{exc}}{\delta C} \langle \Psi | \Psi \rangle_v \\ \sigma &= \max_V \left(FWHM(\Delta E, V) \right) \\ &= 2\sqrt{1.4 C_0 (1-C_0) V_c} \max_V \left\{ \frac{\delta E_{exc}}{\delta C} \frac{\langle \Psi | \Psi \rangle_v}{\sqrt{V}} \right\} \end{aligned} \tag{3.24}$$

It is assumed that :

$$\frac{\delta E_{exc}}{\delta C} \approx \frac{\delta E_g}{\delta C} \tag{3.25}$$

The three dimensional exciton has a hydrogenic wavefunction:

$$\Psi(\rho) = \pi^{-1/2} \lambda^{-3/2} \exp(-\rho/\lambda) \tag{3.26}$$

The maximization over all possible volumes V is then done. The volumes V of interest are spheres of various radii centered on the exciton. The radius is written in terms of a variable parameter γ:

$$\rho = \gamma \lambda \tag{3.27}$$

The volume is thus:

$$V = \frac{4}{3} \pi \gamma^3 \lambda^3 \tag{3.28}$$

The integral over the wavefunction is calculated:

$$\langle\Psi|\Psi\rangle_V = \int_V \left|\exp(-\rho/\lambda)\right|^2 \left(\frac{1}{\pi\lambda^3}\right) d^3\rho$$

$$= \left(\frac{1}{\pi\lambda^3}\right) \int_0^{\pi} \int_0^{2\pi} \int_0^{\gamma\lambda} \exp(-2\rho/\lambda)\rho^2 \sin\theta \, d\theta \, d\phi \, d\rho \tag{3.29}$$

$$= \left[1 - \exp(-2\gamma)(2\gamma^2 + 2\gamma + 1)\right]$$

The maximum over V is found:

$$\max_V \left\{ \frac{\delta E_{exc}}{\delta C} \frac{\langle\Psi|\Psi\rangle_V}{\sqrt{V}} \right\} \approx \frac{\delta E_g}{\delta C} \max_\gamma \left\{ \frac{\left[1 - \exp(-2\gamma)(2\gamma^2 + 2\gamma + 1)\right]}{\sqrt{\frac{4}{3}\pi\gamma^3\lambda^3}} \right\} \tag{3.30}$$

$$\approx \frac{\delta E_g}{\delta C} \left(\frac{4}{3}\pi\lambda^3\right)^{-1/2} \max_\gamma \left\{ \frac{\left[1 - \exp(-2\gamma)(2\gamma^2 + 2\gamma + 1)\right]}{\gamma^{3/2}} \right\}$$

The maximum over g is found to occur at g=1.16 with a value of .3276. Finally:

$$\sigma = 2\sqrt{\frac{1.4C_0(1-C_0)V_c}{\frac{4}{3}\pi\lambda^3}} \frac{\delta E_g}{\delta C}(0.3276) \tag{3.31}$$

Well Width or Interface Fluctuations

It is well known that the interfaces in a quantum well are not perfect. The growth interruption at the interface leaves monatomic island-like step variations in the surface. Several researchers[45-47] have studied these islands and the growth conditions that affect their characteristics. Bimberg et al.[46] report the imaging of monolayer islands in GaAs/AlGaAs interfaces by cathodoluminescence imaging. They found single monolayer islands with mean sizes of 6 to 8 microns, which were reduced to 2 microns when growth temperature was increased from 600°C to 660°C. Similar studies of InGaAsP interfaces are not available but it can be assumed that they will exhibit similar interface fluctuations. These interface fluctuations result in a variation in the quantum well width which directly affects the exciton energy.

The theory of well width or interface fluctuation broadening was first presented by Singh and Bajaj.[42] They stated that the linewidth (FWHM) is given by:[42,48]

$$FWHM_{ww} = \alpha FWHM_{island} \left.\frac{\delta E_{exc}}{\delta w}\right|_{w_0} \delta \qquad (3.32)$$

where $FWHM_{island}$ is the FWHM of the gaussian random distribution of island heights given in units of monolayers, δ is the monolayer thickness, and $\left.\frac{\delta E_{exc}}{\delta w}\right|_{w_0}$ is the variation in exciton energy with well width. α is a factor that approaches 1 as the island size approaches the exciton size. Given the size of islands found by Bimberg et al.[46] and other researchers, α is often omitted. The variation of exciton energy with well width is found by a variety of means, usually by the same method used to initially determine the subband levels. In this work the RTM was used. A separate level calculation was performed for the case of a well with slightly altered width and the resultant levels were compared to the normal subband levels. Different size alterations to the step size were tried to ensure that the derivative converged. It was found that 1 or 2 angstrom alterations were sufficient while minimizing the extra computational effort needed to resolve steps this small.

Figure 3.6 shows a typical result for the 7.5 nanometer well case given before. Here the linewidth increases with field. The field pulls the electron and hole wavefunctions toward the barrier, increasing the wavefunction at the interface. This linewidth is also highly dependent upon well width because the wavefunctions are higher at the interface for narrower wells. The above equation may also be used to describe the broadening from random variation in well width from well to well within the multi-quantum well stack. Some fabrication error in well width is to be expected.

Comparison of Linewidth Theory with Published Experimental Data

The existing theoretical work on exciton linewidth is largely unverified. Many of the broadening mechanisms appear to be of similar magnitude and it is difficult to sort out

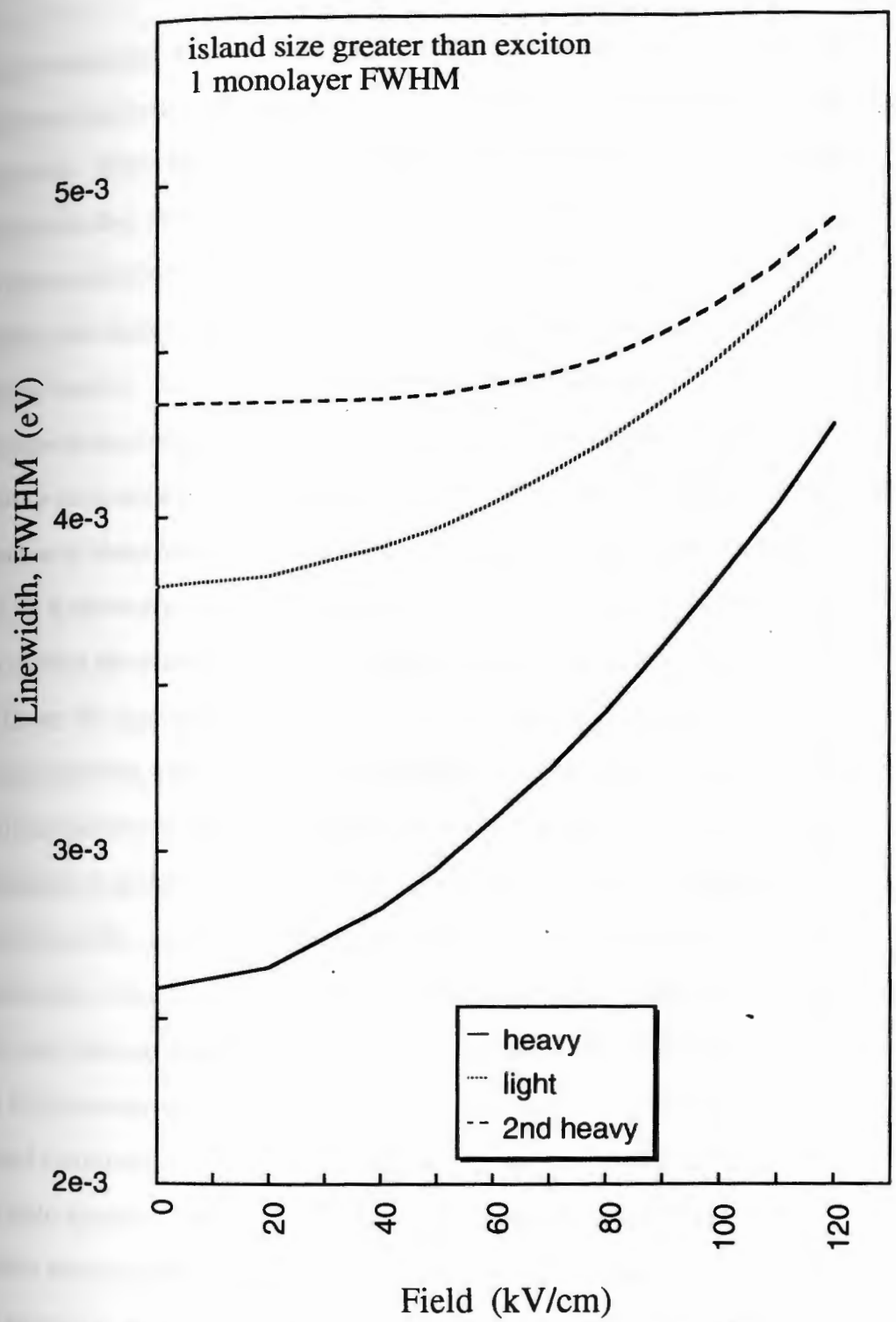

Figure 3.6. Well width fluctuation broadening. Well=7.5 nm, Barrier=10nm.

which ones dominate. In the equations presented in the last chapter there are several undetermined parameters, mostly associated with the fabrication quality of the multi-quantum well. Given the usual lack of detailed data on such quality factors, and the possibility that they vary from manufacturer to manufacturer or even from wafer to wafer, these parameters may be considered fitting parameters. In the composition broadening, the cluster volume is undetermined. Practical devices may exhibit clustering in wells or barriers. The macroscopic composition fluctuation depends on the distribution of macroscopic composition fluctuations, also unknown. The FWHM of this distribution becomes a fitting parameter. For the interface fluctuations, the FWHM of the distribution of island heights for each interface is unknown and varies from sample to sample. It is necessary to compare the theory with the best available measured linewidth data to confirm the theory and determine typical values for these fitting parameters.

Given the large number of broadening factors, and the complex manner in which they vary with field, composition, and well width, it is perhaps not possible to design a series of measurements capable of fully discriminating between the effects. Future developments in measurement techniques may resolve this problem. One of the best series of linewidth measurements was reported by Sugawara et al.[18] for InGaAsP/InP quantum wells. Using carefully controlled metal organic vapor phase epitaxy (MOVPE) growth, they fabricated sets of single quantum well samples with well widths varying from 1 to 20 nanometers and well composition varying from y=0.6 to 1.0. They also fabricated corresponding bulk samples. Finally they fabricated a limited number of 20 period multi-quantum wells for comparison to ensure that the multi-quantum well linewidths were dominated by effects at the single well level. The variation in well width allows broadening effects which vary in well width dependency to be discriminated. The bulk samples eliminate interface broadening and barrier composition altogether. They then performed photoluminescence spectral measurements for each sample, at 4.2K. The

low temperature eliminated the effects of thermal broadening, leaving only the inhomogeneous broadening factors. The photoluminescence measurements were made by exciting the samples with a Krypton laser at 647.1 nanometers. The samples were immersed in liquid Helium. The photoluminescence was dispersed by a monochrometer and detected using a lock-in technique.

Figures 3.7 and 3.8 shows the Sugawara et al.[18] data for linewidth versus well width. The linewidth shown is the FWHM of the heavy hole exciton at zero applied field. Also shown by an open symbol is a 20 period multi-quantum well sample. The close agreement in linewidth between the MQW and the single well samples shows that the linewidth for these samples is dominated by effects at the single well level. This rules out such possible broadening mechanisms as lack of well width uniformity. In general it will not be possible to rule out such mechanisms for other samples. The data point labeled as bulk is a 200 nm thick layer.

Figures 3.7 and 3.8 include curves showing the newly calculated theoretical linewidth fit and the various contributions to linewidth. Equations 3.32, 3.12, 3.31, and 3.22 are used for the well width, random composition, random bulk composition , and macroscopic composition linewidth respectively. Barrier composition broadening was not included because of the non-alloy InP barriers. Temperature broadening was not included because the measurements were at 4.2K.

For the composition broadening, separate x and y composition calculations were done, where x and y are the species factors in the $In_{1-x}Ga_xAs_yP_{1-y}$ alloy composition. The x and y composition fluctuations are assumed to be independent and to exhibit Gaussian lineshapes. Their linewidths are thus combined as:

$$FWHM_{tot}^2 = FWHM_x^2 + FWHM_y^2 \tag{3.33}$$

The random composition, macroscopic composition, and well width broadening are likewise assumed to be independent with Gaussian lineshapes. They were combined as:

$$FWHM_{tot}^2 = FWHM_{comp,ran}^2 + FWHM_{mac}^2 + FWHM_{ww}^2 \tag{3.34}$$

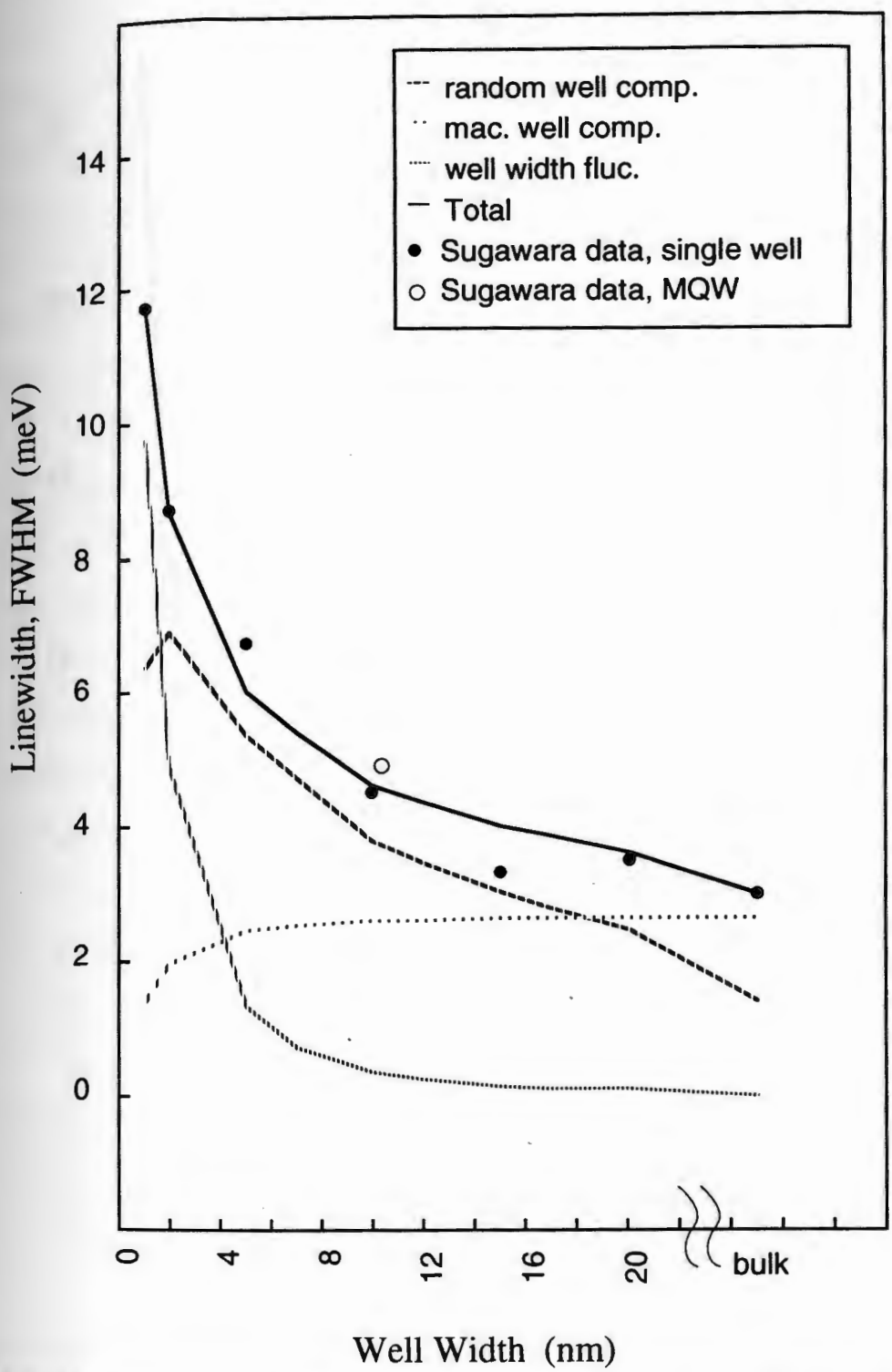

Figure 3.7. Linewidth vs. well width. Theoretical fit to Sugawara et al. data at 4.2K. Well y=1.0.

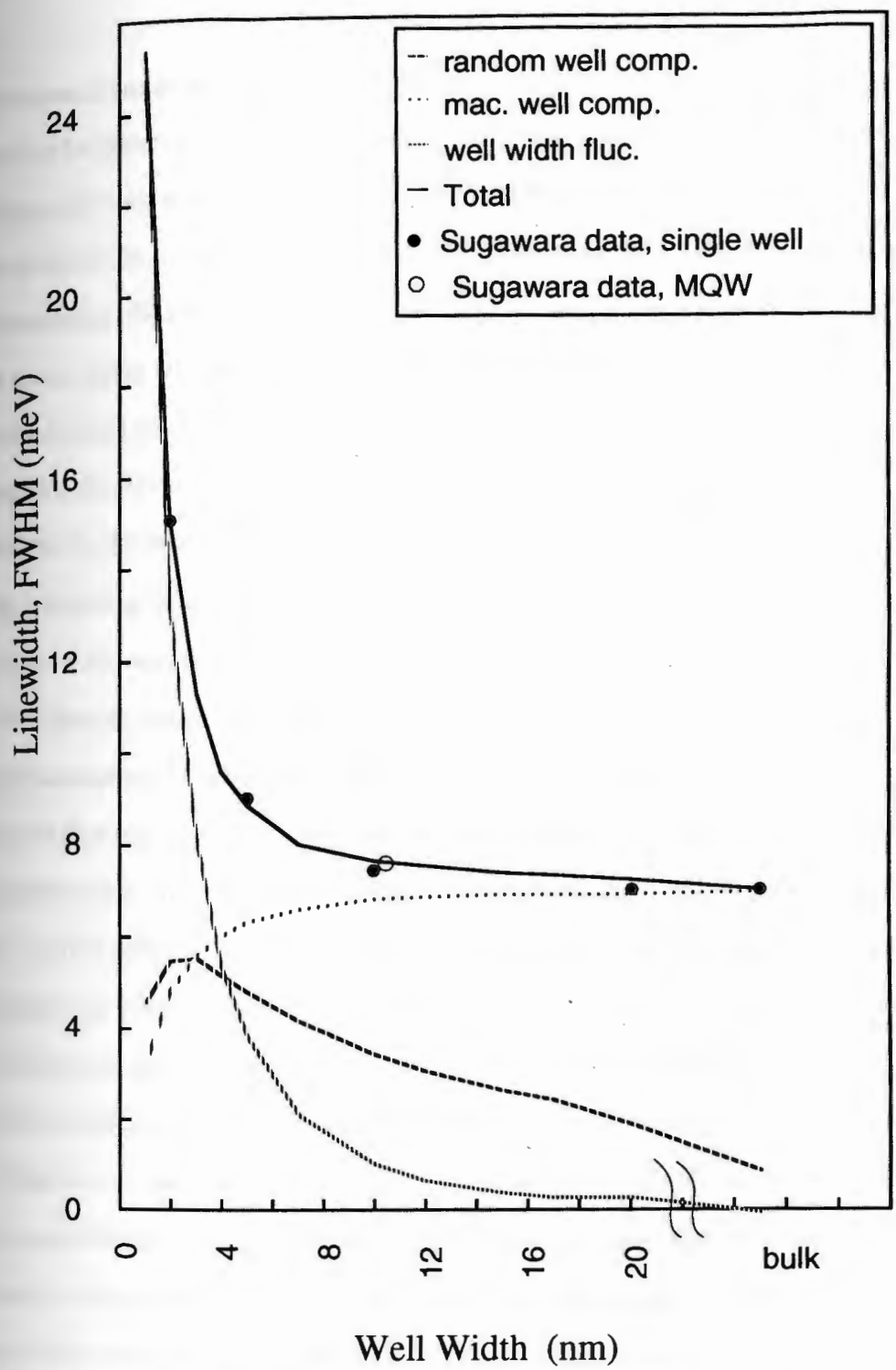

Figure 3.8. Linewidth vs. well width. Theoretical fit to Sugawara et al. data at 4.2 K. Well y=0.6.

Each component has an associated variable parameter: cluster volume for random composition broadening, $FWHM_{comp}$ for macroscopic composition broadening, and $FWHM_{island}$ for well width broadening. These were chosen to give the best fit of the theoretical linewidth to the data. The result is that the narrow well data indicates the well width broadening, the additional broadening in the mid-well-size region indicates the random composition broadening, and the bulk data indicates the macroscopic composition broadening. Resulting cluster volumes were 2.5 and 1.5 times the volume per cation for the y=1.0 and 0.6 cases respectively. The volume per cation is given by $a_0^3/4$ where a_0, the lattice constant, is that of the InP to which the MQW is lattice matched. Resulting values for $FWHM_{island}$ are 0.19 and 0.73 monolayers for y=1.0 and y=0.6 respectively using a value of 2.9344 angstroms per monolayer.

The random composition broadening is seen to increase with reduced well width due to the associated shrinkage of the exciton volume. The smaller wells confine the electron and hole closer to each other, increasing the binding energy and resulting in a smaller exciton size. It is more likely to realize a composition fluctuation across a smaller volume. At very small well widths the exciton penetrates into the barrier and the random well composition broadening drops. The well width broadening is non existent for the bulk which has no interfaces. It is still very low for large well widths but rises rapidly at small well widths because the wavefunction at the interface is greater in such wells.

These two linewidth contributions are not sufficient to describe the data because both decrease with large well width, while the data becomes flat. Sugawara et al.[18] introduced a macroscopic broadening term which was independent of well width and chosen to fit the bulk linewidth result. There is considerable evidence for macroscopic broadening. Schubert and Tsang[48] and then Sugawara et al.[18] have reported a variation in exciton low temperature photoluminescence lineshape and linewidth with excitation power density. At lower power densities the line shape becomes asymmetric and the

linewidth smaller. It has been explained that the decrease in excitation power increases the exciton recombination lifetime and hence the diffusion length of the excitons. The excitons then preferentially recombine in lower energy regions. The high energy part of the lineshape is thus lost, resulting in a narrower asymmetric lineshape.

The present work uses a new equation for macroscopic composition fluctuation linewidth, equation 3.22. It accounts for the fact that macroscopic composition broadening should not be independent of well width because, as well width decreases, less of the exciton is located in the well to be affected by composition fluctuations there.

In the next chapter, comparison of a full absorption spectra model with experimental data from Zucker et al.[19] and unpublished data from Siemens will be presented. The linewidths are quite different between the Sugawara,[18] Zucker,[19] and Siemens data. Both the Zucker and the Siemens devices demonstrate much worse linewidth. This is more than can be accounted for by thermal broadening in the room temperature spectra. The Zucker and Siemens data were also quite different, with the Zucker linewidth remaining essentially unchanged with applied field while the Siemens linewidth increased with field. It appears that at the present stage of development of InGaAsP devices, there is great variability in the process control and accuracy of fabrication achieved. Different manufacturers may have quite different levels of the various linewidth factors. Accuracy of linewidth measurements is also somewhat questionable. While MQW stacks of many layers have been used in measurements with the GaAs/AlGaAs system, most measurements with InGaAsP have used far fewer quantum wells.[18,19] The total absorption length is thus reduced, leading to poorer signal to noise ratio in the spectral absorption measurements.

In conclusion for this chapter, a number of line broadening effects have been theoretically modeled. The composition broadening model was derived based on a model by Hong and Singh[34] but including a quantum mechanical correction factor and

implemented through the resonant tunneling method for the first time. A simplified method was also developed based on assuming that the change in energy levels is directly related to the energy gap change alone. Results for the two models were compared and the simplified model was shown to be sufficiently accurate for use in device design optimization. A barrier composition broadening model was also developed, which for the first time correctly treats the exciton as a two particle system with the electron and hole penetrating differently into opposite barriers under an applied field. The effect of macroscopic composition fluctuations was considered, with the variation with well width and applied field included. The theoretical linewidth model was compared to experimental results of Sugawara et al.[18]

CHAPTER 4

MODELING OF ABSORPTION SPECTRA

In this chapter the theoretical background of chapters one through three will be applied to modeling the absorption spectra and associated index change in InGaAsP MQW modulators. This model will be compared against published data from Zucker et al.[19] and unpublished data from Siemens researchers.

Most authors to model the absorption spectra to optimize modulator device design have modeled only the exciton absorption, neglecting the continuum.[6,22] This will be shown to be inadequate, especially in the case of InGaAsP, where at high field the exciton may almost fade into the continuum. Stephens et al.[16] included continuum absorption in modeling GaAs/AlGaAs and Bandyopadhyay and Basu[23] followed their approach for InGaAsP devices. They used the following expression for the absorption spectra prior to convolution with the inhomogeneous broadening function:

$$\alpha(\hbar\omega,F)=\left|\langle\Psi_e|\Psi_h\rangle\right|^2 q_{ex}L(\hbar\omega,E_{cv}(F)-E_b(F)) + \int_{E_{cv}}^{\infty}\left|\langle\Psi_e|\Psi_h\rangle\right|^2 N q_{con}K(E',E_{cv}(F))L(\hbar\omega,E')dE' \tag{4.1}$$

where L is a Lorentzian function representing homogeneous broadening, E_{cv} is the energy separation of the electron and hole subband levels, E_b is the binding energy, q_{exc} is the exciton oscillator strength, N is the density of states, and q_{con} is the continuum oscillator strength which was fit to the data. K is the Sommerfeld factor which is given by:

$$K=\frac{2}{1+\exp\left[-2\pi R_y^{1/2}/(\hbar\omega-E)^{1/2}\right]} \tag{4.2}$$

where R_y is the three dimensional Rydberg constant:

$$R_y=\frac{e^4\mu}{32\pi^2\varepsilon^2\hbar^2} \tag{4.3}$$

The Sommerfeld factor represents the enhancement in the continuum due to considering the coulomb interaction. It was first derived for the three dimensional exciton by Elliot.[50] Unlike the MQW case, the three dimensional and the pure two dimensional exciton problems can be solved analytically within the effective mass approximation. In doing so, Elliot showed that the solution was a series of exciton lines. These became more closely spaced and dropped in intensity as the bandedge was approached, forming a quasi-continuum which blended smoothly into the true continuum above the band edge. In chapter two we derived the absorption between unbounded states in a MQW, neglecting any Coulomb interaction between the electrons and holes. It is straightforward to derive a similar result for the three dimensional bulk semiconductor. The ratio of Elliot's absorption to that with the no-interaction derivation gives the three dimensional Sommerfeld factor. Shinada and Sugano[51] derived the absorption for the pure two dimensional exciton. Their Sommerfeld factor is given as equation 4.2. It gives an enhancement by a factor of two at the band edge and fades to no enhancement far above the band edge. Calculations by Chan[52] suggest that for a MQW the Sommerfeld factor may be less than two. With this in mind a variable Sommerfeld factor has been used:

$$K_{var} = \frac{1+\eta}{1+\eta\exp\left[-2\pi R_y^{1/2}/(\hbar\omega - E)^{1/2}\right]} \tag{4.4}$$

with values of η between zero and one.

A major drawback of the work of Stephens et al.[16] and Bandyopadhyay and Basu[23] is that they used a fixed ratio for the oscillator strengths:

$$\frac{q_{ex}}{Nq_{con}} = 12R_y \tag{4.5}$$

This value for the ratio is between the values for a pure three dimensional or pure two dimensional case. They maintain the same ratio, even when the applied field changes. This is equivalent to assuming that the exciton does not change size or binding energy with field.

The ratio of oscillator strengths is directly available from equations (2.14) and (2.33).

$$\frac{q_{ex}}{Nq_{con}} = \frac{2|\Phi_1(0)|^2}{N} = \frac{4\hbar^2}{\mu\lambda^2} \tag{4.6}$$

The ratio is seen to be quite sensitive to the exciton size. Thus, this ratio may be the most sensitive measure of lambda available because the binding energy is small and only linearly dependent upon lambda. Exciton size varies with applied field and this should have important impact on the above ratio. For these reasons, the following form for the absorption spectra was initially used in this study:

$$\alpha(\hbar\omega, F) = \left|\langle \Psi_e | \Psi_h \rangle\right|^2 \left(\frac{R}{\lambda(F)^2}\right) Nq_{con} L(\hbar\omega, E_{cv}(F) - E_b(F)) + \int_{E_{cv}}^{\infty} \left|\langle \Psi_e | \Psi_h \rangle\right|^2 Nq_{con} K_{\text{var}}(E', E_{cv}(F)) L(\hbar\omega, E') dE' \tag{4.7}$$

The normalized Lorentzian function is:

$$L(\hbar\omega, E) = \frac{\sigma_{\text{hom}}}{\pi\left[(\hbar\omega - E)^2 + \sigma_{\text{hom}}^2\right]}$$

where σ_{hom} is the homogeneous linewidth due to tunneling.

For each applied field an RTM calculation is performed. This gives the subband levels and hence E_{cv}. It also gives the electron and hole wavefunctions which are used to calculate the overlap integral $\langle \Psi_e | \Psi_h \rangle$. The variational method described in chapter one is used to determine the binding energy and exciton lateral size, λ.

The RTM calculation was performed separately for the electron, heavy hole, and light hole. Three exciton transitions were included in the spectra. The 1e:1hh transition was between the first electron subband and the first heavy hole subband. Also included were the 1e:1lh and the 1e:2hh transitions. Many researchers only include the 1e:1hh transition because they are only interested in the leading edge of the absorption.[6,22] In the next chapter we will perform our device optimization assuming that a fixed drive voltage is available. Many of the designs in question drive the devices into the region beyond the heavy hole exciton where the light hole exciton absorption is also important.

In addition, a Kramers-Kronig calculation of index change will be used to determine the chirp performance of the modulators. In such a calculation, a light hole absorption feature at higher energy contributes significantly to the index change at lower energies. It is therefore important to include the light hole exciton. The 1e:2hh exciton was found to fall at almost the same energy as the 1e:lh. It is initially a forbidden transition at zero field. The electron wavefunction is symmetric and the second heavy hole wavefunction is assymetric, giving zero for the overlap integral. As field is applied, however, this is disturbed and the overlap integral grows so that the 1e:2hh exciton is a significant contribution to the spectrum at high fields.

Most researchers have not included tunneling induced broadening. Most of the work on MQW absorption has been focused on the GaAs/AlGaAs system which has greater confinement of the electron. The bandgap difference split is less optimal in the InGaAsP system, giving a significantly shallower well for the electrons. In addition, there are differences for those working within the InGaAsP system. Many researchers use InP barriers with InGaAsP wells. Bandyopadhyay et al.[23] did so and calculated that the tunneling induced broadening was always less than 10^{-4} eV. Others use different compositions of InGaAsP for both well and barrier. In such cases the confinement is less and more tunneling can be expected. A subroutine that is part of the RTM calculates the width of each resonance in the RTM transmission. This width is directly related to the tunneling of the particles out of the well. Figures 4.1 and 4.2 show a closeup of one subband resonance for two values of tunneling. A Lorentzian lineshape is included for comparison. It can be seen that the lineshape as given by the RTM is indeed approximately Lorentzian, especially for low tunneling. It was found that tunneling sometimes contributed noticeable additional linewidth at high fields and should be included.

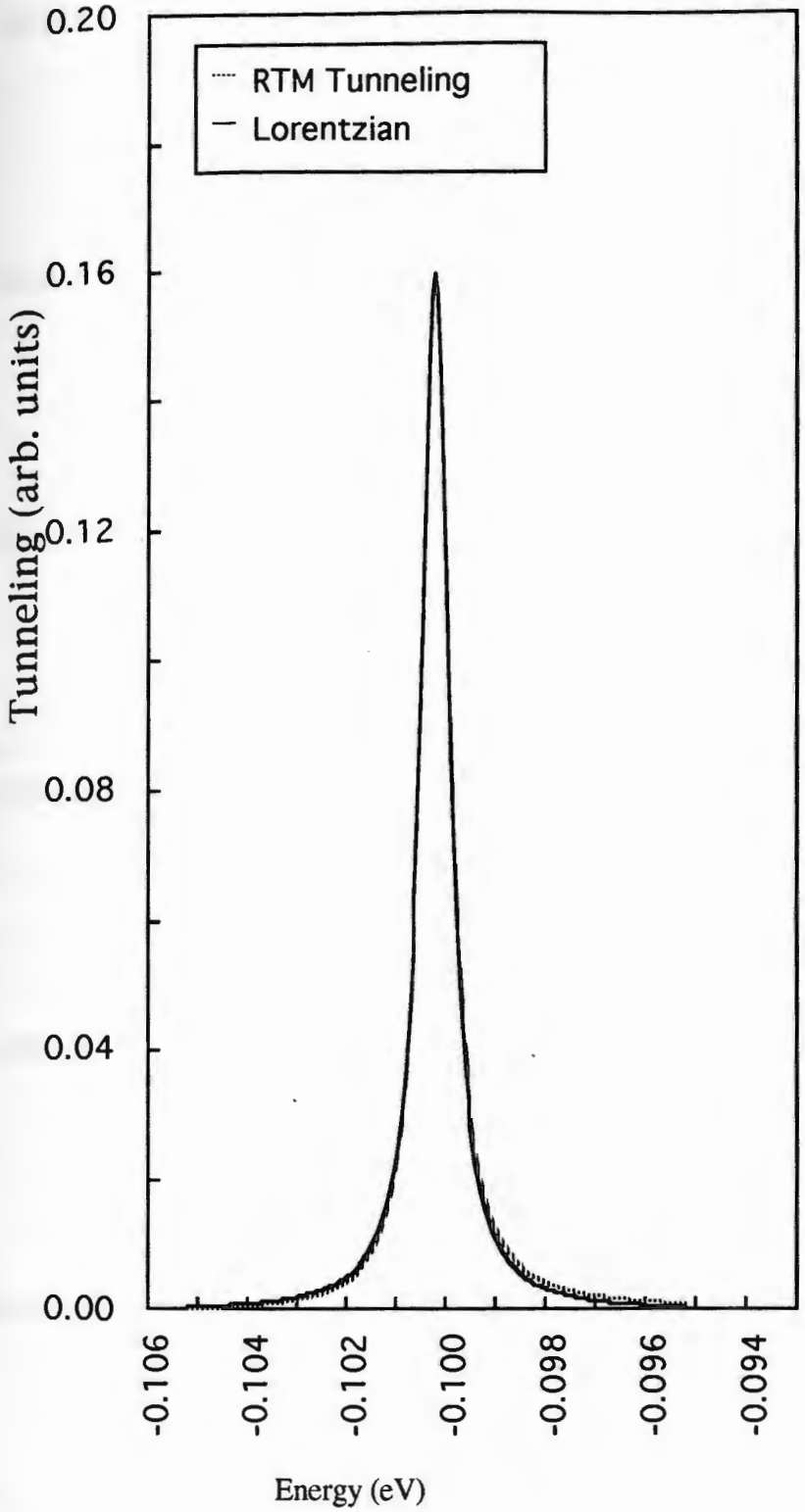

Figure 4.1. RTM tunneling resonance. 7.5 nm well with 10 nm barrier, well y=.82, barrier y=.23, applied field = 100 kV/cm. FWHM=0.7 meV.

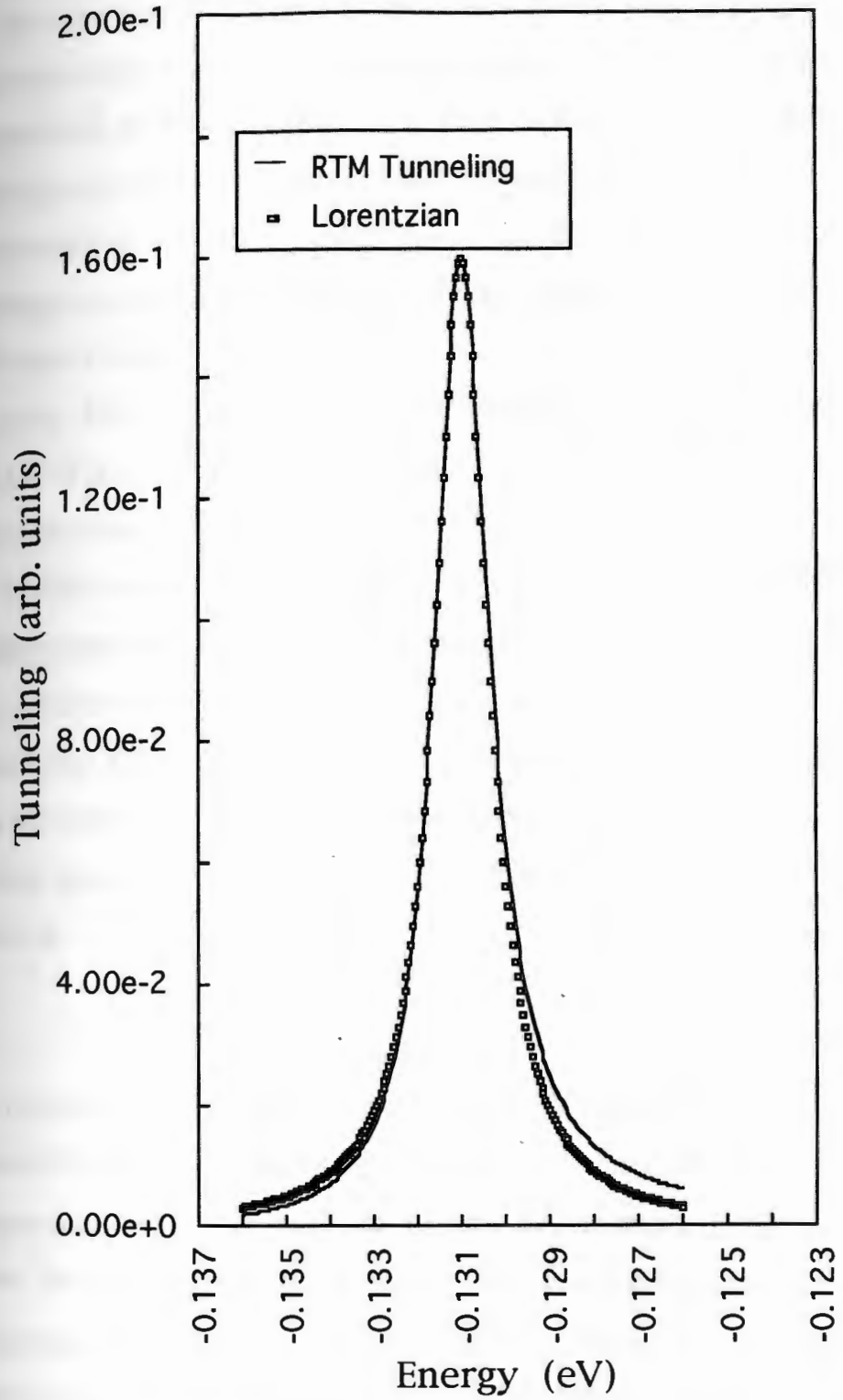

Figure 4.2. RTM tunneling resonance. 7.5 nm well with 10 nm barrier, well y=.82, barrier y=.23, applied field = 120 kV/cm. FWHM=1.6 meV.

The expression in equation 4.7 is convolved with a Gaussian lineshape representing the inhomogeneous and thermal broadening. The linewidth of the Gaussian is a combination of thermal, random composition broadening, macroscopic composition broadening, and well width broadening. The well width broadening can represent either interface roughness or variation in well thickness in a MQW stack. The thermal broadening is not expected to vary much from manufacturer to manufacturer. Sugawara et al.[36] found a thermal FWHM of 8.9 to 9.2 meV and values of 9 to 9.5 meV were used in this study. The fitting parameters for the other broadening factors were varied in order to find a combination which fit the experimental zero-field spectra, and continued to fit as the linewidth changed with applied field.

Typical calculated spectra illustrate the importance of using a full absorption spectrum to evaluate any theoretical model. Many researchers have not compared the full spectra, but have tried to read the exciton shifts, or exciton heights, or linewidths from measured data. Figures 4.3 and 4.4 show a typical absorption spectrum and the separate exciton and continuum contributions. It can be seen that the exciton positions are not where they appear to be from the full spectrum. Neither are the linewidths what they appear to be.

Zucker Data

The first experimental data to be evaluated is from Zucker et al.[19] Their sample B consisted of five periods, with a 70 angstrom well of 1.33 μm composition InGaAsP and 250 angstrom barriers of InP. They estimated their total intrinsic layer thickness, d_i, as 1.16 μm. Their absorption spectra were taken with a broadband optical source and a grating spectrometer. Figures 4.5 through 4.8 show an initial fit of the measured spectra to the theory for various applied reverse bias voltages. The magnitude drops too fast with applied field, partially disguising that the shift and linewidth are well matched.

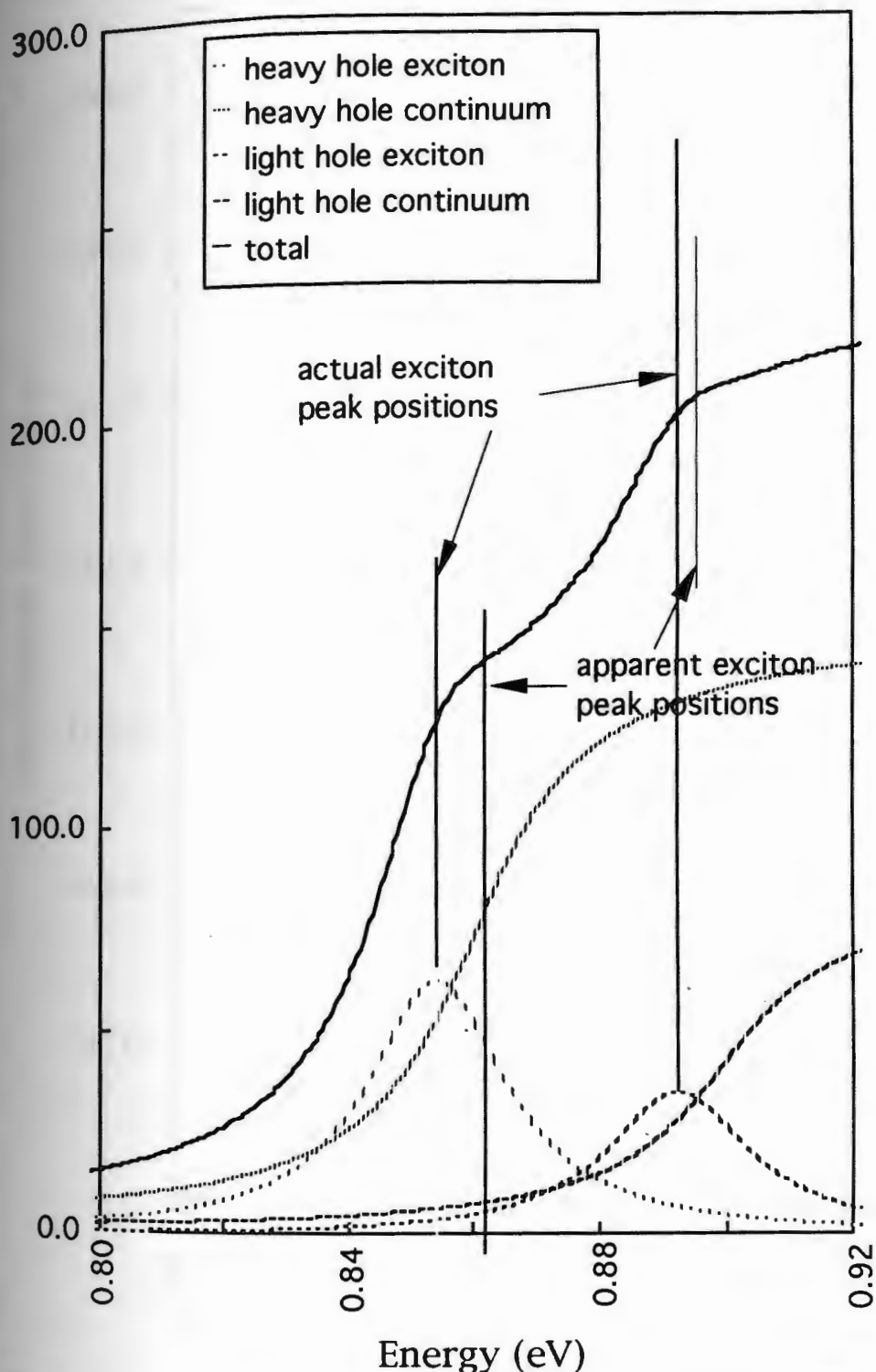

Figure 4.3. Typical absorption spectrum with components illustrating difficulty in determining exciton location. Linewidth=10 meV.

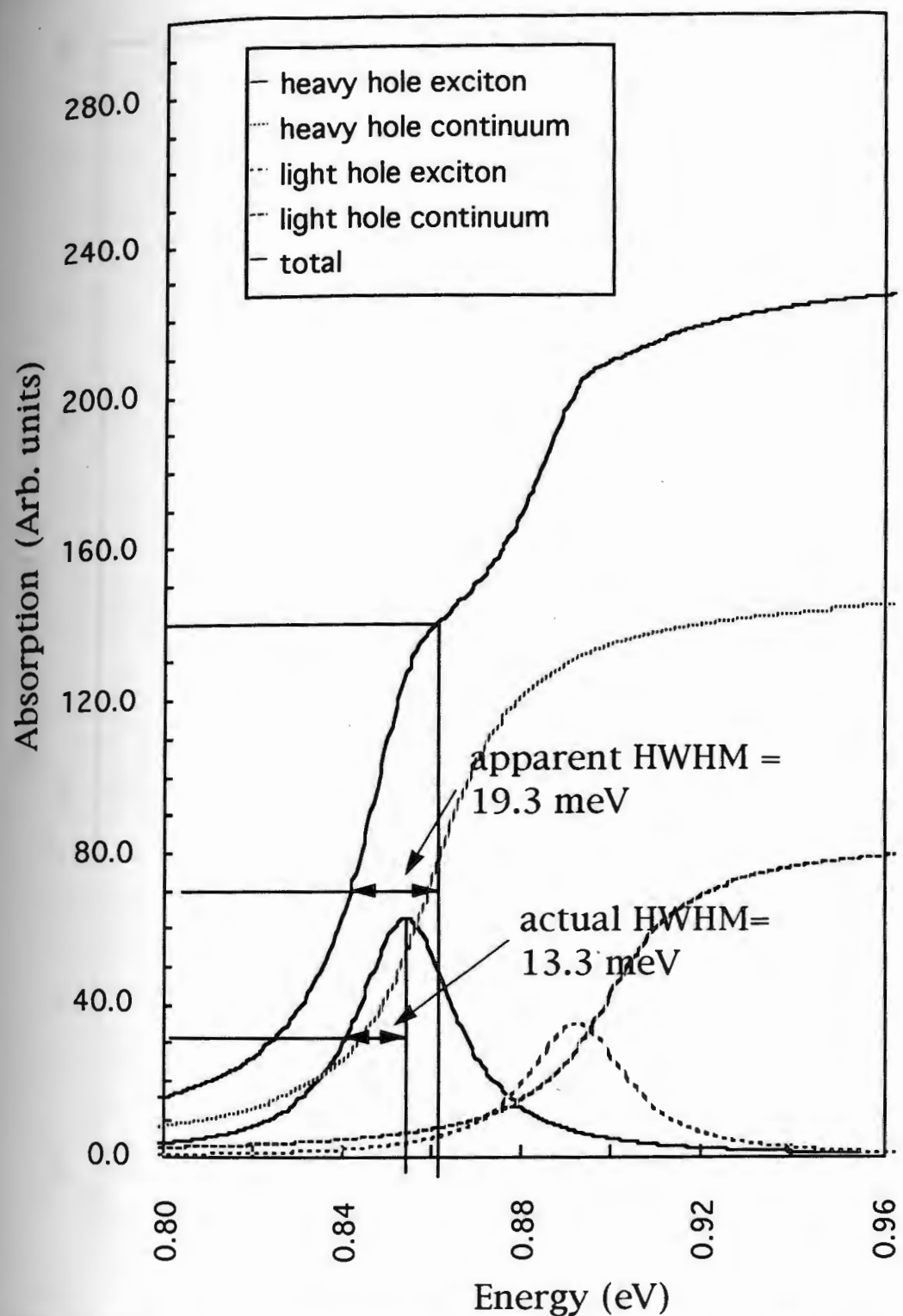

Figure 4.4. Typical absorption spectrum with components illustrating difficulty in determining linewidth.

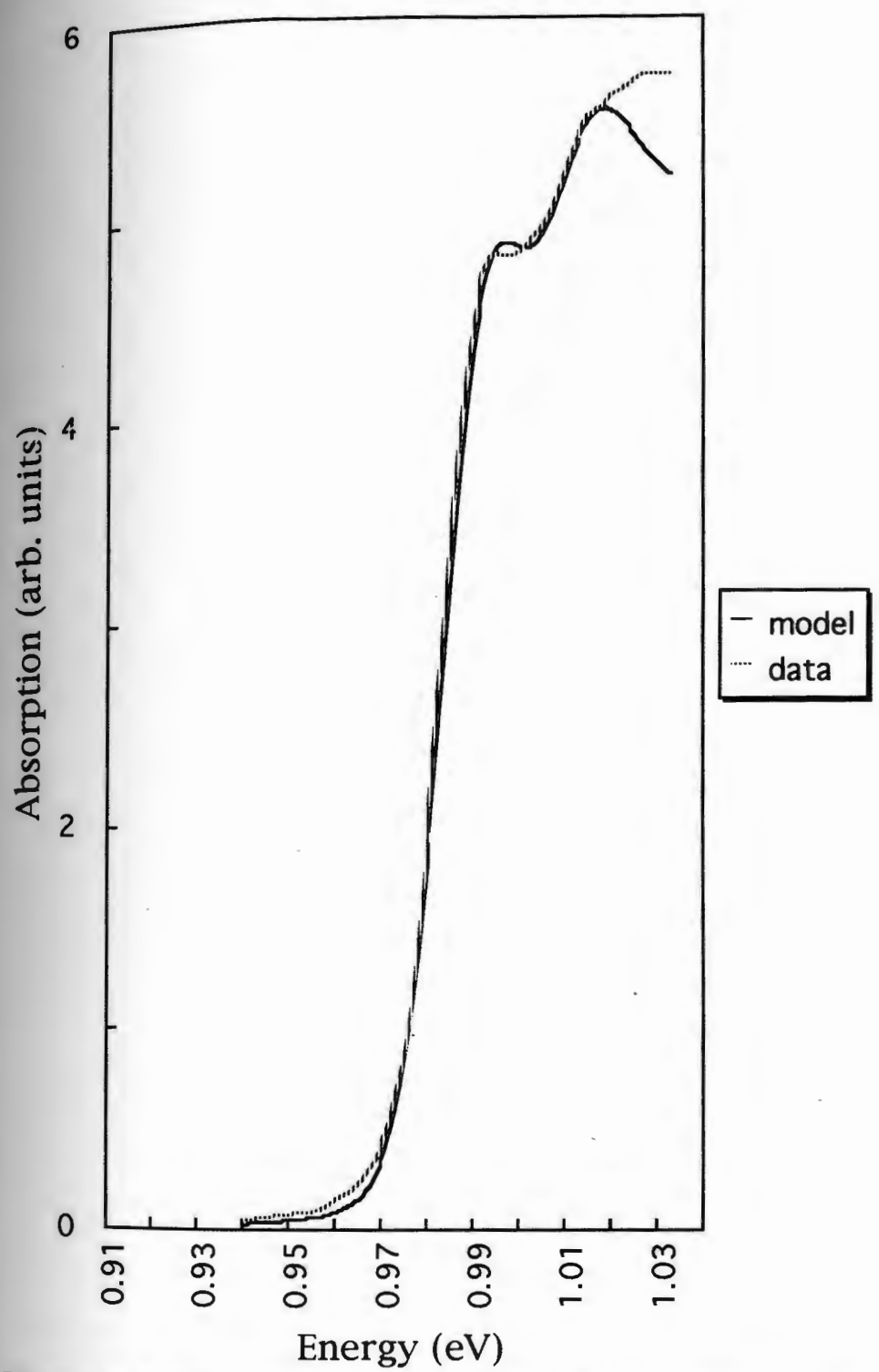

Figure 4.5. Model comparison with Zucker data. 0 Volts applied. 40/60 conduction/valence band split.

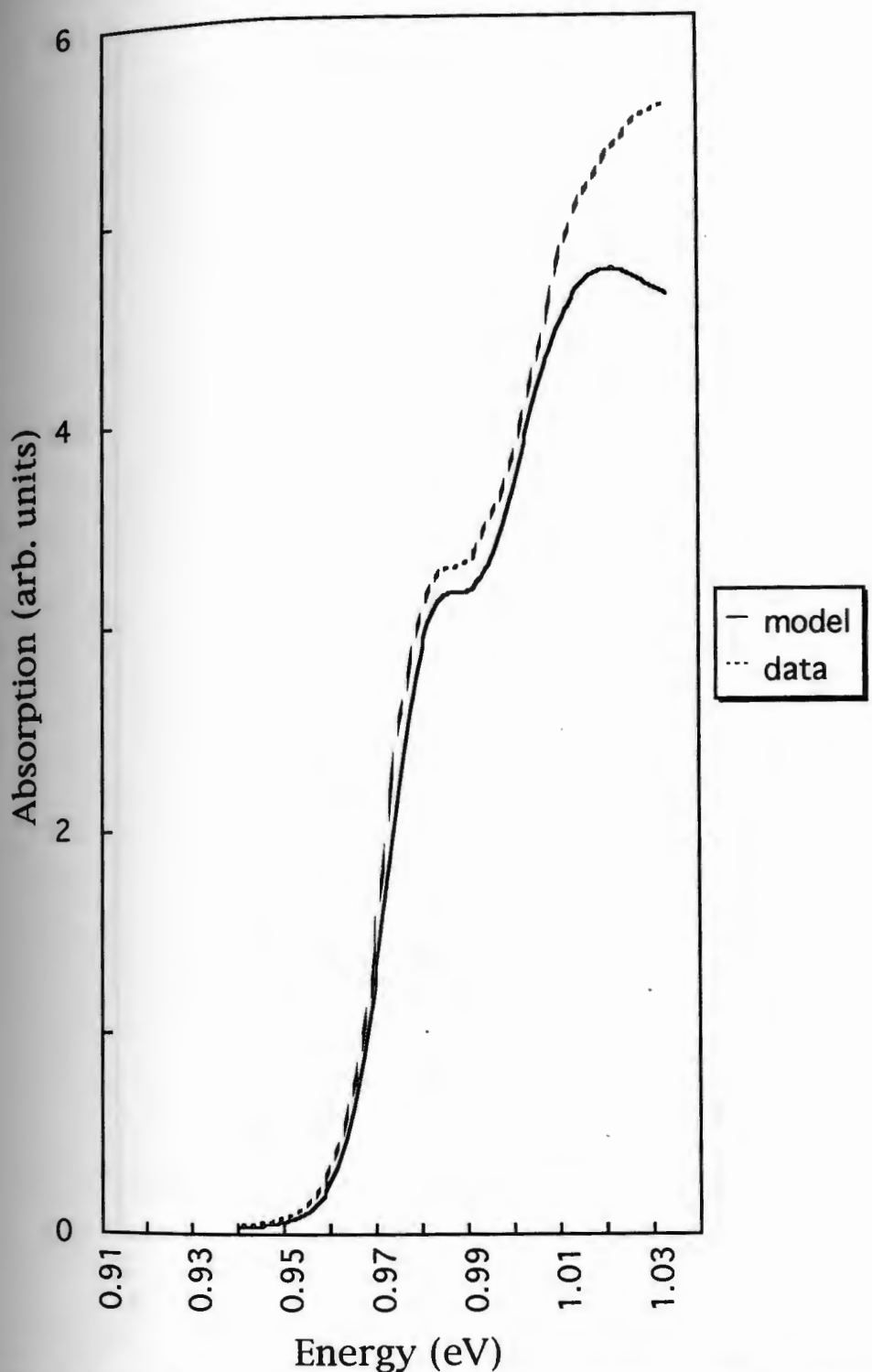

Figure 4.6. Model comparison with Zucker data. 10 Volts applied. 40/60 conduction/valence band split.

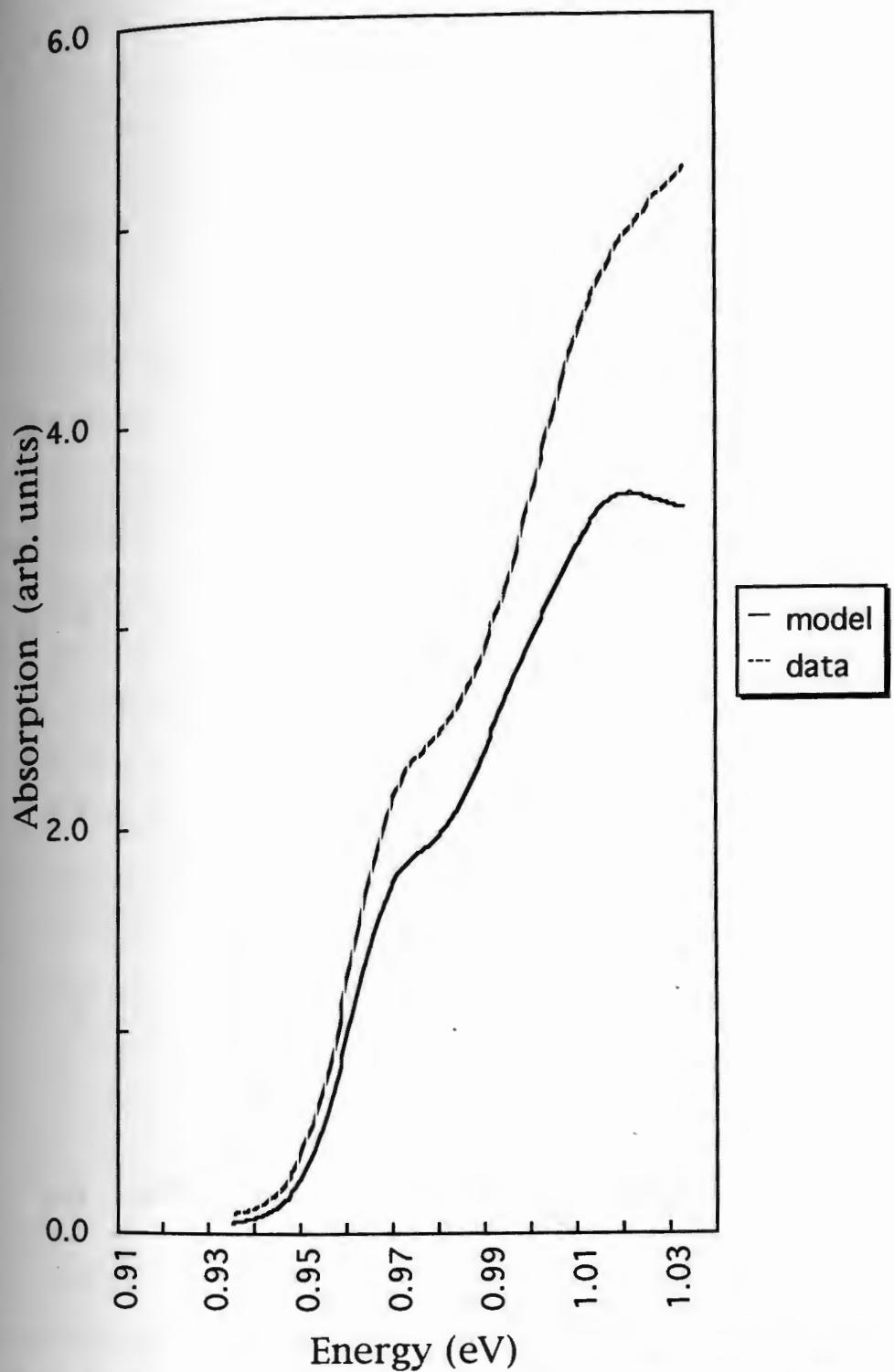

Figure 4.7. Model comparison with Zucker data. 15 Volts applied. 40/60 conduction/valence band split.

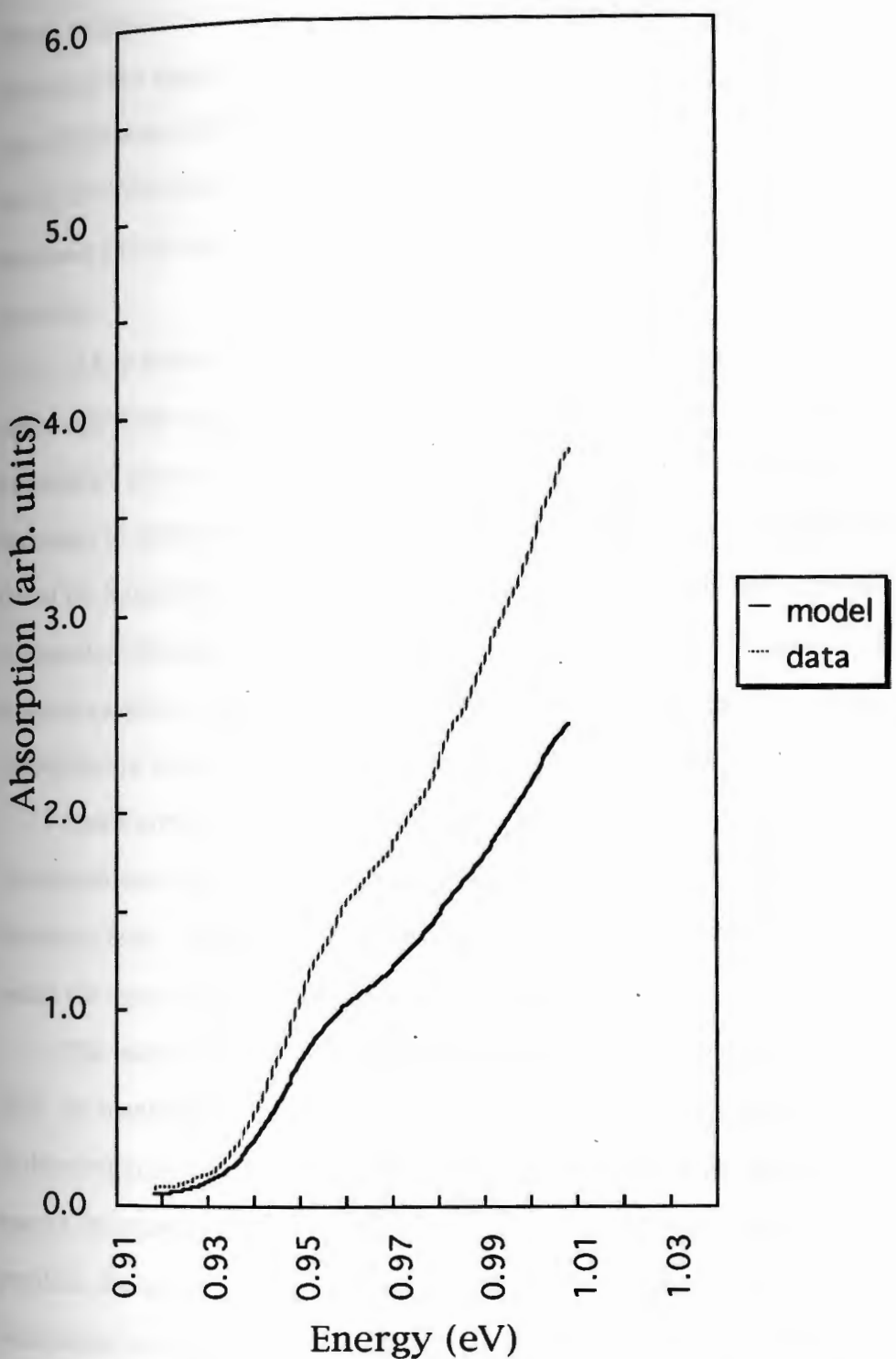

Figure 4.8. Model comparison with Zucker data. 20 Volts applied. 40/60 conduction/valence band split.

When Zucker et al.'s value of intrinsic layer thickness was used to determine the applied field from the applied voltage, the calculated shifts with field did not match. For d_i=1.16 μm, 5 volt steps correspond to 43 kV/cm field steps To fit the shifts it was necessary to use 51.5 kV/cm field steps, implying an effective d_i of 0.97 μm. The intrinsic layer thickness can be hard to estimate and the Zucker samples may not have been fully depleted.

A key feature of the Zucker data is that the linewidth remains approximately unchanged with applied field. In addition, the linewidth is greater than that of Sugawara's devices,[18,33] even when thermal broadening is accounted for. It was necessary to increase some of the inhomogeneous broadening components relative to that found for Sugawara's data and to find a combination yielding constant linewidth. Well composition broadening is the only linewidth component which decreases with field and hence is capable of offsetting tunneling and well width broadening which increase. The fitting factors which best fit the data are given in Table 4.1.

Strain applied in the plane of the layers through lattice mismatch, either intentional or unintentional, has as one of its effects the shifting of the light hole exciton relative to the heavy hole. In figure 4.5 to 4.9 a strain shift of +10 meV was incorporated to better match the separation of light and heavy hole in the data.

The major problem with the fit is that the model spectrum falls too much with field. As mentioned previously, references (16) and (23) did not include the dependence of the exciton oscillator strength upon λ^{-2}. A consequence of including this is that the spectra drop too far with field. Two factors were investigated as possible sources of this problem, the approximation involved in ignoring the z-direction coulomb interaction, and uncertainty in the splitting ratio of the band gap difference between the conduction and valence bands.

Perhaps the greatest weakness of the present theoretical approach is that it neglects the coulomb interaction for the exciton in the z direction. The coulomb interaction in the z

direction provides additional confinement of the electron and hole in that direction. This increases the overlap integral and hence increases the binding energy. With higher binding energy the exciton does not spread as much in the x/y plane, reducing λ. Both the increased overlap integral and the reduced λ lead to less of a drop of the spectrum with applied field.

Table 4.1.- -Linewidth Components of Zucker Data

Component	fit factor	value	Heavy hole exciton contribution, FWHM (meV)	
			0 volt	20 volt
Comp., random,well	clus	6	16	10.0
Comp., random, bar.	clus	6	0	0
Comp., macro., well	mac $\propto \sigma_{comp}$	1.7	4.0	3.4
Comp., macro., bar.	mac $\propto \sigma_{comp}$	1.7	0	0
Well width	isl = σ_{island}	2.4 mono.	7.2	15.4
Thermal	therm = σ_T	9.5 meV	9.5	9.5
Total gaussian			20.4	21
Tunneling	N.A.		.16	5.4

This simplification was justified in the past in that it gave fairly accurate results. This problem would have been less of a problem for the GaAs/AlGaAs system for which most of the theoretical work was done, because the well depth for electrons is significantly greater than that in InGaAsP. It may be that other simplifications, such as

ignoring the λ^{-2} dependence, masked the deficiencies in predicting the absorption magnitude. It is also noted that the magnitude is the characteristic most sensitive to such an error. A 20% error in binding energy is of minimal impact to the exciton shifts but gives a substantial change in magnitude through the λ^{-2} dependence.

Theoretical approaches which include the z direction interaction were investigated. One such by Wu et al.[53] uses a variational form in the z as well as the x/y directions. Two variational parameters are associated with the electron and hole z direction wavefunctions and one variational parameter is associated with the in-plane exciton wavefunction. A variational minimization is done, varying the multiple variational parameters to determine the lowest exciton binding energy. This method, however, is expensive in calculations and only made possible by the simplistic variational form used for the wavefunction. In solving for the z direction single particle wavefunctions, another researcher used a Monte Carlo technique instead of the RTM.[14] Like the RTM and unlike variational techniques, this method is capable of finding a more accurate and complex form of the wavefunction. It would perhaps be possible to use a model combining a z direction Monte Carlo technique with an in-plane variational technique, doing a simultaneous minimization of the binding energy. While likely to give more accurate wavefunction results than that of Wu, it would be excessively computationally intensive.

The second possible explanation is the uncertainty in the splitting ratio. While a 40% to 60% conduction band to valence band split has been used so far, various researchers have found a broad range of splitting ratios. This ratio was treated as an additional fitting factor in the method already described. Figures 4.9 through 4.13 show the fit using the factors in Table 4.2. It can be seen from the figures that the modified splitting ratio yields model results which more closely match the drop in absorption with increased field.

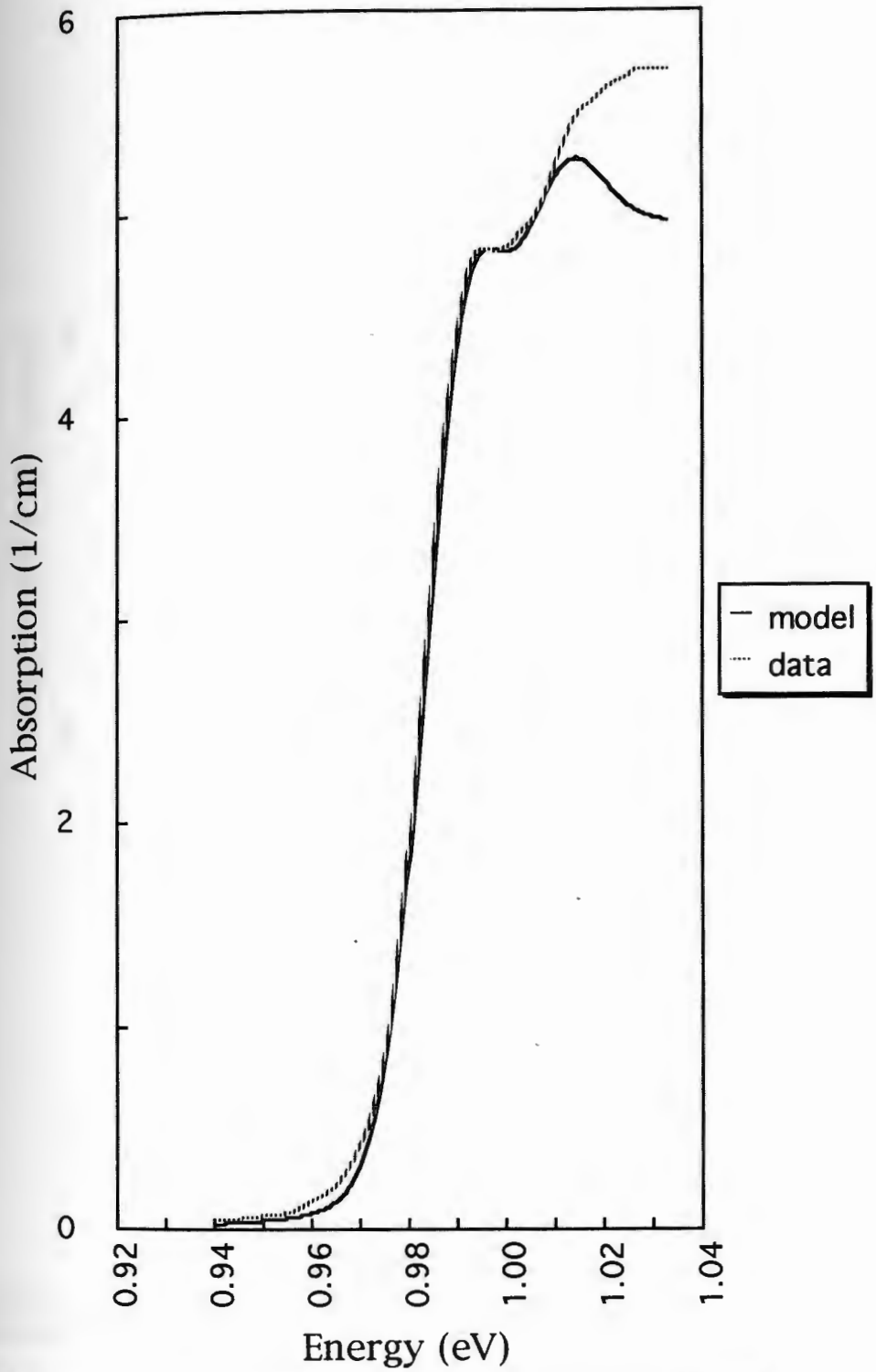

Figure 4.9. Model comparison with Zucker data. 0 Volts applied. 56/44 conduction/valence band split.

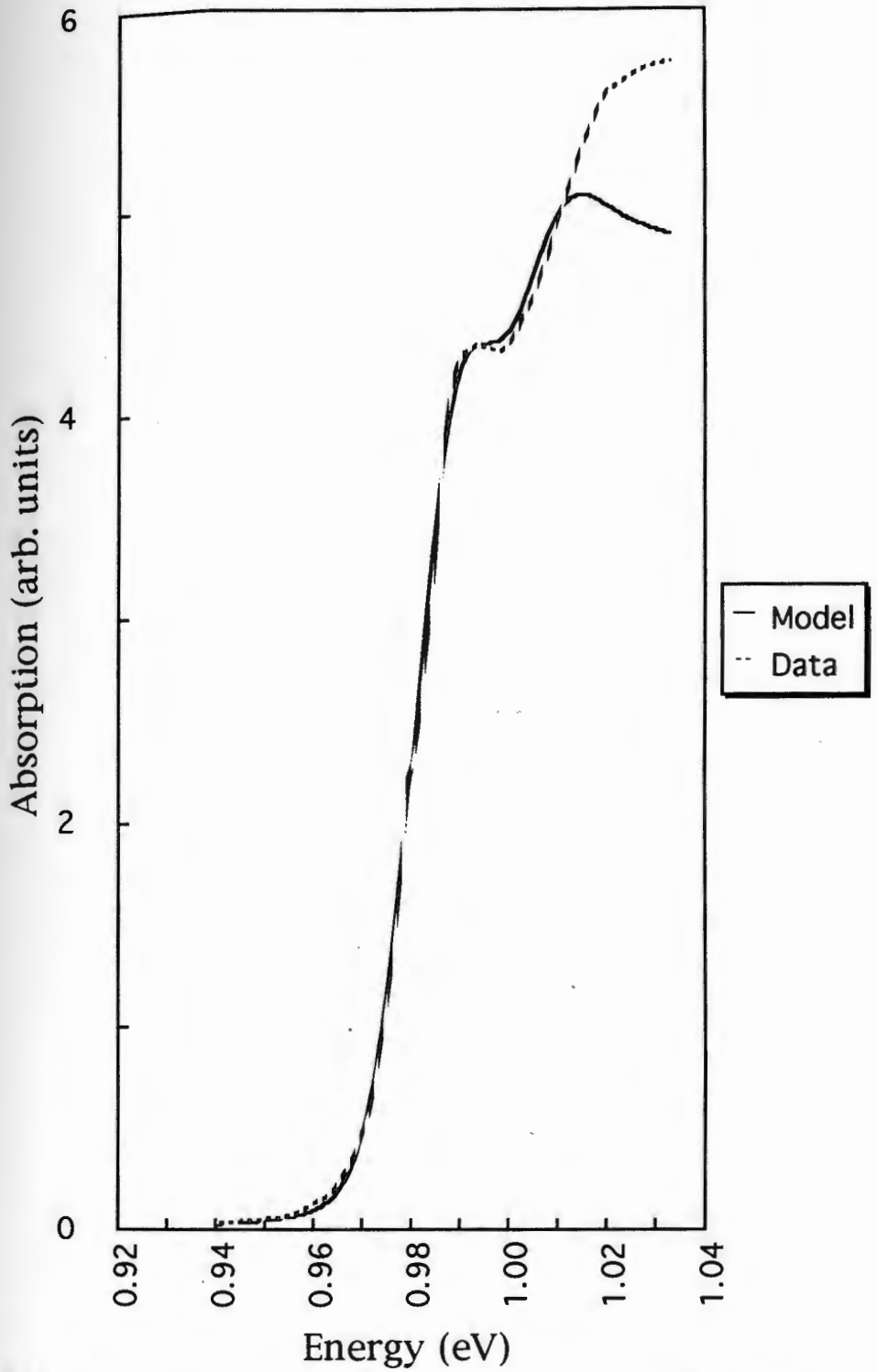

Figure 4.10. Model comparison with Zucker data. 5 Volts applied. 56/44 conduction/valence band split.

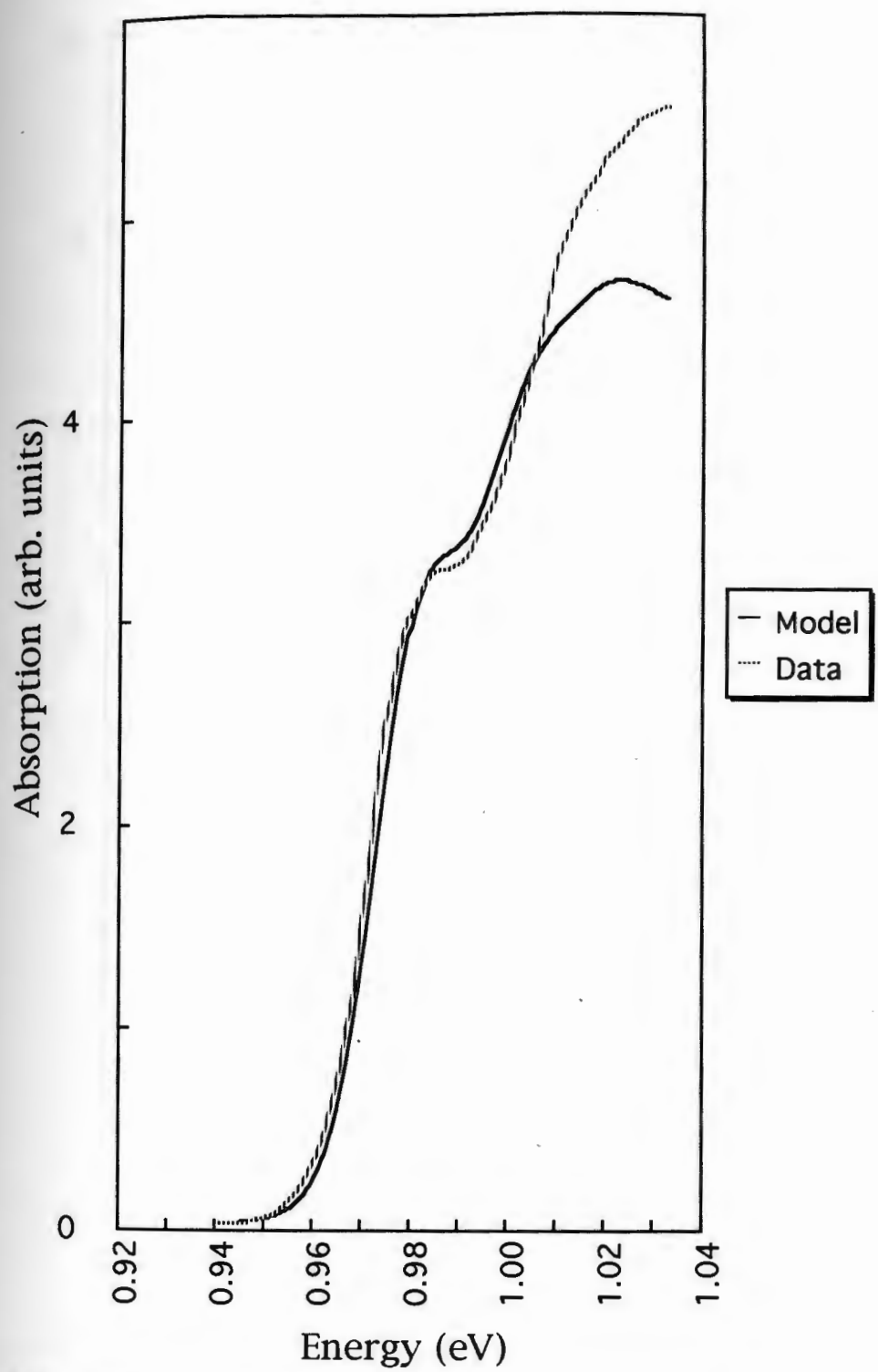

Figure 4.11. Model comparison with Zucker data. 10 Volts applied. 56/44 conduction/valence band split.

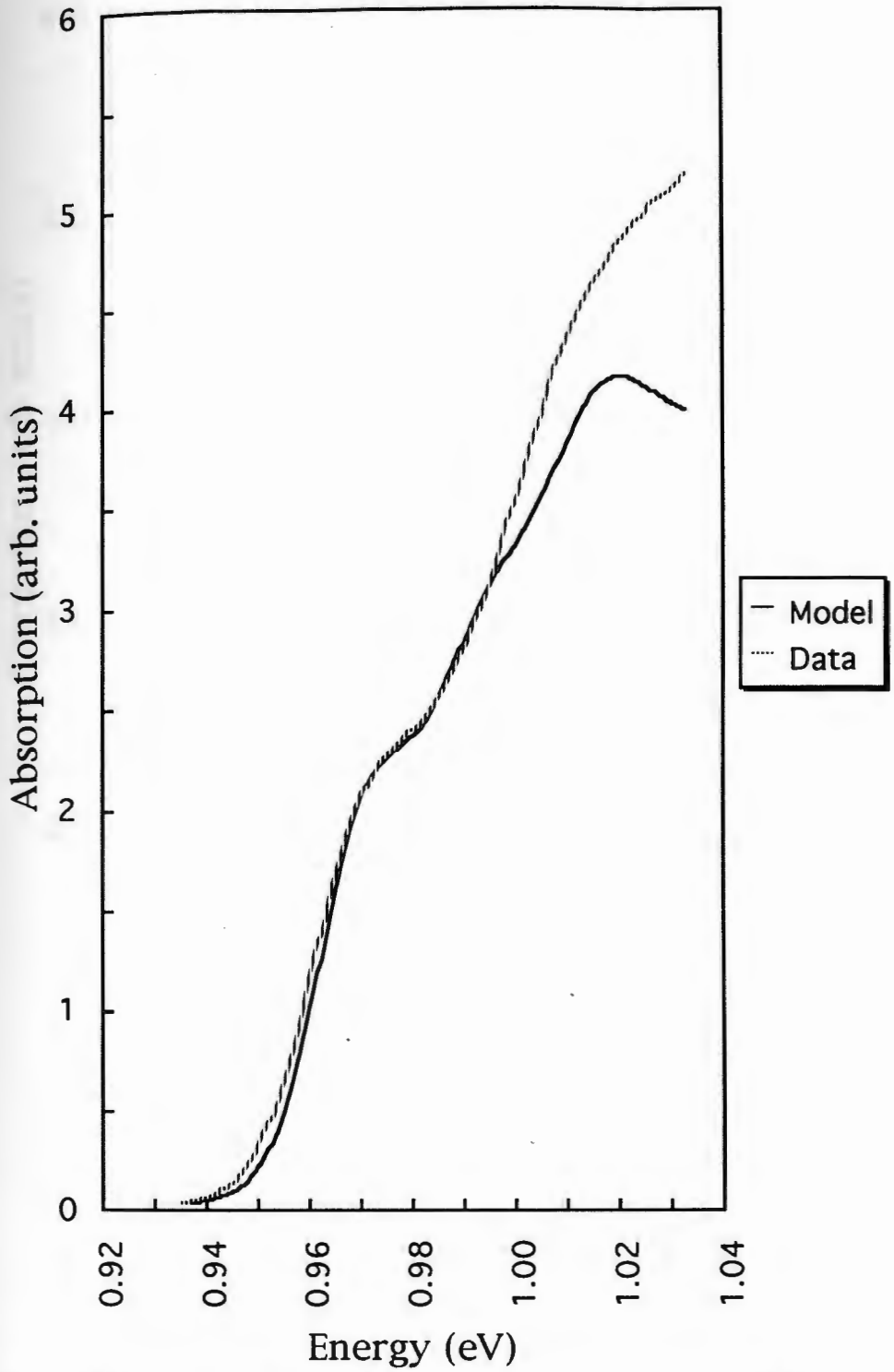

Figure 4.12. Model comparison with Zucker data. 15 Volts applied. 56/44 conduction/valence band split.

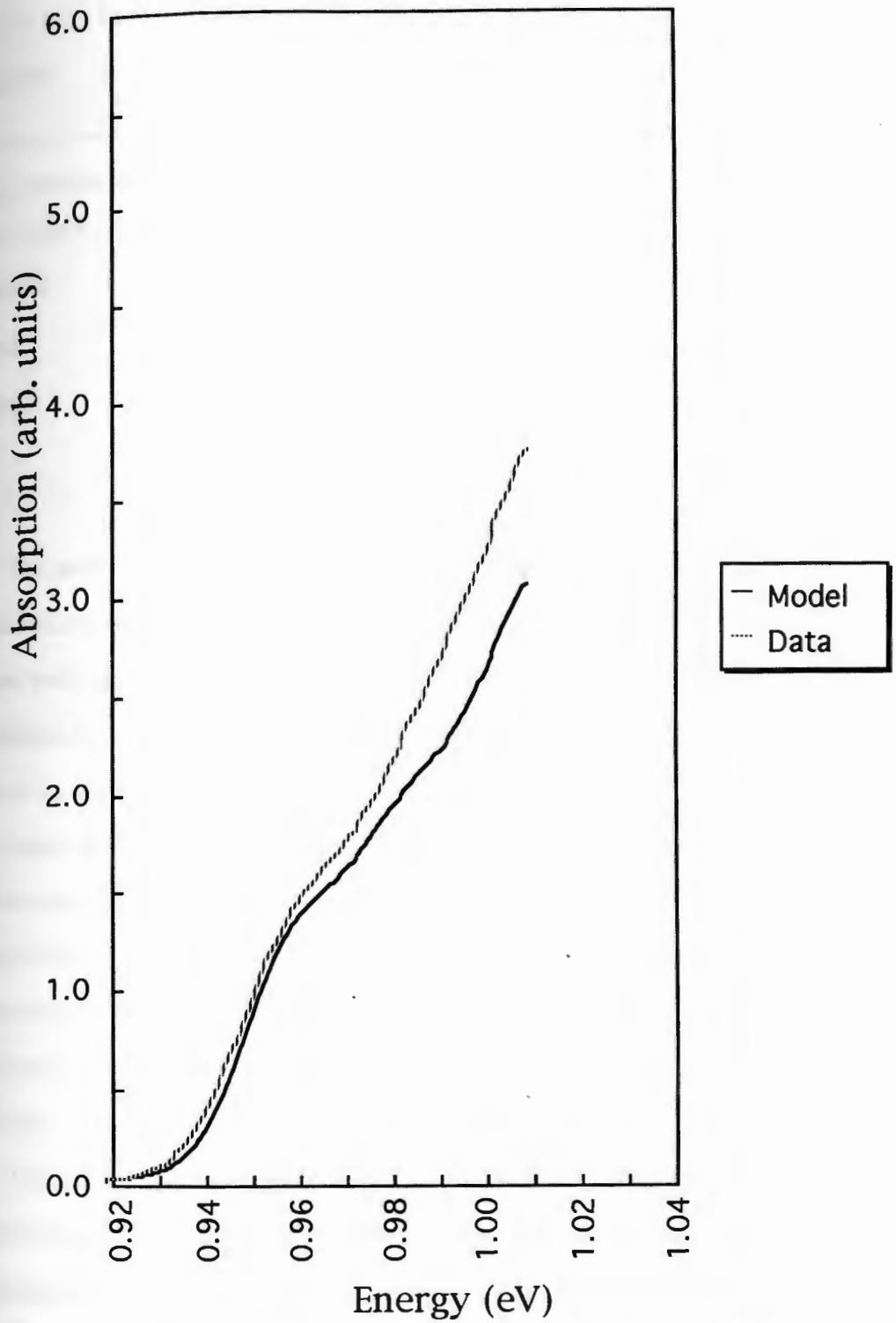

Figure 4.13. Model comparison with Zucker data. 20 Volts applied. 56/44 conduction/valence band split.

Table 4.2.--Fit Factors for Figures 4.9 to 4.13

Component	fit factor	value
Comp., random,well	clus	5
Comp., macro., well	mac $\propto \sigma_{comp}$	1.7
Well width	isl = σ_{island}	2.4 mono.
Thermal	therm = σ_T	9.5 meV
Split ratio	56/44 conduction/valence	

Siemens Data

The second example is unpublished experimental data provided courtesy of Siemens Research Laboratories. This sample included 15 quantum wells with 75 angstom wells and 100 angstrom barriers. Well composition is y=.846 and barrier composition is y=.405. Absorption spectra were obtained using a broadband optical source and a grating spectrometer.

Initial attempts to fit the model to the data encountered the same problem with the spectrum absorption dropping too much with applied field. Figures 4.14 to 4.16 show a fit using a 50%/50% conduction band/ valence band splitting ratio The three plots show applied voltages of 0, 2, and 4 volts. The built in voltage is estimated at 2 volts. The model best fits the experimental exciton shifts when fields of 40, 80, and 120 kV/cm were used.

The linewidth is greater than that of Sugawara et al.'s devices,[18] even when thermal broadening is accounted for. It was necessary to increase some of the inhomogeneous broadening components relative to that found for Sugawara et al.'s data. The fitting factors which best fit the data across the range of applied fields are given in Table 4.3. The Siemens devices seem to be dominated by well width broadening, either

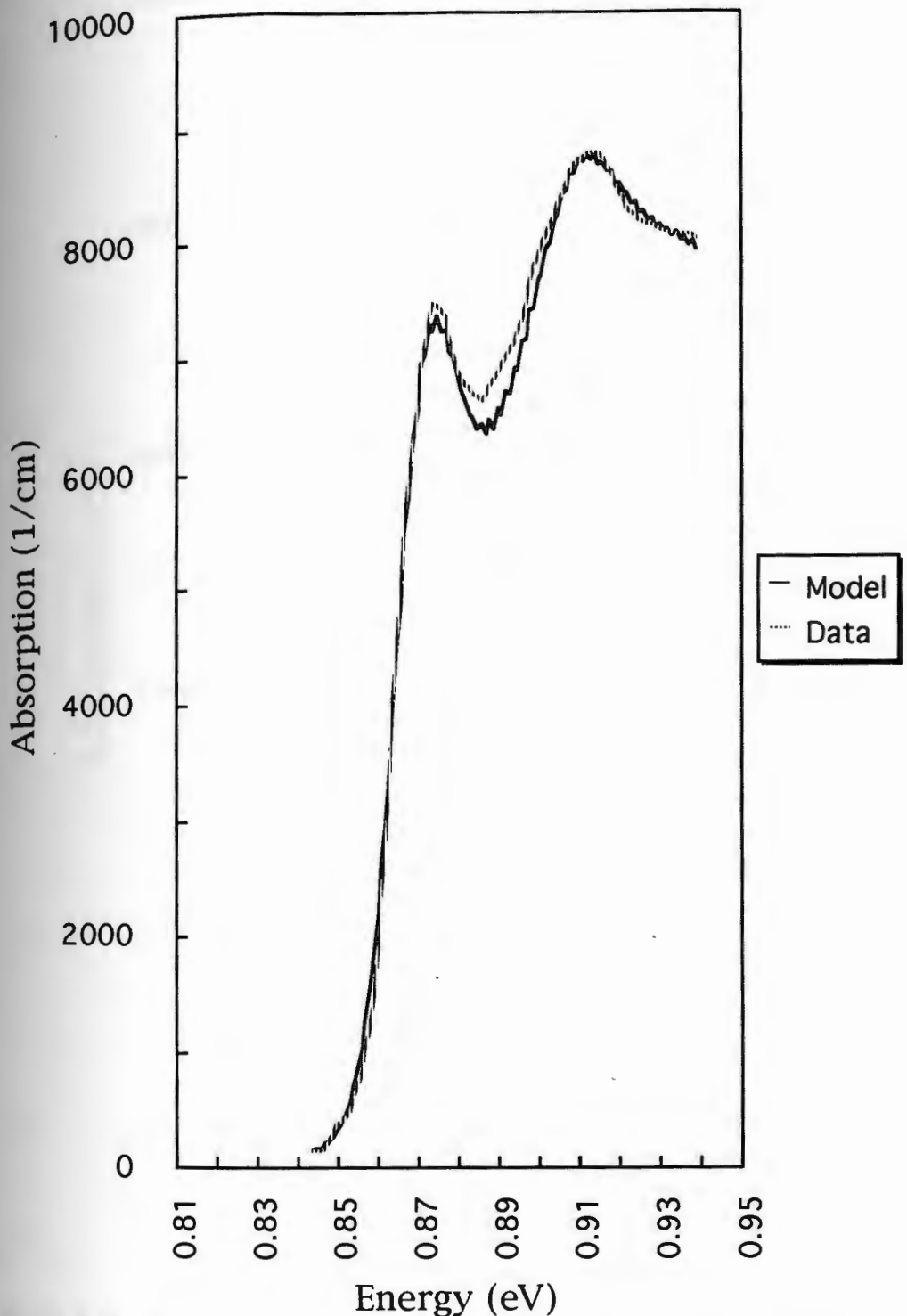

Figure 4.14. Model comparison with Siemens data. 0 Volts applied. 50/50 conduction/valence band split.

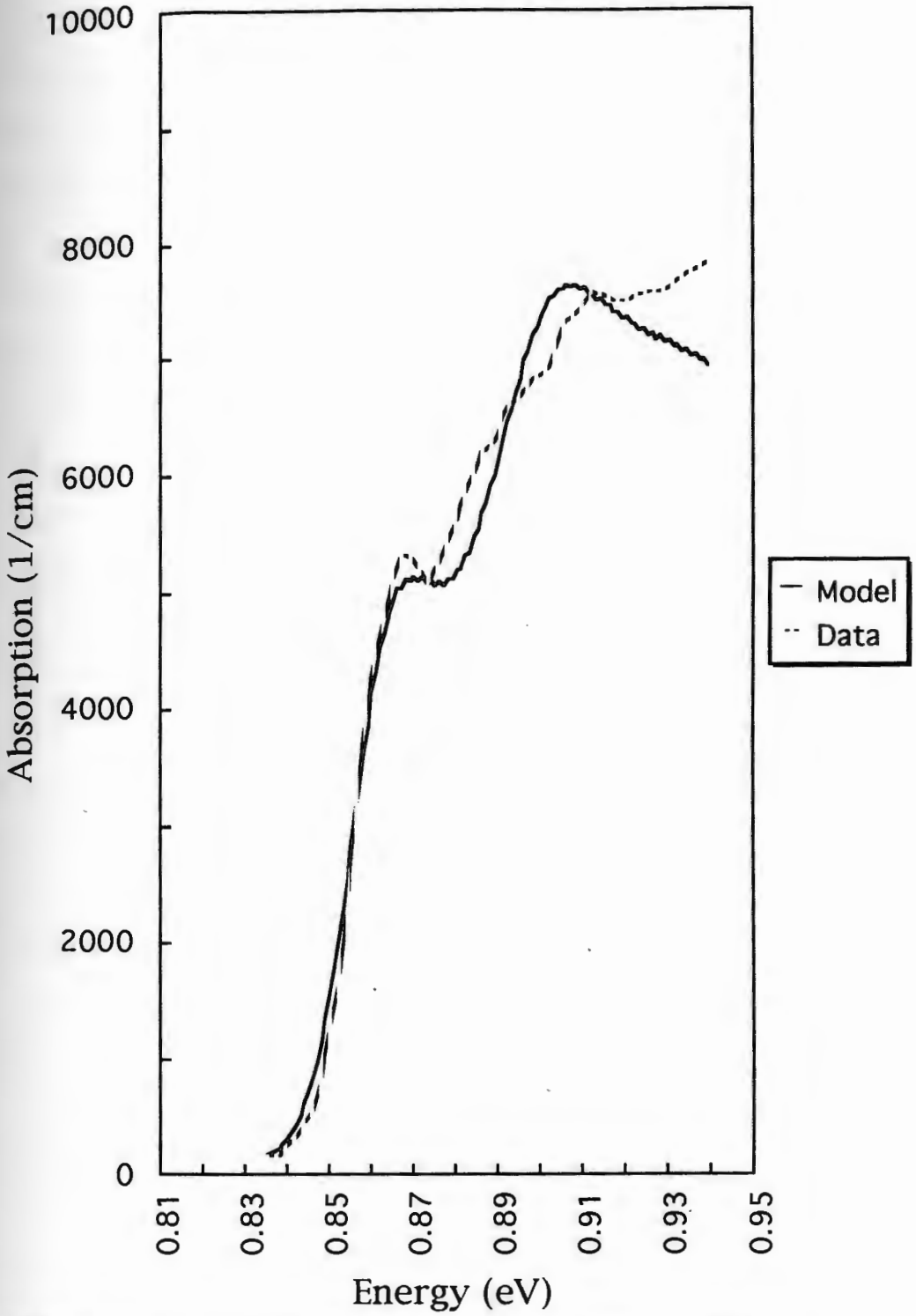

Figure 4.15. Model comparison with Siemens data. 2 Volts applied. 50/50 conduction/valence band split.

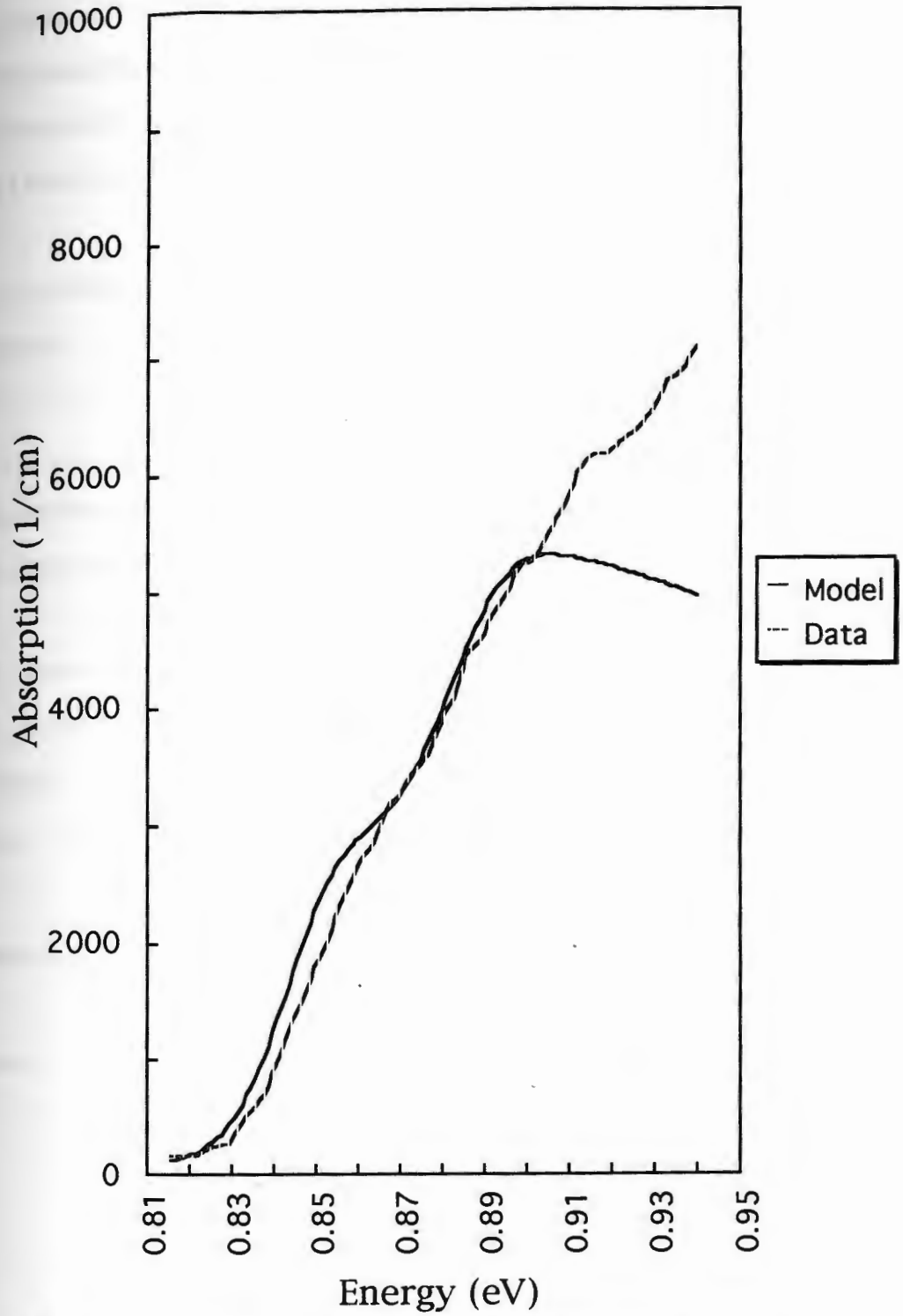

Figure 4.16. Model comparison with Siemens data. 4 Volts applied. 50/50 conduction/valence band split.

from rough interfaces or from variations in well thickness from well to well. It is also noted that tunneling is significantly higher than for the Zucker et al.[19] devices. This is a direct consequence of the smaller composition difference between the wells and barriers, giving a shallower well.

Table 4.3.--Linewidth Components of Siemens Data

Component	fit factor	value	Heavy Hole Exciton Contrib., FWHM (meV)	
			0 volt	20 volt
Comp., random,well	clus	1	1.8	1.2
Comp., random, bar.	clus	1	.13/.16	.14/.26
Comp., macro., well	mac $\propto \sigma_{comp}$	1	2.3	2.0
Comp., macro., bar.	mac $\propto \sigma_{comp}$	1	.08/.16	.07/.48
Well width	isl = σ_{island}	5.5 mono.	12.8	20.8
Thermal	therm = σ_T	9.5 meV	9.5	9.5
Total gaussian			16.2	23
Tunneling	N.A.		.48	8.8

CHAPTER 5

MODULATOR DEVICE MODELING

Design Approach

The goal of all the material modeling thus far presented is to support the design optimization of optical modulator devices. It is necessary to take the absorption spectra vs field data of the material model and derive from these the modulator performance. It is first necessary to identify those performance parameters of interest and the design parameters which are available to define the design. Table 5.1 gives a possible list of each.

Table 5.1.--Design and Performance Parameters

Design Parameters	Performance Parameters
well width	3 dB bandwidth
barrier width	insertion loss
well composition	contrast ratio
barrier composition	chirp
modulator length	drive voltage
number of wells	
bias voltage	
drive voltage	
stress-strain in layers*	

* Stress-strain was not considered in this study due to a lack of experimental data.

Given the large number of design and performance parameters, careful thought must be given to a basic optimization strategy. The few published works on optimization of MQW modulator design have usually relied on establishing figures of merit to combine several desired performance parameters into a single parameter. The most common are the device's bandwidth/drive voltage ratio or the ratio of the contrast to the drive voltage/length product. Figures of merit are inadequate when they leave out important performance characteristics or inappropriately weight the importance of the parameters. With efficiency figures of merit it is also possible to drive the design to high efficiency and no performance, i.e. the design that gives the best bandwidth to drive voltage ratio may not give the bandwidth one desires. Given these problems, a figure of merit was not used and the performance parameters were simply presented in tabular form. Performance cut-offs for the different parameters were established, and designs not meeting one or more of the requirements were not presented.

Several assumptions were made relative to the design process. Rather than designing with a variable drive voltage, it was assumed that a certain maximum drive voltage is available and the device must be designed for maximum performance with that driver. This is more commonly the situation in practice as drive power is severely limited at microwave frequencies. This eliminated drive voltage as either a design parameter or a performance parameter. A drive voltage of 2 volts and a built in voltage of 1.15 volts was used. In a few cases in Chapter 6, this fixed voltage was changed and the model recalculated to determine the effect of a lower drive voltage on the design process.

It was also assumed that fairly high insertion loss could be tolerated. This is certainly not true in all cases, but is true in many cases of current interest. The recent development and widespread implementation of fiber optic amplifiers at 1.55 μm or semiconductor optical amplifiers integrated with the modulators can change the constraints on system design. High modulator loss at a transmitter can be compensated by a power amplifier before transmission. The modulator's loss will not greatly impact

the system as long as the optical power level input into the amplifier is higher than the lowest optical power level reached in the transmission amplifier chain. Thus, unlike past studies, this study has gone further in considering trading optical loss for other performance features. Finally, chirp was considered to be a major performance parameter. External modulation has mostly been considered over direct laser modulation due to the perception that chirp performance is improved with the former. External modulators, however, can exhibit appreciable chirp and the design must address minimizing it to meet system goals for dispersion in long distance communications.

Several parameters were fixed in the interest of minimizing the number of variable design parameters. A single bias voltage was used. Upon manufacture, a modulator's operation may be shifted relative to the design and bias voltage may be useful to tune the modulator's performance to the correct wavelength. It is not apparent, however, that it serves any other purpose. By comparing the Zucker and Siemens tunneling linewidths it is apparent that the barrier composition should be as close to InP as possible. The modulator efficiency is increased if the inactive barrier material is reduced by thinner barrier layers. Thinner barrier layers can only be used if the tunneling is kept low. Siemens personnel indicated that they prefer a InGaAsP composition. There is always some GaAs diffusion and they have found that a small GaAs concentration is more accurately controlled. While it may thus be adviseable to maintain a small y in the barrier, it should be minimized. A fixed y of 0.1 was chosen.

Device Equations

This study addresses the performance of waveguide type modulators. The effective refractive index of the waveguide mode is given by:

$$n_{eff}^2 = \frac{n_w^2 L_w + n_b^2 L_b}{L_w + L_b} \tag{5.1}$$

where n_w and n_b are the refractive index of the well and barrier material respectively, and L_w and L_b are the well and barrier thicknesses. The refractive index of the barrier layers

is given by the single-effective-oscillator (SEO) method with interpolation between the four binaries. The formulas of reference (54) are used:

$$n^2 = 1 + \frac{E_d}{E_0} + \frac{E_d}{E_0^3}E^2 + \frac{\eta}{\pi}E^4 \ln\left(\frac{2E_0^2 - E_g^2 - E^2}{E_g^2 - E^2}\right) \tag{5.2}$$

where:

$$E = h\nu$$

$$\eta = \frac{\pi E_d}{2E_0^3\left(E_0^2 - E_g^2\right)}$$

$$E_0 = 0.595x^2(1-y) + 1.626xy - 1.891y + 0.524x + 3.391$$

$$E_d = (12.36x - 12.71)y + 7.54x + 28.91$$

$$E_g = 1.35 + 0.668x - 1.17y + 0.758x^2 + 0.18y^2 - 0.069xy - 0.322x^2y + 0.03xy^2$$

This method has been shown to fit well with experimental measurements of InGaAsP refractive index at wavelengths away from the bandgap.[55] This equation was used for the refractive index of the barrier layers and the waveguide cladding layers surrounding the multi-quantum well material.

The SEO theory exhibits a singularity at the bandgap and is of no use in predicting refractive index in the region near the bandgap.

The refractive index at the bandgap is given by Nahory and Pollack[56] by interpolation between the measured index at the bandgap for the four binaries:

$$n = 3.4 + 0.256y - 0.095y^2 \tag{5.3}$$

For this work, the refractive index of the well layers was found by determining the detuning from the bandgap, and using linear interpolation between the refractive index at the bandgap given by equation 5.3 and the refractive index 20 meV away from the bandgap given by equation 5.2.

Based on Agrawal and Dutta's[57] formula for bulk waveguides, the following emperical formula gives the fill factor for MQWs:

$$\Gamma = \frac{\left(k_0 d_i\right)^2\left(n_{eff}^2 - n_1^2\right)}{1.5 + \left(k_0 d_i\right)^2\left(n_{eff}^2 - n_1^2\right)}\left(\frac{L_w}{L_w + L_b}\right) \tag{5.4}$$

where $k_0 = (2\pi/\lambda)$, (from this point on the symbol λ is used for the wavelength). The p and n regions of the pin junction form the cladding region of the waveguide and have refractive index n_1. These regions are InP with an index given by equation 5.2. The thickness of the intrinsic quantum well region is d_i, given by:

$$d_i = (L_w + L_b)z + L_b \tag{5.5}$$

The number of quantum wells is z.

It can be shown that the device contrast ratio is given by:

$$CR = 10\log\left\{\exp\left[\left(\Delta\alpha(F_{off},\lambda) - \Delta\alpha(F_{bi},\lambda)\right)\Gamma L\right]\right\} \tag{5.6}$$

where L is the device length. The absorption change at wavelength λ with maximum applied field F_{off} is:

$$\Delta\alpha(F_{off},\lambda) = \alpha(F_{off},\lambda) - \alpha(F=0,\lambda) \tag{5.7}$$

Likewise $\Delta\alpha(F_{bi},\lambda)$ is the absorption change at λ with built in field F_{bi}. F_{bi} corresponds to the high transmission state of the modulator and includes both the device's built in voltage and any voltage applied in the "on" state to tune the modulator's performance to the correct wavelength. F_{off} corresponds to the off state. It is noted that the "off" refers to the light being "off", not the applied field. The applied field is given by:

$$F = V/d_i + F_{bi} \tag{5.8}$$

The insertion loss is given by:

$$IL = 10\log\left\{\exp\left[-\Gamma L\left(\Delta\alpha(F_{bi},\lambda) + \alpha(F=0,\lambda)\right)\right]\right\} \tag{5.9}$$

To determine the bandwidth it is first required to calculate the capacitance of the device.

$$C = \frac{\varepsilon_0 n_{eff}^2 LW}{d_i} + C_{para} \tag{5.10}$$

A waveguide width, W, of 3 μm was used. A parasitic capacitance, C_{para}, of 0.030 picofarads was added for contact pads and leads. The -3 dB bandwidth is given by:

$$BW = \frac{1}{2\pi R_0 C} \tag{5.11}$$

where the terminating resistance, R_o, is 50 ohms.

Index Change and Chirp

Associated with the modulator absorption change is a change in refractive index. The change in refractive index can be found using a Kramers-Kronig integral[58]:

$$\Delta n(E,F) = \frac{c\hbar}{\pi}\int_0^\infty \frac{\Delta\alpha(F,E')}{E'^2 - E^2}dE' \tag{5.12}$$

It is necessary to calculate around a singularity at E'=E. The integral is devided as:

$$\int_0^\infty \frac{\Delta\alpha(F,E')}{E'^2 - E^2}dE' = \int_0^{E-h} \frac{\Delta\alpha(F,E')}{E'^2 - E^2}dE' + \int_{E-h}^{E+h} \frac{\Delta\alpha(F,E')}{E'^2 - E^2}dE' + \int_{E+h}^\infty \frac{\Delta\alpha(F,E')}{E'^2 - E^2}dE' \tag{5.13}$$

The first and third integrals were calculated by the trapezoidal rule. The second integral is estimated by using Taylor's theorem to expand $\Delta\alpha$ for small h. The second integral can then be calculated term by term. Retaining two terms:

$$\int_{E-h}^{E+h} \frac{\Delta\alpha(F,E')}{E'^2 - E^2}dE' \approx \ln\left(\frac{2E-h}{2E+h}\right)\left\{\frac{\Delta\alpha}{2E} - \left(\frac{d\Delta\alpha}{dE'}\right)_{E'=E} + \ldots\right\} \tag{5.14}$$

In numerically calculating the index change it is not possible to evaluate the integral from 0 to infinite energy. The integral is started at an energy well below the exciton where the absorption change contribution is negligible. At the high energy end, the absorption spectrum model does not adequately represent the true spectrum because only the 1e:1hh, 1e:1lh, and 1e:2hh excitons are included. Numerous additional transitions which have not been modeled also add to the absorption spectrum. This deficiency of the model does not have an appreciable effect upon the shape of the index change spectrum in the spectral region of interest near the absorption edge. This is because the primary contribution to the index change at a particular energy E is the absorption nearest to E. The deficiency of the absorption spectra can have the effect of increasing or decreasing the entire index change spectrum. As field is applied the absorption curves shift to lower energy and the contributions of the light and heavy hole drop. The contribution of the second heavy hole exciton initially rises and eventually drops also. The dropping of the

absorption spectra decreases the total absorption contribution to the Kramers-Kronig integral and the entire index change spectrum is lowered. The most noticeable effect is that at low energy, far from the exciton, the index change is negative, instead of going to zero as expected. In reality, when applied field causes the hh and lh exciton oscillator strengths to decrease, the oscillator strengths of other transitions should increase to maintain the same oscillator strength sum.[8] This effect was approximated by integrating the calculated absorption change across the full range of the integral for each field. The absorption change spectra was then increased in a region well above the excitons as necessary to maintain the total absorption change constant. This eliminated the problem at low energy without affecting the shape of the index change spectrum near the absorption edge.

The chirp performance of a modulator is often defined in terms of the chirp parameter α_H, called the Henry factor:

$$\alpha_H = \frac{dn}{dk} \tag{5.15}$$

where n and k are the real and imaginary parts of the electroabsorptive material's index. The Henry factor should not be confused with the symbol used for absorption. Dorgeuille and Devaux[59] have recently published a study of the non-return to zero (NRZ) intensity modulation transmission performance versus the chirp parameter for MQW modulators. They discussed how the phase versus absorption curve in a MQW modulator is not linear, so that the chirp parameter varies according to how the device is biased and changes within each modulation swing. Figure 5.1 shows a typical phase versus absorption curve from Reference 59. The chirp parameter is the slope at any point of the curve. In the past, system designers have attempted to describe the chirp performance by a single chirp parameter. The most common form is the following:

$$\alpha_{H,\text{on,off}} = \frac{\Delta n(F_{bi}) - \Delta n(F_{off})}{\Delta k(F_{bi}) - \Delta k(F_{off})} \tag{5.16}$$

where:

$$\Delta k(F) = \frac{\Delta\alpha(F)}{2k_0} \tag{5.17}$$

Koyama et al.[60] and Gnauck et al.,[61] have calculated dispersion penalties and system transmission performance, given a single valued chirp parameter as defined in (5.16). All found that the optimum chirp parameter varies between zero and -1, depending on system jitter tolerances. These values give some amount of pulse compression in the fiber transmission. At the optimum value the bit-rate-squared length product was significantly increased compared with that for positive chirp parameters.

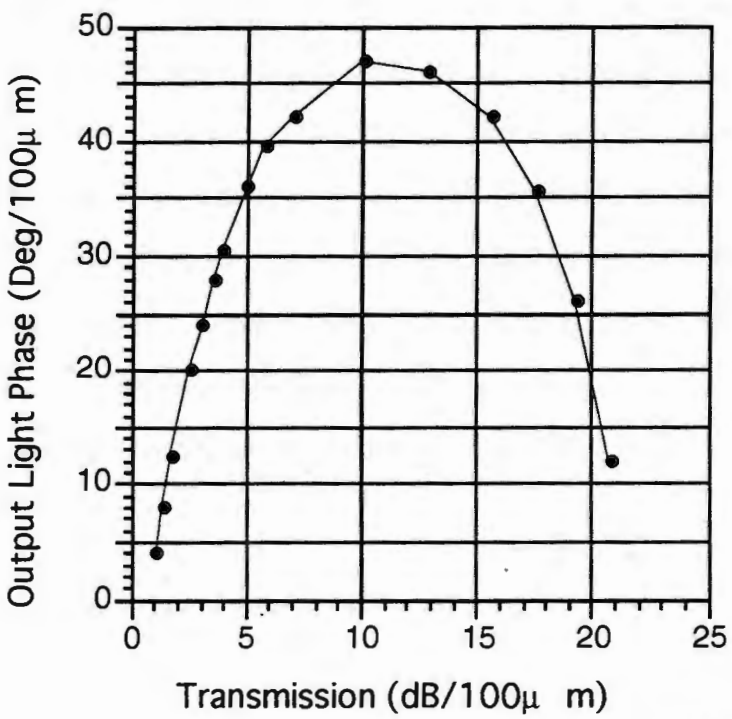

Figure 5.1. Typical phase of output light versus transmission for a 100 μm modulator.

Dorgeuille and Devaux[59] further investigated the performance with the more complicated bias dependent chirp parameter of the MQW modulator. They found that the transmission system performance could be estimated accurately with a single valued chirp parameter defined as:

$$\alpha_{H,3dB} = \frac{\Delta n(F_{bi}) - \Delta n(F_{3dB})}{\Delta k(F_{bi}) - \Delta k(F_{3dB})} \tag{5.18}$$

where F_{3dB} is the field at which the absorption is increased by 3dB. This makes intuitive sense in that dispersion has little impact when the bit is off and there is no light to disperse. Both $\alpha_{H,on-off}$ and $\alpha_{H,3dB}$ were calculated, but the design effort focused on $\alpha_{H,3dB}$. The phase shift was also calculated:

$$\phi = k_0 \Gamma L \left[\Delta n(F_{off}) - \Delta n(F_{bi}) \right] \tag{5.19}$$

The final design optimization program was comprised of two parts. The material model program calculated the absorption change and index change spectra for a series of values of well width, well composition, and barrier width. For each combination it ran nine fields: 0, 14, 28, 42, 56, 70, 84, 98, and 120 kV/cm. The modulator's design wavelength of operation was chosen to be 1550 nm. The second program ran a series of lengths and well numbers. As a result, F_{bi} and F_{off} varied from trial to trial. It was necessary to interpolate from $\Delta\alpha$ and Δn values from a minimal number of fields which still provided sufficient accuracy. In the first program the $\Delta\alpha$ and Δn values at 1550 nm were extracted for each field. Separate cubic splines were used to fit $\Delta\alpha$ vs. field and Δn vs. field and the spline parameters were stored for later use by the second program. Typical results are shown in Figures 5.2 to 5.4 for case 12513, an optimized low chirp design.

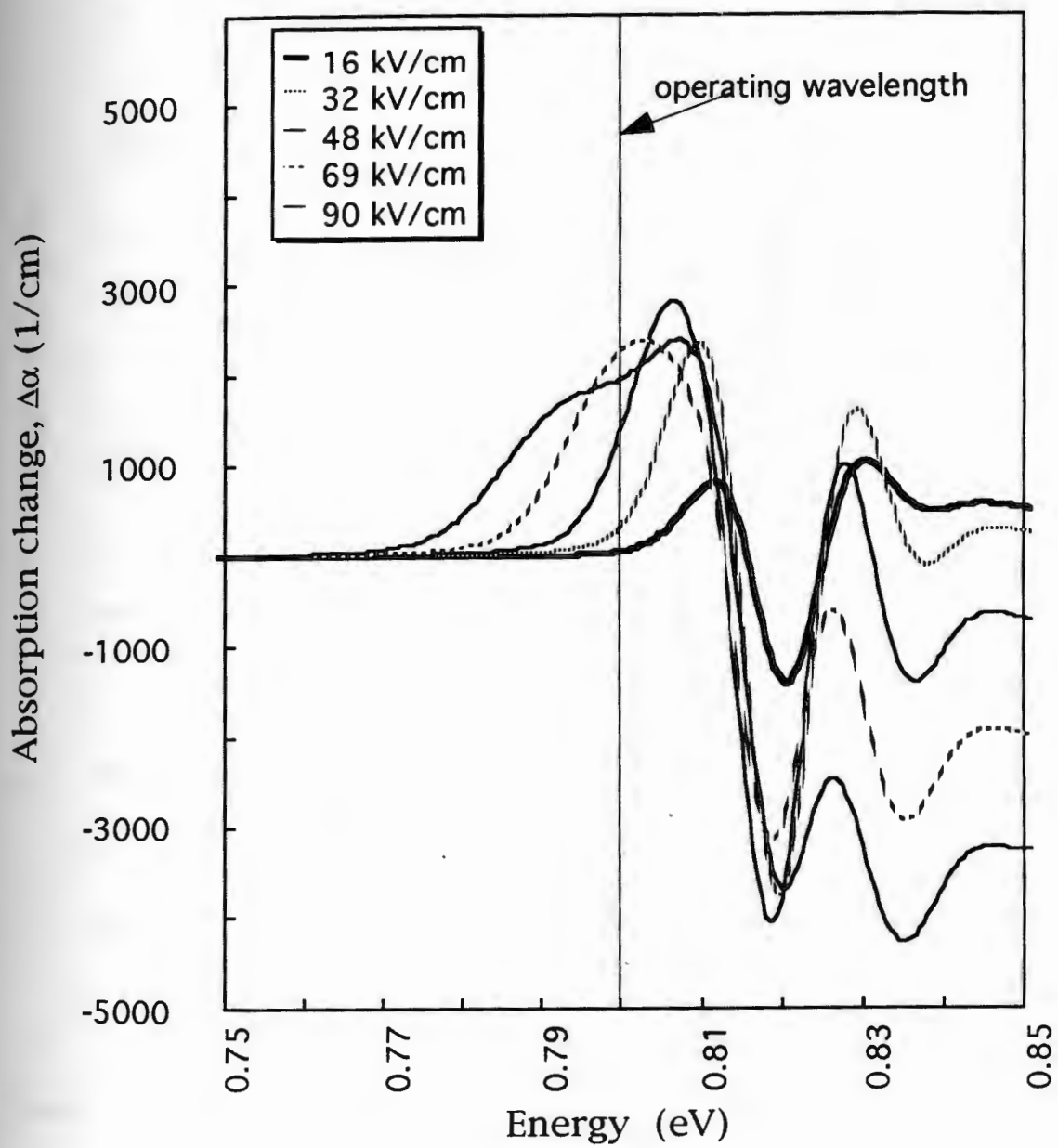

Figure 5.2. Absorption change spectrum. Case 12513.

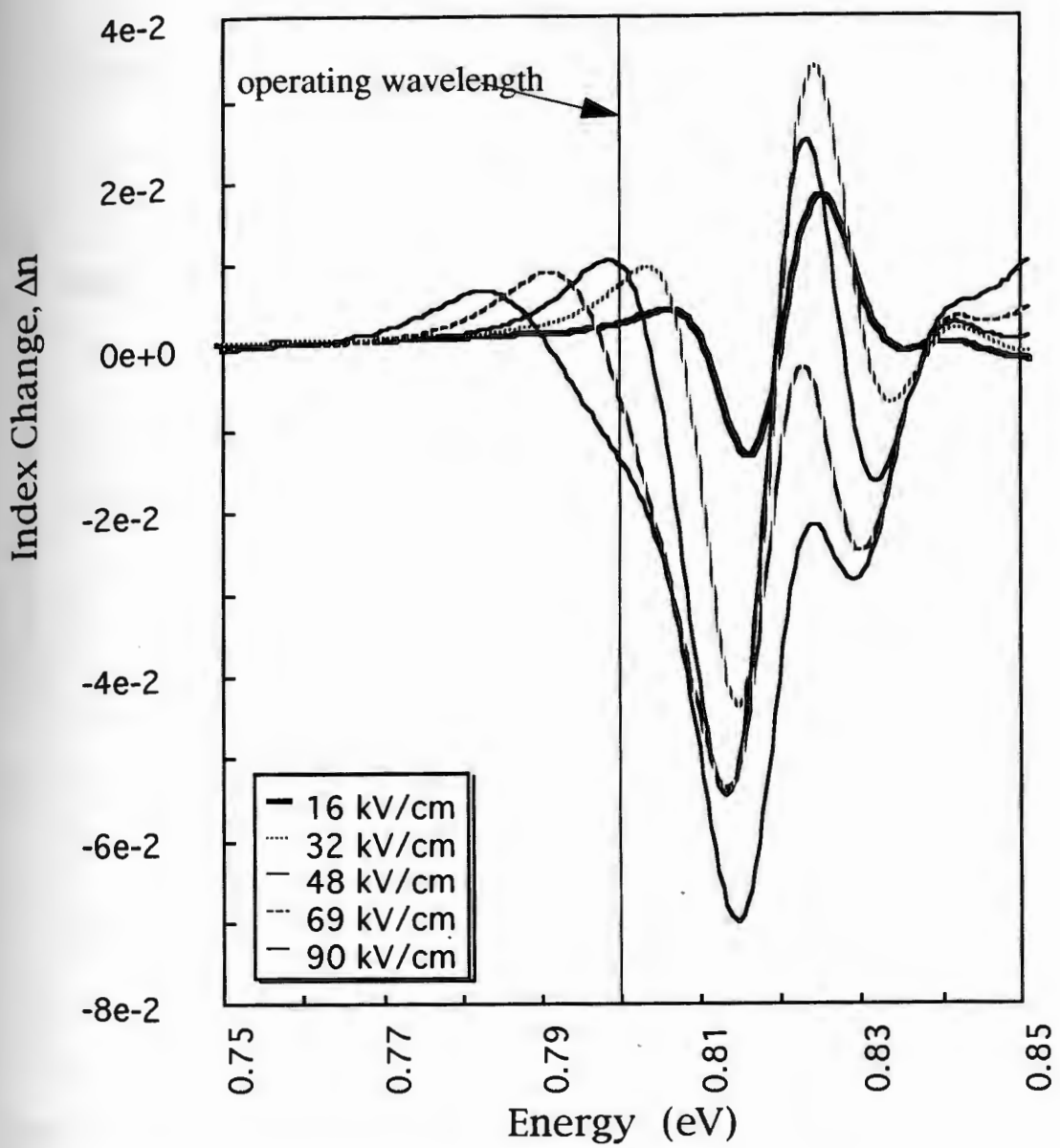

Figure 5.3. Index change spectrum. Case 12513.

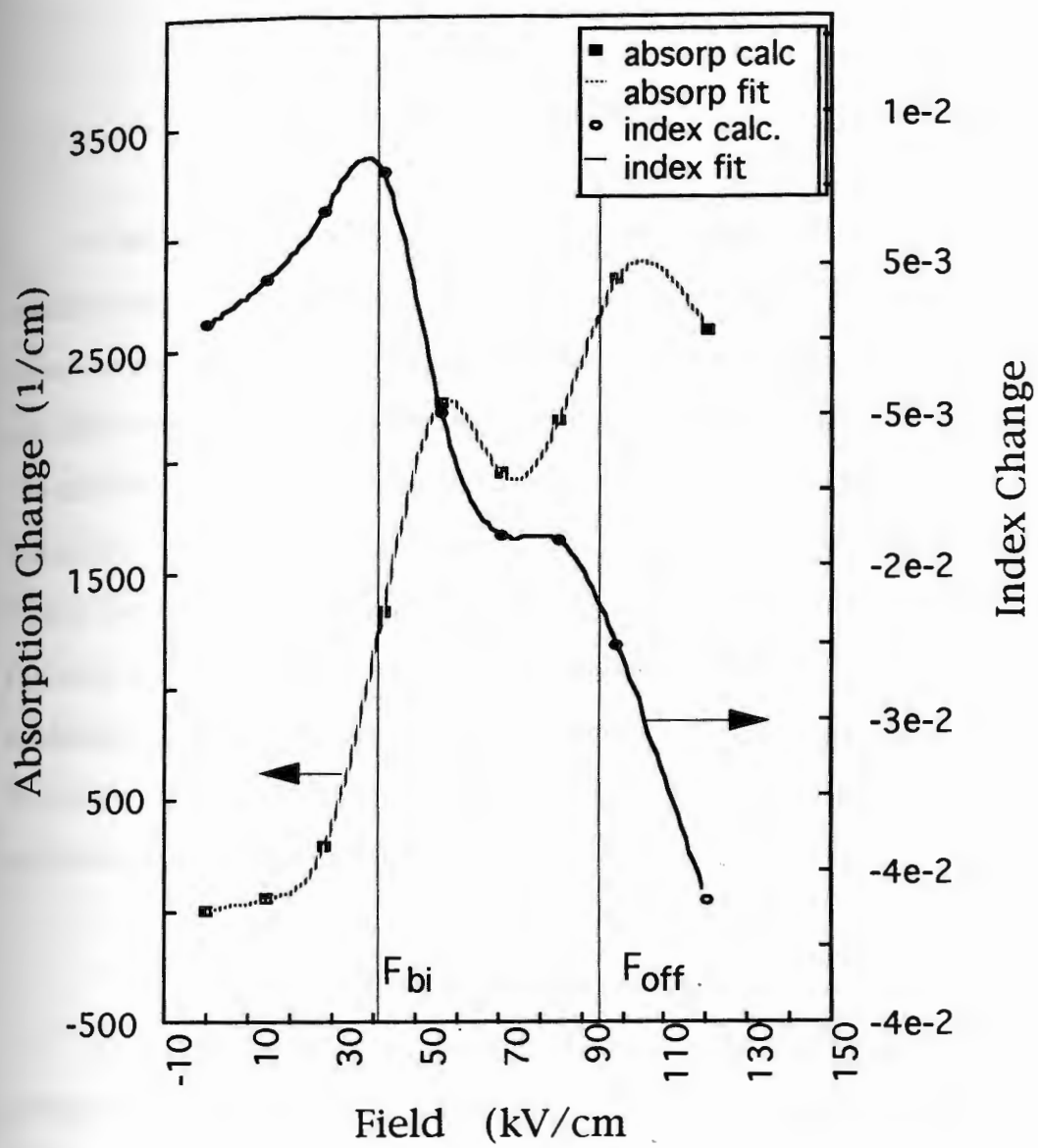

Figure 5.4. Absorption and index change at 1550 nm versus field with cubic spline fit. Case 12513.

CHAPTER 6

DESIGN RESULTS

In the following discussion, the various designs considered by the design optimization program are represented by a five digit design code. The first digit represents the choice of device length, with one through four representing 50, 100, 150, and 200 microns. The second digit represents the number of wells: 10, 15, 20 ,or 25. The third digit represents the well width: 12.5, 13.0, 13.5, 14.0, 14.5, or 15.0 nanometers. The fourth digit represents the barrier width: 4.0, 6.0, or 8.0 nanometers. Finally, the fifth digit represents well composition y_W: 0.89, 0.90, 0.91, 0.92, or 0.93. For quick reference these values are shown in Table 6.1. For each design, the bandwidth, contrast ratio, absorption loss with no applied field, 3 dB Henry factor $\alpha_{H,3dB}$, and the spectral offset or detuning of the exciton from the operating wavelength, both with and without applied field, were calculated.

Design Parameter Effects

It would be desirable to be able to distinguish the effects of changes in the design parameters. In general, however, this will not be possible because of the complexity of the interactions between the various parameters. It is useful to first understand the role each design parameter is playing and how it affects the modulator performance parameters.

The affect of the well composition parameter y_W is straight forward. Changing y_W primarily acts to change the exciton detuning without other major changes. The detuning is the spectral offset of the heavy hole exciton from the operating wavelength. This can

be seen in Table 6.2. It is through the detuning that the contrast ratio, loss, and Henry factor are affected. The bandwidth is virtually unaffected.

Table 6.1.--Design Designations

	1	2	3	4	5	6
first digit: device length (μm)	50	100	150	200	-	-
second digit: number of wells	10	15	20	25	-	-
third digit: wellwidth (nm)	12.5	13	13.5	14	14.5	15
fourth digit: barrier width (nm)	4	6	8	-	-	-
fifth digit: composition y_w	0.89	0.90	0.91	0.92	0.93	-

The detuning changes rapidly with this factor. Given current fabrication accuracies, it is not possible to hit the correct value of y_w close enough. However, in actual device operation the bias voltage or operating wavelength can be tuned to optimize the device performance.

Modifying device length also has fairly simple effects. Table 6.3 presents a series of designs that illustrates changing the length. Changing the length has no effect on the shape of the absorption spectrum calculated for an individual well and doesn't affect the applied field. The detuning is thus unchanged. Adding length simply increases the loss and contrast ratio in direct linear proportion as expected. The bandwidth is affected directly through the increase in capacitance as the length increases.

Table 6.2.--Effect of Detuning

design	yw	detuning (meV)	bandwid. (GHz)	contrast ratio (dB)	loss (dB)	$\alpha_{H,3dB}$
12421	.89	20.5	39.00	14.1	1.71	2.17
12422	.90	15.9	38.93	18.4	2.69	1.06
12423	.91	11.0	38.86	20.5	8.18	.39
12424	.92	6.4	38.80	14.8	22.57	-.47
12425	.93	1.9	38.73	2.1	41.87	-20.61

The Henry factor is a material parameter and would normally not be expected to vary with a device parameter like length, which does not affect the individual well absorption spectra. The increase in the 3 dB Henry factor in Table 6.3 demonstrates one of the differences between the conventional Henry factor and the 3 dB Henry factor. The conventional Henry factor is based on intensity and phase change between an "on" and an "off" field, neither of which are affected by device length. The 3 dB Henry factor is based on an "on" field and a field which reduces the intensity by 3 dB. Because the device length affects how quickly 3 dB of loss is achieved versus applied field, the 3 dB Henry factor is modified as well.

The effect of the remaining parameters are not so simple, mostly because they alter the total MQW thickness, d_i, and hence the built-in field, applied field, and total field shift. Designs with small d_i lead to large field shifts between the bias field and the applied field. These shifts can be so large that instead of the applied field moving the operation up the leading edge of the first heavy hole exciton, it may move the operation well beyond, into the more complex spectral region of the second heavy hole and first

light hole excitons. The effects of these parameters are more likely to depend on the values of the other parameters. Changing well thickness may have one effect when other parameters are such that the applied field is still acting on the initial slope of the first heavy hole exciton. Changing well thickness will have quite another effect if the other parameters are such that the applied field operates in the region of the other excitons.

Table 6.3.--Effect of Device Length

design	length (μm)	detuning at F_{bi} (meV)	bandwidth (GHz)	contrast ratio (dB)	loss (dB)	$\alpha_{H,3dB}$
13411	50	23.1	43.0	18.4	2.25	2.04
23411	100	23.1	27.0	36.8	4.51	2.44
33411	150	23.1	19.6	55.2	6.76	2.53
43411	200	23.1	15.4	75.3	9.02	2.57

The number of wells is one of the parameters to have such an effect. Increasing the well number decreases the change in applied field. Depending on the spectral shape of the absorption, this might decrease or increase the contrast ratio. This is somewhat offset because the greater number of wells gives greater absorption per unit length, increasing loss and contrast ratio. The situation is further complicated because the built in field is also modified, modifying the initial detuning. It was already shown above that this can modify all performance parameters except bandwidth. The effect on the 3 dB Henry factor is not straightforward because it depends in a complex way on the initial built in field, the shape of the absorption spectrum, and how quickly 3 dB loss is achieved versus applied field. The bandwidth is affected through the capacitance change with changing d_i. Table 6.4 shows a particular example. The change in detuning at bias and the change in the magnitude of the total detuning shift is apparent. In this case,

between 20 and 25 wells, the contrast ratio decreases with well number, indicating that the change in field shift is more important than the effect due to more absorption. In the 15 well case the applied field shifts the spectrum well beyond the first heavy hole exciton and results in decreased contrast ratio. The loss increases with well number, indicating that the increase in absorption due to extra wells is of greater significance than the change in detuning.

Little can be said a priori about the well width. Well width is another factor that changes the total thickness, d_i, and hence the bias and applied field. Larger well width allows greater exciton shift with applied field. However, it also reduces the exciton oscillator strength and can vary the exciton linewidth, all of which affect the shape of the absorption spectrum in a complex way.

Table 6.4.--Effect of Well Number

design	well number	detuning at F_{bi} (meV)	detuning at F_{off} (meV)	bandwidth (GHz)	contrast ratio (dB)	loss (dB)	$\alpha_{H,3dB}$
12631	15	18.8	-18.2	42.8	14.41	1.73	1.28
13631	20	22.5	-1.6	50.2	16.54	2.06	1.99
14631	25	24.4	7.2	56.0	10.48	2.13	2.14

Provided sufficient barrier width is incorporated to prevent tunneling, barrier width should not have a large effect on the single well absorption spectrum. It is another factor which changes the total thickness, and hence the built in and applied field. Alternately, a reduction in barrier width can allow more wells without affecting d_i.

Modulator Design for Long Distance

The interplay of all of the effects leading to a full modulator design is now considered. The optimum modulator design will depend on the particular application, which will dictate the requirements for bandwidth, loss, contrast ratio, and chirp. For long distance applications, the chirp will be of major importance. Dorgeuille and Devaux[59] showed that the required $\alpha_{H,3dB}$ to maximize transmission length depended upon the system jitter tolerance. For a tolerance of 20% of the bit time, the required $\alpha_{H,3dB}$ is about -0.5. For a tolerance of 10%, greater transmission length can be achieved, but only if $\alpha_{H,3dB}$ is reduced to -1.0. Figure 6.1 illustrates the loss and $\alpha_{H,3dB}$ dependence on detuning for the case in Table 6.2.

There is a basic tradeoff between device loss and chirp performance. Optimum negative Henry factors as defined in (5.18) can be achieved by operating close to the exciton, but the drawback is greater device loss. It is of interest to see which design parameters can influence this tradeoff. Well width and barrier width can potentially influence the tradeoff through their effect on the absorption spectra. Figure 6.2 shows loss vs $\alpha_{H,3dB}$ for designs in the 12xxx design series and shows that the resulting tradeoff appears independent of the well width.

Figures 6.3 and 6.4 show how the tradeoff varies with barrier width for the 12xxx and 13xxx design series. In the 12xxx series the thinner barriers appear to give lower loss for the same Henry factor. In the 13xxx series the resulting tradeoff appears independent of the barrier width.

The major factors affecting loss vs. chirp are not those affecting the absorption spectra, but the device factors of length and number of wells. These affect the total absorption and hence the loss and contrast ratio. Increasing the number of wells increases the total absorption. The result on the loss/chirp tradeoff is shown in Figure 6.5, which compares designs with 10 wells to designs with 15 and 20 wells. Only designs with greater than 10 dB contrast ratio are shown. It is seen that the lower

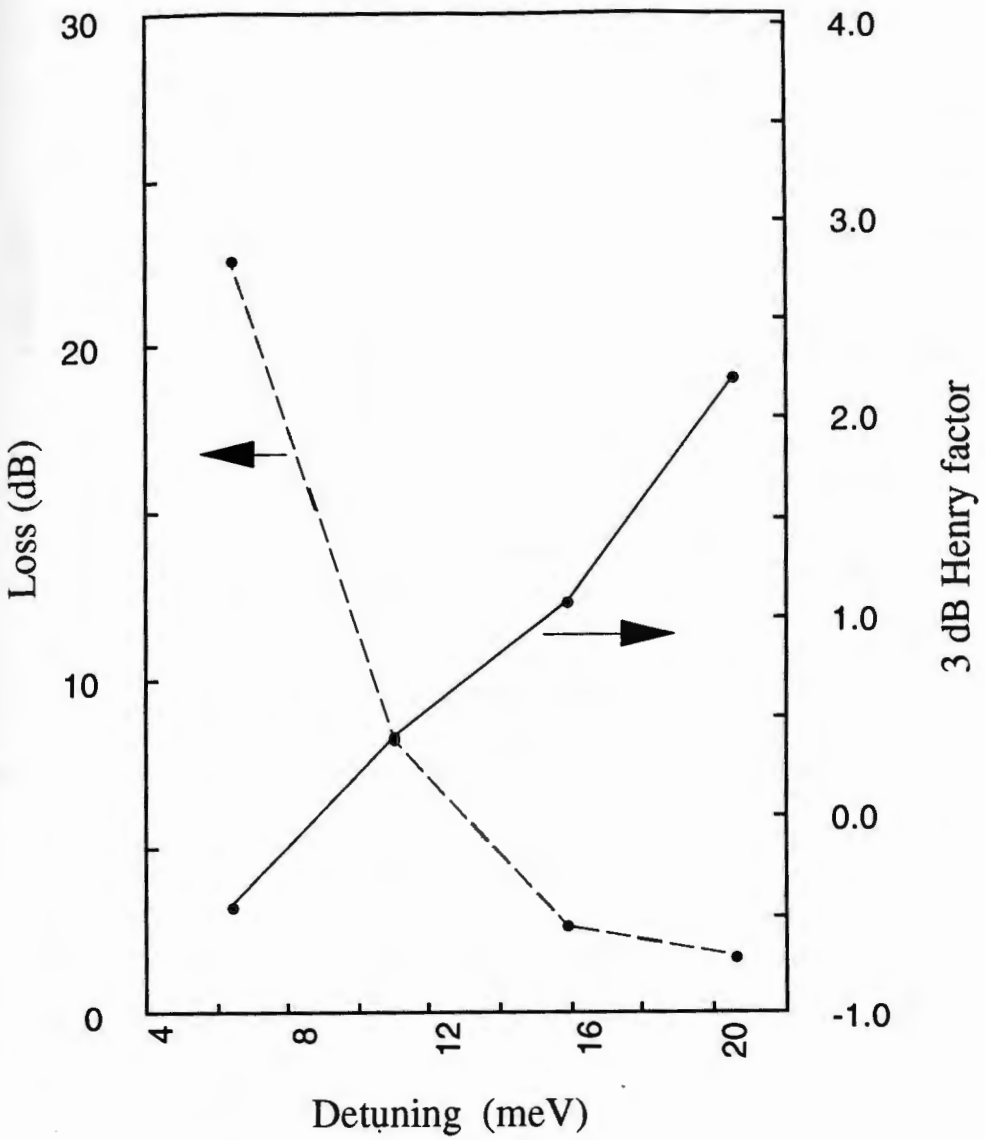

Figure 6.1. Loss and chirp dependence on detuning.

number of wells is clearly superior. However, only one of the 10 well designs achieved 10 dB contrast ratio and it didn't offer a low Henry factor.

In Figure 6.6 the 12xxx series with length of 50 microns is compared to the 22xxx series with length of 100 micron length. The extra length clearly leads to more loss for the same Henry factor.

The optimum low $\alpha_{H,3dB}$ design is guided by the observations above. It has few

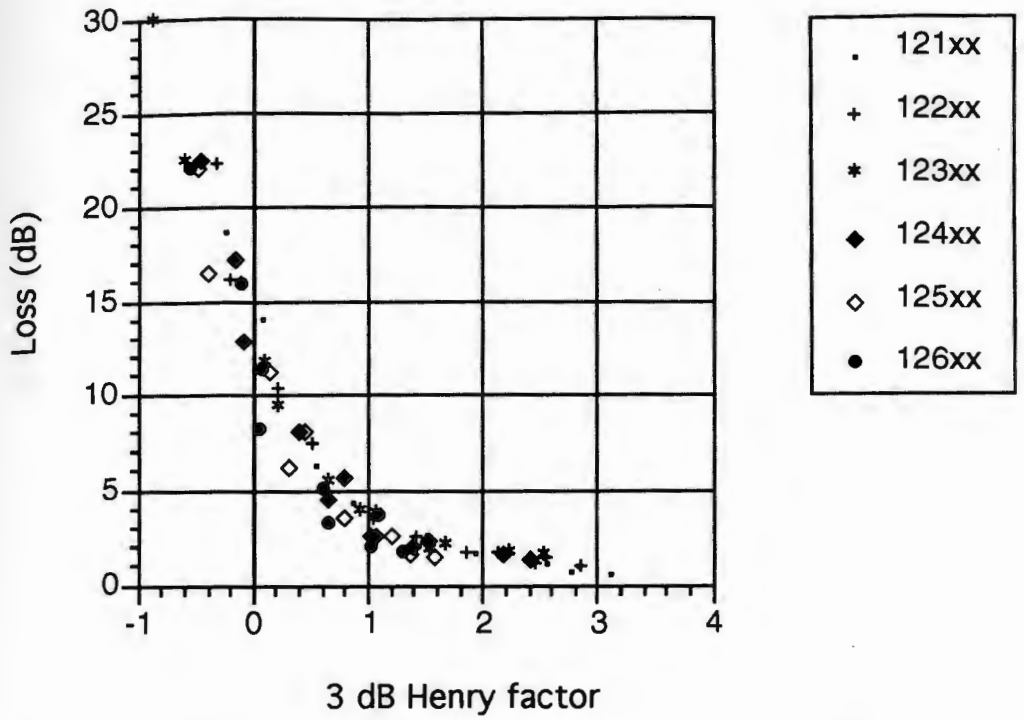

Figure 6.2. Loss/chirp tradeoff for the 12xxx design series vs. well width.

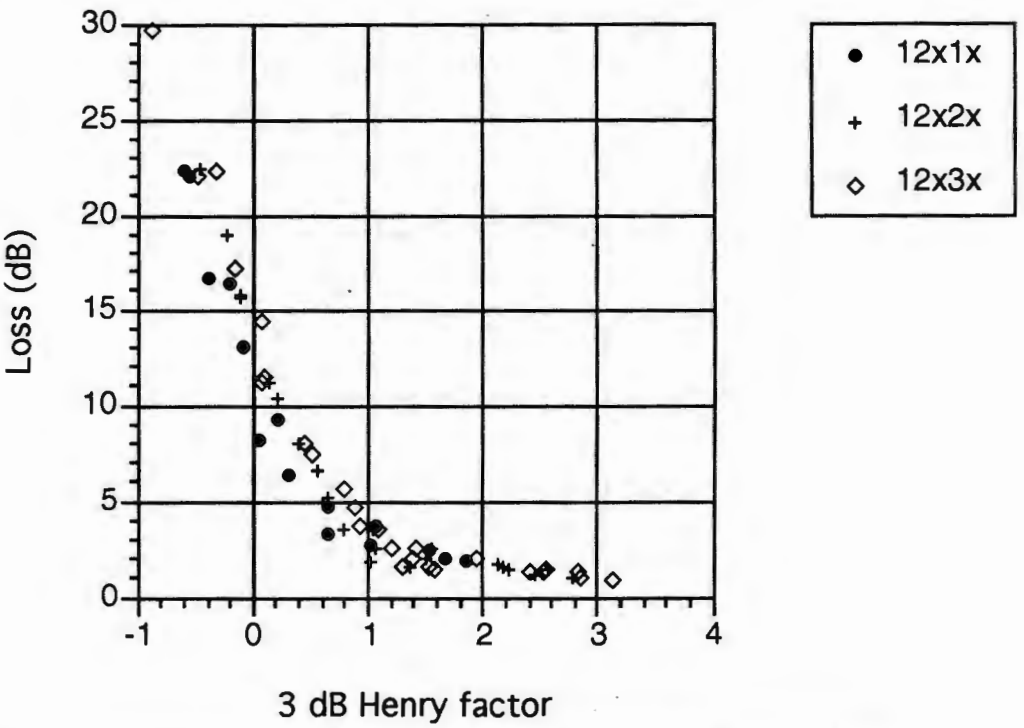

Figure 6.3. Loss/chirp tradeoff for the 12xxx design series vs. barrier width.

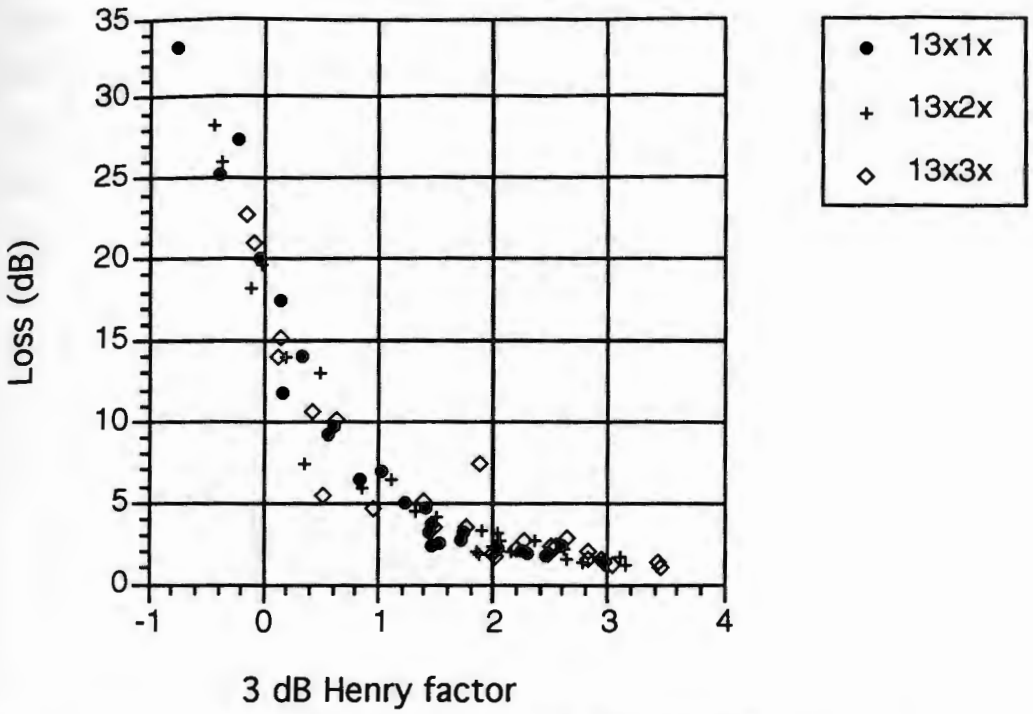

Figure 6.4. Loss/chirp tradeoff for the 13xxx design series vs. barrier width.

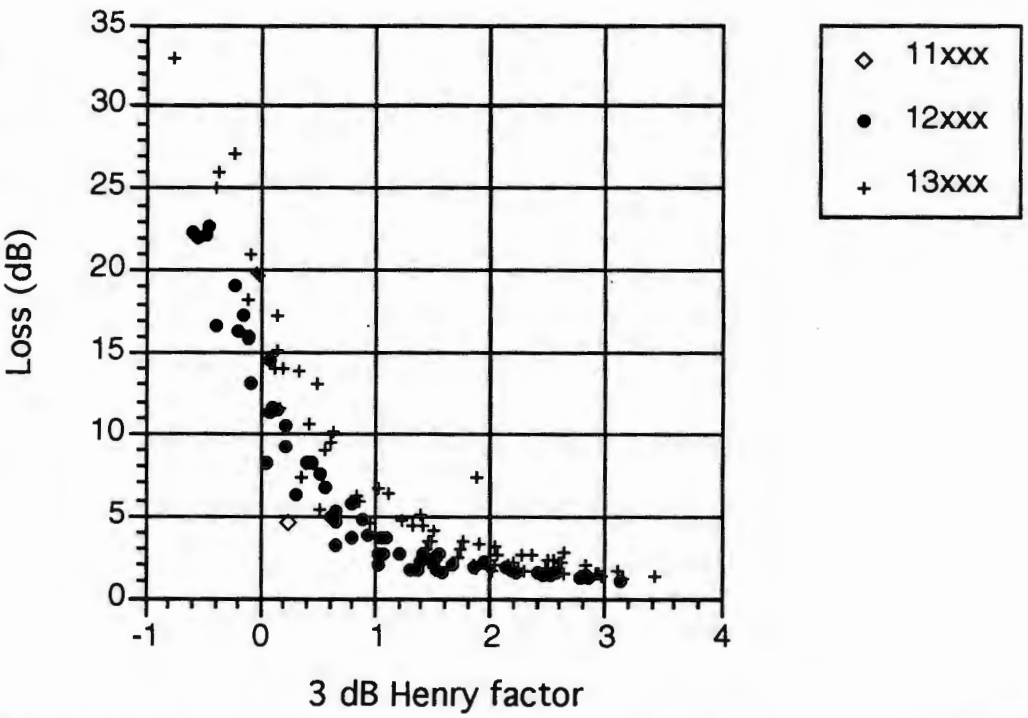

Figure 6.5. Effect of well number on loss/chirp tradeoff. The 11xxx design series has 10 wells, the 12xxx series has 15, the 13xxx series has 20.

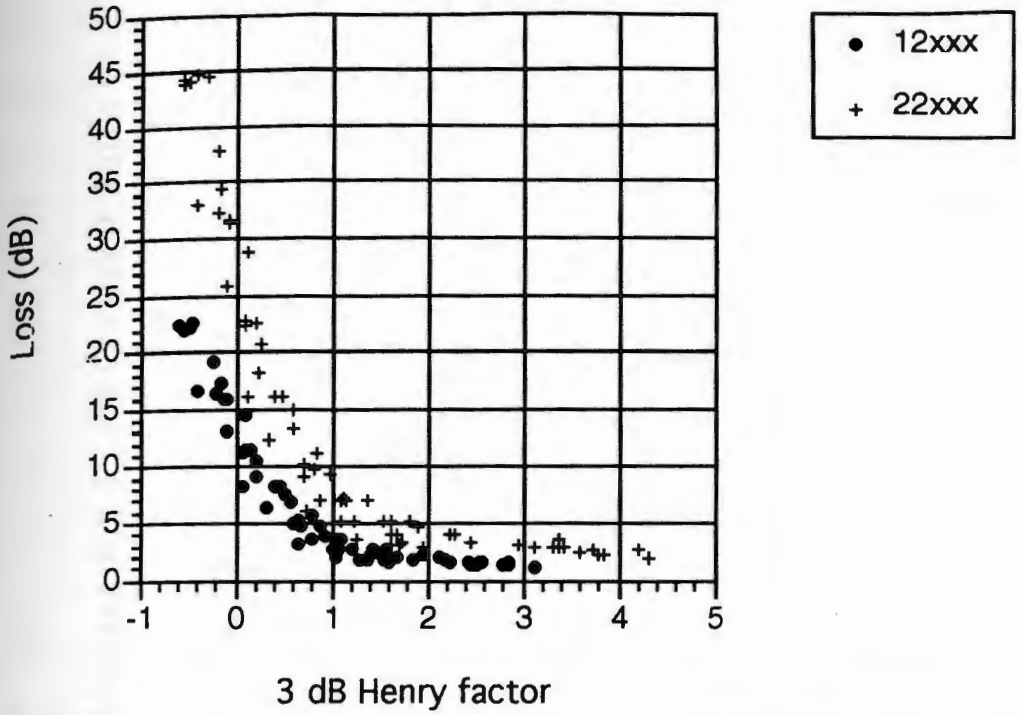

Figure 6.6. Effect of device length on loss/chirp tradeoff. The 12xxx design series has 50 micron length, the 22xxx series has 100.

enough wells to keep a favorable loss vs. chirp tradeoff, but enough to meet the contrast ratio and Henry factor requirement. The exact value will depend on the contrast ratio required by the system but will be about 15. The device is as short as possible for chirp minimization- about 50 microns. This has the added benefit of increased bandwidth. It should also have narrow barriers for optimum loss/chirp performance.

The remaining design factor to be determined is the well width. The 12x1x design determined in the last paragraph was investigated further by running the model with smaller steps in y_w to determine the correct detuning to give a 3 dB Henry factor of -0.5. Designs at different well widths were then compared when tuned in y_w for this same Henry factor. The device model was run with various drive voltages to determine the minimum drive voltage necessary to achieve 15 dB contrast ratio. These drive voltages and the design bandwidths are plotted in Figure 6.7. Unless bandwidth is critical, the plot would lead to a choice of 14.5 nm wells to minimize drive voltage.

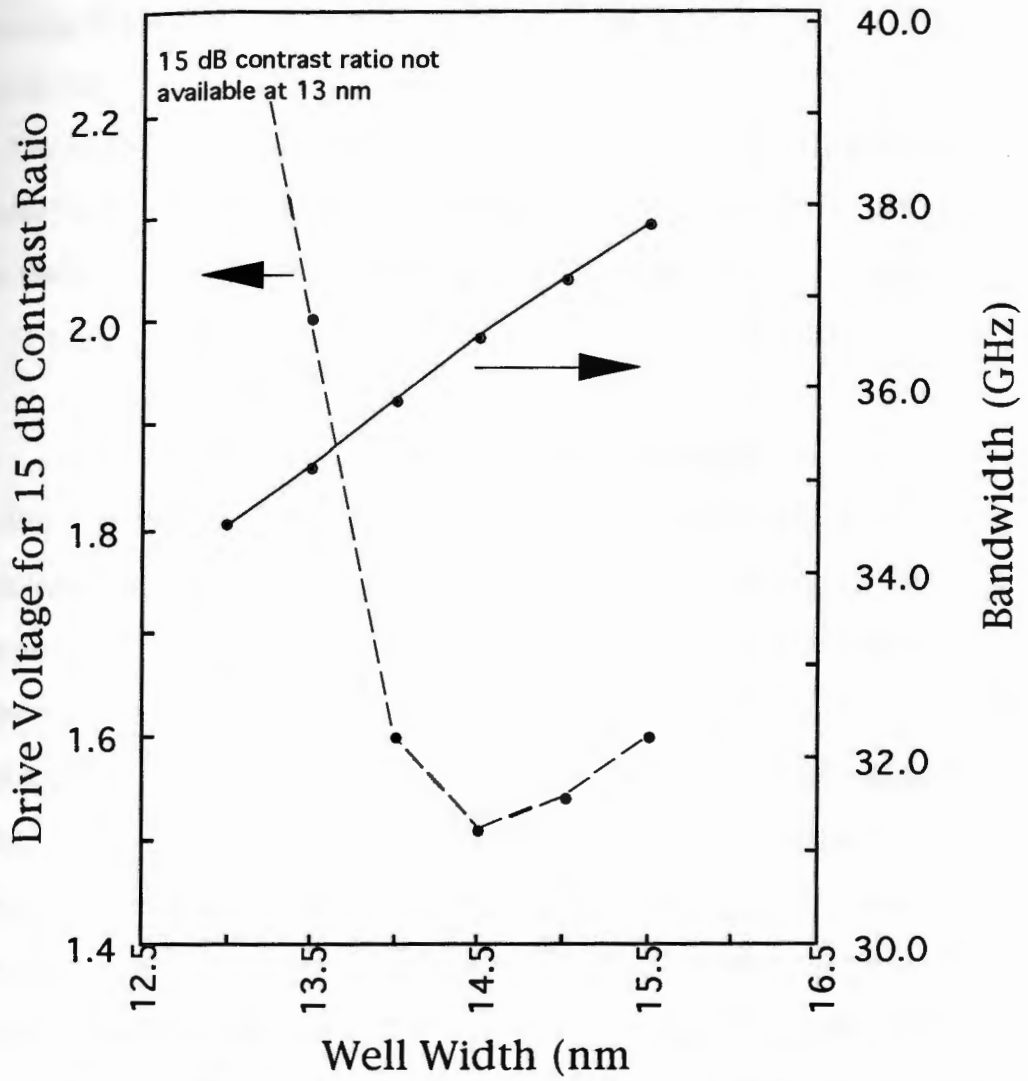

Figure 6.7. Effect of well width on the 12x1x design. Detuning is chosen for each design to give a 3dB Henry factor of -0.5.

The optimum device is slightly detuned from case 12513 and will have a 3 dB Henry factor of -0.5, a bandwidth of about 36 GHz, a contrast ratio around 15 dB, and a loss of around 18 dB. It is biased for a detuning of about 7.0 meV. Its drive voltage is 1.5 volts. This device loss is quite high compared with modulators which have been considered in the past. This work clearly indicates the tradeoff involved, and high losses will be necessary to achieve low chirp. Such a device could be acceptable if an amplifier is used after the modulator. It is possible to trade even higher loss for more bandwidth

by choosing designs with thicker barriers. The 12534 design gives 42 GHz bandwidth but 22 dB loss.

The choice of well number is the primary difference from designs that seek to maximize bandwidth without regard for chirp performance. It will be seen in a later section that such designs use the maximum number of wells technically feasible.

Modulator Design for Short Distance

When designing a modulator for short distance applications, the chirp performance is much less relevant. When a requirement for negative Henry factor is not imposed, there is freedom to design the modulator to further maximize other performance parameters. In the previous section, the necessity to minimize the chirp guided the design choices quite strictly, offering few alternatives. This is not true for the short haul modulator. Further, it is necessary to determine what performance objectives the design is to meet. In some applications the required bandwidth is given and the design task becomes to maximize the contrast and minimize loss and drive power. In other applications maximum bandwidth will be sought. The full computer model will be useful regardless of the performance requirements sought. It is not possible, however, to plot out a design chart showing how to design any of these possible devices. The full device model has six inputs and four performance outputs and cannot be presented in a single plot or even set of plots. A three dimensional plot could show only one output versus two inputs. Other two dimensional plots could show several outputs relative to a single input. The most complicated plots or sets of plots cannot present the full complexity of the model. Any attempt to hold several parameters constant while varying others, results in a plot that is a cut of the full model. While it is useful for designs close to the frozen values it says nothing of designs away from those frozen values.

Despite these limitations, much can be understood from an example. For this example an arbitrary (but typical) design goal is considered. The goal in priority order will be:

1) maximize band width as highest priority,

2) require contrast ratio greater than 15 dB,

3) minimize drive power,

4) minimize loss.

The model showed that bandwidth is maximized by choosing the shortest device and the most wells that are feasible. For this work these are designs with 50 μm length and 25 wells, designated 14xxx designs. Larger barrier widths also maximize the bandwidth by decreasing the device capacitance.

Bandwidth is also dependent upon well width through the capacitance. However, the difference is so small between the well widths considered that in most design situations the well width can be used to optimize the other performance parameters. The tradeoffs are illustrated in Figures 6.8 to 6.10. These plot contrast ratio versus loss for different well widths for the 14x3x design. The contrast versus loss curves are traced out by varying the detuning through y_w.

Figure 6.8 is plotted for a drive voltage of 1.5 volts. It can be seen that at this voltage design 1453x with 14.5 nm wells gives the lowest loss for 15 dB contrast ratio. It is followed by designs with 14 and then 15 nm wells.

Figure 6.9 is plotted for a 1.0 volt drive voltage and shows that it is possible to tradeoff loss for drive power. The best design requires 4.5 dB loss to reach 15 dB contrast ratio compared to 3 dB loss with 1.5 volt drive. It is noted that the best well width is now the 1463x case with 15 nm wells. Thus, the designer's decision concerning the loss versus drive voltage tradeoff will affect the choice of well width. Figure 6.10 shows that this tradeoff can not be carried too far because, below a certain drive level, the loss will climb rapidly for all designs.

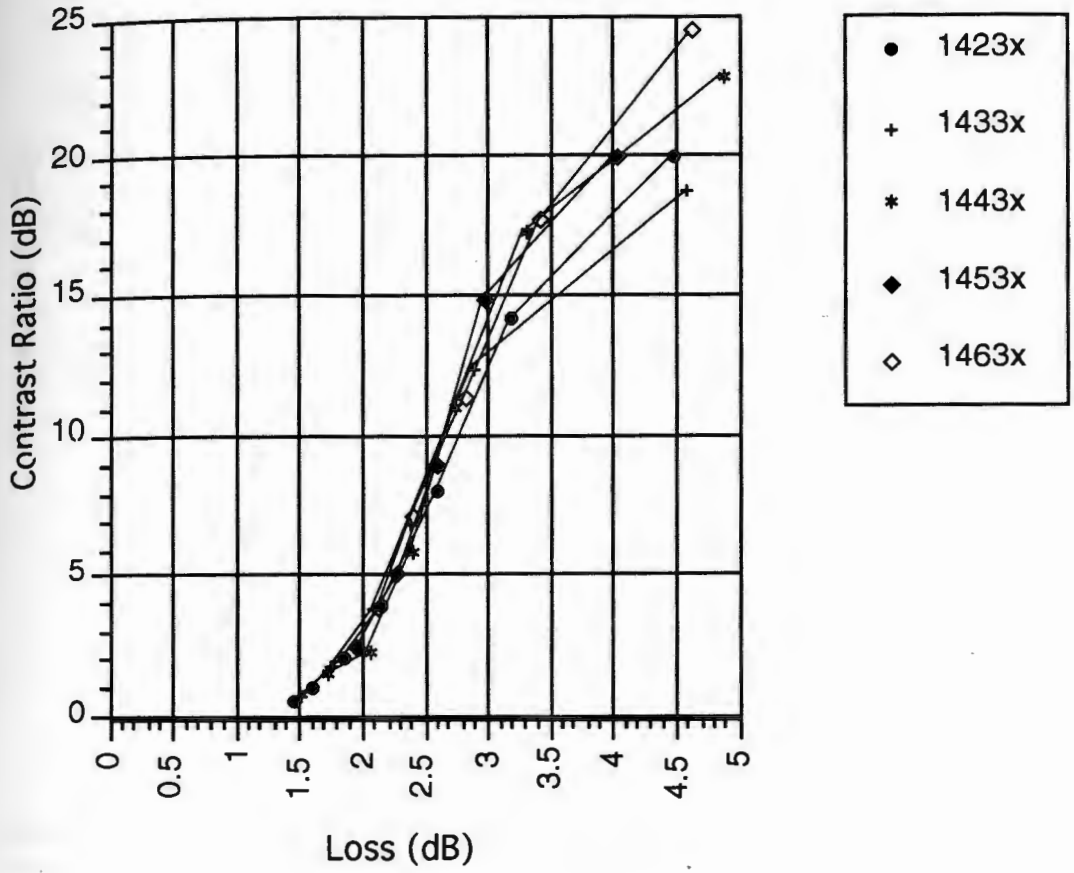

Figure 6.8. Loss versus contrast ratio for various well widths in the 14x3x design series. Drive voltage = 1.5 volt.

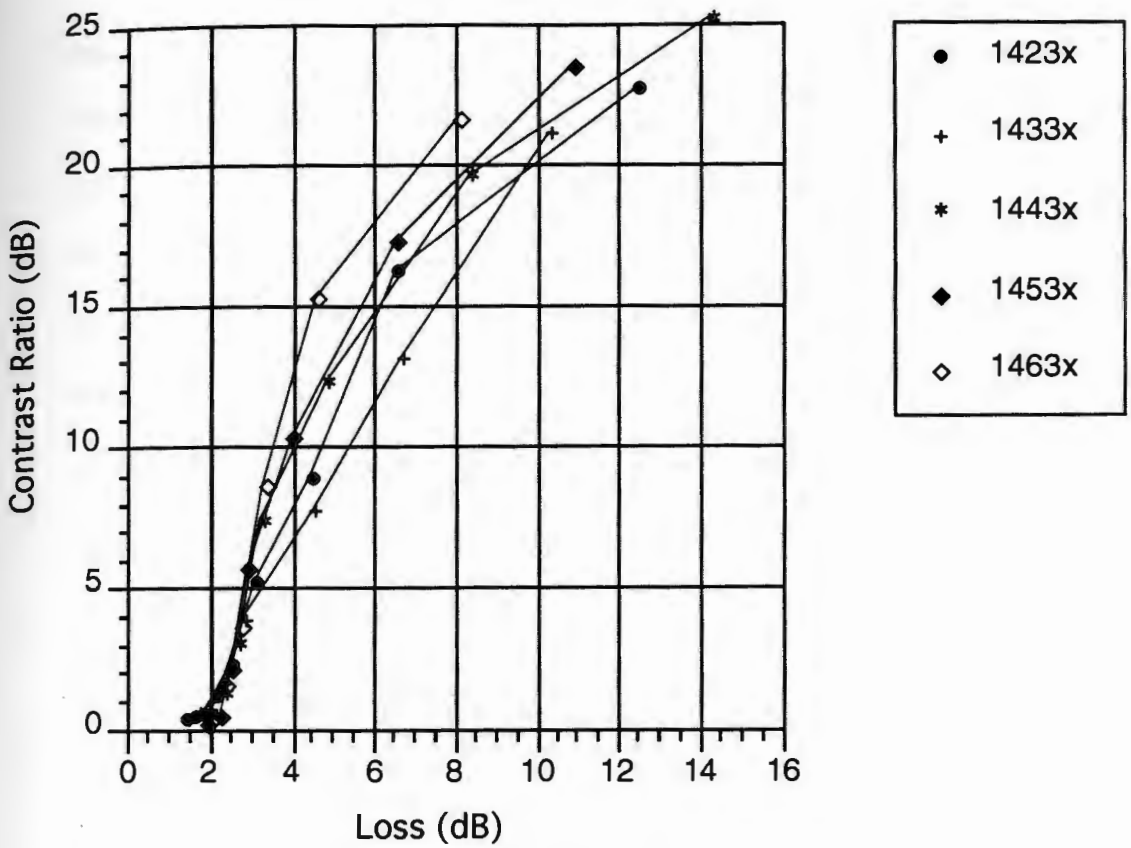

Figure 6.9. Loss versus contrast ratio for various well widths in the 14x3x design series. Drive voltage= 1.0 volt.

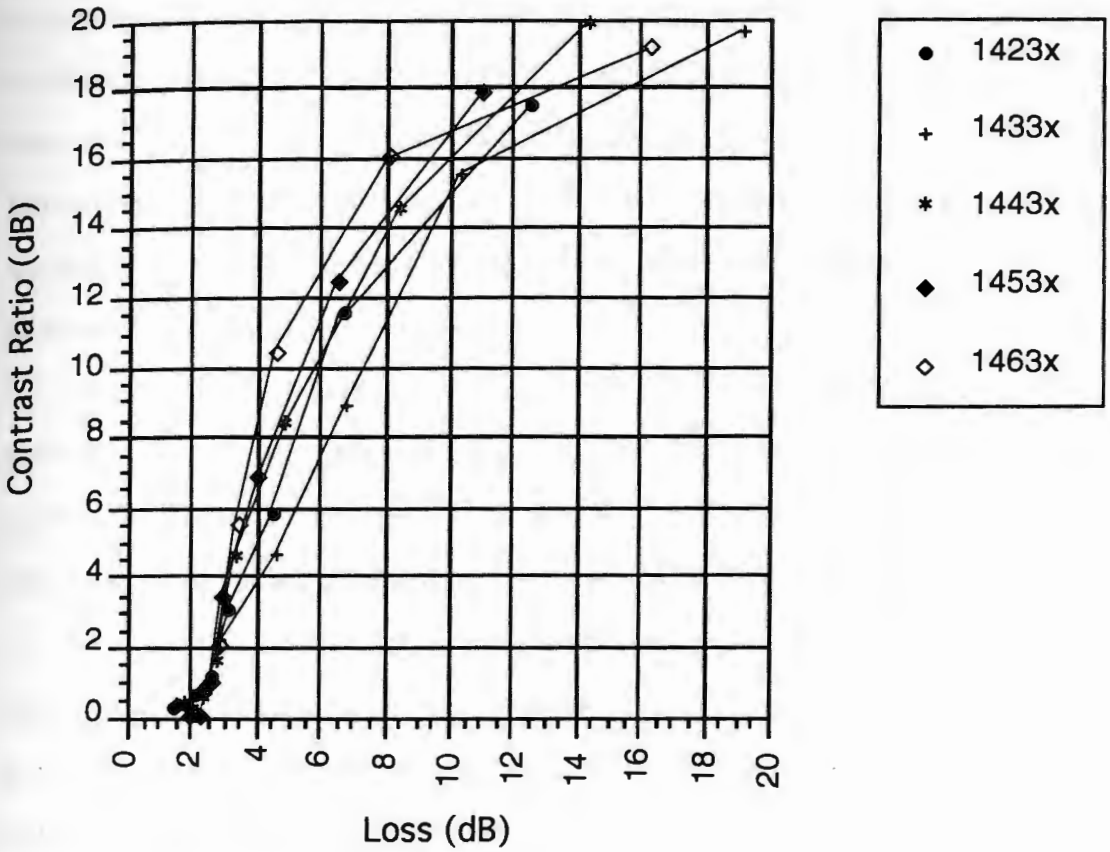

Figure 6.10. Loss versus contrast ratio for various well widths in the 14x3x design series. Drive voltage = 0.8 volt.

The way the optimum well width changes with applied voltage may be a result of two opposing effects. If there is sufficient drive voltage, the lower well width will give less linewidth and greater exciton oscillator strength leading to better contrast ratio for lower loss. As drive voltage is reduced, greater well width will give greater exciton shift. The contrast ratio enhancement due to the greater shift will play off against the oscillator strength and linewidth effects in such a way that different well widths are favored at different drive voltages.

If the low voltage option is chosen, the optimum device is slightly detuned from case 14633 and will have a bandwidth of about 56 GHz, a contrast ratio of 15 dB, and a loss of 4.5 dB. Its drive voltage is 1 volt. It is biased for a detuning of about 14.5 meV. The design is not optimized for chirp as evidenced by its 3 dB Henry factor of 1.1.

In conclusion for this chapter, it has been shown that the MQW electroabsorption modulator model can be used to evaluate a large number of possible designs. It has been shown that design optimization is possible as long as what constitutes "optimization" is well defined. Different applications with different performance requirements can lead to distinctly different optimized device designs. For long distance applications where device chirp is important, the devices must be tuned closer to the exciton, with higher loss resulting. This loss can be tolerated if an optical amplifier is used prior to transmission. Minimizing the loss led to a design with 15 wells. For short distance applications, chirp is no longer of concern, and the design may be concentrated on optimization of the remaining performance parameters. If bandwidth is the top priority the design is optimized by the largest number of wells that is feasible. Well width is determined by the choice in a tradeoff between loss and drive voltage.

CHAPTER 7

CONCLUSIONS

A detailed theoretical model of electroabsorption in InGaAsP multi-quantum wells has been developed. Though similar to previous theoretical models for GaAs/AlGaAs structures, the model includes significant improvements in the handling of excitonic linewidth and the variation of exciton oscillator strength with applied field. The model calculates both the absorption spectra and the refractive index change spectra for different applied fields. Results of the electro-absorption model were compared with two sets of experimental data on InGaAsP MQWs. It was shown that with appropriate choices of several parameters related to the MQW fabrication quality, it could effectively describe both the shape of the absorption edge, its shift with applied field, and the decrease in oscillator strength with applied field. The model clearly demonstrated that it is necessary to include the first heavy hole, second heavy hole, and first light hole excitons as well as the effect of the continuum.

This material model was then used to calculate the performance of MQW modulator devices as part of a multi-parameter design optimization. The performance factors of bandwidth, loss, contrast ratio, drive voltage, and chirp performance were all considered, rather than using figures of merit which ignore or inadequately prioritize these factors. The design of a modulator to give optimum chirp performance over long transmission distances was investigated. It was shown that by using present fiber or semiconductor optical amplifiers, higher device loss can be tolerated, allowing operation tuned closer to the exciton to optimize the chirp. The loss versus chirp tradeoff can be optimized through use of short device length, small well number, and small barrier thickness. Well width of 14.5 nm gave the lowest drive voltage requirement. The design

of a modulator for typical short distance transmission was also considered. When chirp performance is ignored, it is possible to further optimize the remaining performance factors. The choice of a large well number is the main result to distinguish these designs from designs that optimize chirp performance. The choice of well width was found to involve a tradeoff of lower drive voltage versus higher loss.

The two design examples showed that there are numerous tradeoffs to be made between the various performance parameters. They also showed that performance can be significantly improved through optimized design. The proper prioritization of the various performance parameters will depend upon the specific application and such factors as the transmission distance, the loss budget, the ability to include an optical amplifier, the contrast ratio requirements, the drive power available, and the bandwidth desired. Furthermore, the model is sufficiently complicated that the tradeoffs change with the design parameters and cannot be generalized. In such cases the judgement of a human designer who can weigh all the factors can be very valuable. This device model gives the designer the tool required to make those judgements.

REFERENCES

1. I. Kotaka, K. Wakita, O. Mitomi, H. Asai, and Y. Kawamura, "High-Speed InGaAlAs/InAlAs Multiple Quantum Well Optical Modulators with Bandwidths in Excess of 20 GHz at 1.55 μm," IEEE Phot. Tech. Lett., **1**, pp. 100-101, 1989.

2. G. Mak, C. Rolland, K. Fox, and C. Blaauw, "High-Speed Bulk InGaAsP-InP Electroabsorption Modulators with Bandwidths in Excess of 20 GHz," IEEE Phot. Tech. Lett., **2**, pp. 730-733, 1990.

3. E. Yamada, K. Wakita, and M. Nakazawa, "30 GHz Pulse Train Generation From a Multiquantum Well Electroabsorption Intensity Modulator," Elect. Lett., **29**, pp. 845-847, 1993.

4. D. Miller et al., "Band-Edge Electroabsorption in Quantum Well Structures: The Quantum-Confined Stark Effect," Phys. Rev. Lett., **53**, pp. 2173-2176, 1984.

5. D. Miller et al., "Electric Field Dependence of Optical Absorption Near the Band Gap of Quantum-well Structures," Phys. Rev. B, **32**, pp. 1043-1060, 1985.

6. S. Nojima and K. Wakita, "Optimization of Quantum Well Materials and Structures for Excitonic Electroabsorption Effects," Appl. Phys. Lett., **53**, pp. 1958-1960, 1988.

7. D. Miller, D. Chemla, and S. Schmitt-Rink, "Relation Between Electroabsorption in Bulk Semiconductors and in Quantum Wells: The Quantum-confined Franz-Kedysh Effect," Phys. Rev. B, **33**, pp. 6976-6982, 1986.

8. D. Miller, J. Weiner, and D. Chemla, "Electric-Field Dependence of Linear Optical Properties in Quantum Well Structures: Waveguide Electroabasorption and Sum Rules," IEEE J. of Quantum Elec., **22**, pp. 1816-1830, 1986.

9. J. Brum and G. Bastard, "Electric-Field-Induced Dissociation of Excitons in Semiconductor Quantum Wells," Phys. Rev. B, **31**, pp. 3893-3898, 1985.

10. G. Bastard, E. Mendez, L. Chang, and L. Esaki, "Variational Calculations on a Quantum Well in an Electric Field," Phys. Rev. B, **28**, pp. 3241-3245, 1983.

11. P. Klipstein and N. Apsley, "A Theory for the Electroreflectance Spectra of Quantum Well Structures," J. Phys. C: Solid State Phys., **19**, pp. 6461-6478, 1986.

12. M. Matsuura and T. Kamizato, "Subbands and Excitons in a Quantum Well in an Electric Field," Phys. Rev. B, **33**, pp. 8385-8389, 1986.

13. H. Cho and P. Prucnal, "Effect of Parameter Variations on the Performance of GaAs/AlGaAs Multiple-Quantum-Well Electroabsorption Modulators," IEEE J. of Quantum Elec., **25**, pp. 1682-1690, 1989.

14. J. Singh, "Theory of Photoluminescence in Quantum Wells in the Presence of Transverse Electric Field: Monte Carlo Approach," J. Appl. Phys., **59**, pp 2953-2957, 1986.

15. G. Sanders and K. Bajaj, "Electronic Properties and Optical-Absorption Spectra of GaAs-AlGaAs Quantum Wells in Externally Applied Electric Fields," Phys. Rev. B, **35**, pp. 2308-2320, 1987.

16. P. Stevens, M. Whitehead, G. Parry, and K. Woodbridge, "Computer Modeling of the Electric Field Dependent Absorption Spectrum of Multiple Quantum Well Material," IEEE J. of Quantum Elec., **24**, pp. 2007-2015, 1988.

17. G. Lengyel, K. Jelley, and R. Engelmann, "A Semi-Empirical Model for Electroabsorption in GaAs/AlGaAs Multiple Quantum Well Modulator Structures," IEEE J. of Quantum Elec., **26**, pp. 296-1304, 1990.

18. M. Sugawara, T. Fujii, S. Yamazaki, and K. Nakajima, "Optical Characteristics of Excitons in InGaAsP/InP Quantum Wells," Phys. Rev. B, **44**, pp. 1782-1791, 1991.

19. J. Zucker, I. Bar-Joseph, B. Miller, U. Koren, and D. Chemla, "Quaternary Quantum Wells for Electro-optic Intensity and Phase Modulation at 1.3 and 1.55 mm," Appl. Phys. Lett., **54**, pp. 10-12, 1989.

20. C. Rolland, R. Moore, F. Shepherd, and G. Hillier, "10 Gbit/s, 1.56 μm Multiquantum Well InP/InGaAsP Mach-Zehnder Optical Modulator," Elect. Lett., **29**, pp. 471-472, 1993.

21. K. Sato, K. Wakita, and M. Yamamoto, "Strained InGaAsP Multiquantum Wells for Optical Electroabsorption Waveguide Modulators," Elect. Lett., **28**, pp. 609-610, 1992.

22. M. Chin and W. Chang, "Theoretical Design Optimization of Multiple-Quantum-Well Electroabsorption Waveguide Modulators," IEEE J. of Quantum Elec., **29**, pp. 2476-2488, 1993.

23. A. Bandyopadhyay and P. Basu, "Modeling of Excitonic Electrorefraction in InGaAsP Multiple Quantum Wells," IEEE J. of Quantum Electron., **29**, pp. 2724-2730, 1993.

24. M. Chin, "Optical Confinement Factor in Waveguide Electroabsorption Modulators: Design and Measurement," IEEE Phot. Tech. Lett., **6**, pp. 945-948, 1994.

25. K. Kawano, K. Wakita, O. Mitomi, I. Kotaka, and M. Naganuma, "Design of InGaAs-InAlAs Multiple-Quantum-Well (MQW) Optical Modulators," IEEE J. of Quantum Elec., **28**, pp. 224-229, 1992.

26. G. Sanders and Y. Chang, "Optical Properties in Modulation-doped GaAs-GaAlAs Quantum Wells," Phys. Rev. B, **31**, pp. 6892-6895, 1985.

27. G. Sanders and Y. Chang, "Effect of Band Hybridization on Exciton States in GaAs-AlGaAs Quantum Wells," Phys. Rev. B, **32**, pp. 5517-5520, 1985.

28. P. Debernardi and P. Fasano, "Quantum Confined Stark Effect in Semiconductor Quantum Wells Including Valence Band Mixing and Coulomb Effects," IEEE J. of Quant. Elec., **29**, pp. 2741-2755, 1993.

29. K. Brennan and C. Summers, "Theory of Resonant Tunneling in a Variably Spaced Multiquantum Well Structure: an Airy Function Approach," J. Appl. Phys., **61**, pp. 614-623, 1987.

30. J. Singh and S. Hong, "Theory of Electric Field-Induced Optical Modulation in Single and Multiquantum Well Structures Using a Monte Carlo Approach," IEEE J. of Quantum Elec., **QE-22**, pp. 2017-2021, 1986.

31. A. Harwit and J. Harris, "Calculated Quasi-eigenstates and Quasi-eigenenergies of Quantum Well Superlattices in an Applied Electric Field," J. Appl. Phys., **60**, pp. 3211-3213, 1986.

32. S. Datta. Quantum Phenomena. Modular Series on Solid State Devices, Vol. VIII. Reading, Massachusetts: Addison-Wesley Publishing Company, 1989.

33. M. Sugawara, T. Fujii, S. Yamazaki, and K. Nakajima, "Theoretical and Experimental Study of the Optical-Absorption Spectrum of Exciton Resonance in InGaAs/InP Quantum Wells," Phys. Rev. B, **42**, pp. 9587-9507, 1990.

34. S. Hong and J. Singh, "Excitonic Energies and Inhomogeneous Line Broadening Effects in InAlAs/InGaAs Modulator Structures," J. Appl. Phys., **62**, pp. 1994-1999, 1987.

35. D. Chemla, D. Miller, P. Smith, A. Gossard, and W. Wiegmann, "Room Temperature Excitonic Nonlinear Absorption and Refraction in GaAs/AlGaAs Multiple Quantum Well Structures," IEEE J. Quantum Elec., **QE-20**, pp. 265-275, 1984.

36. M. Sugawara, T. Fujii, M. Kondo, K. Kato, K. Domen, S. Yamazaki, and K. Nakajima, "Evaluation of Exciton Absorption Peak Broadening Factors in InGaAsP/InP Multiple Quantum Wells," Appl. Phys. Lett., **53**, pp. 2290-2292, 1988.

37. O. Goede, L. John, and D. Hennig, "Compositional Disorder-Induced Broadening for Free Excitons in II-VI Semiconducting Mixed Crystals," Phys. Stat. Sol., **89**, pp. K183-K186, 1978.

38. E. Schubert, E. Gobel, Y. Horikoshi, K. Ploog, and H. Queisser, "Alloy Broadening in Photoluminiscence Spectra of AlGaAs," Phys. Rev. B, **30**, pp. 813-820, 1984.

39. J. Singh and K. Bajaj, "Theory of Excitonic Photoluminescence Linewidth in Semiconductor Alloys," Appl. Phys. Lett., **44**, pp. 1075-1077, 1984.

40. J. Singh and K. Bajaj, "Quantum Mechanical Theory of Linewidths of Localized Radiative Transitions in Semiconductor Alloys," Appl. Phys. Lett., **48**, pp. 1077-1079, 1986.

41. D. Welch, G. Wicks, and L. Eastman, "Luminescence Line Shape Broadening Mechanisms in GaInAs/AlInAs Quantum Wells," Appl. Phys. Lett., **46**, pp. 991-993, 1985.

42. J. Singh and K. Bajaj, "Role of Interface Roughness and Alloy Disorder in Photoluminescence in Quantum-well Structures," J. Appl. Phys., **57**, pp. 5433-5437, 1985.

43. S. Ogale, A. Madhukar, F. Voillot, M. Thomsen, W. Tang, T. Lee, J. Kim, and P. Chen, "Atomistic Nature of Heterointerfaces in III-V Semiconductor-based Quantum-well Structures and Its Consequences for Photoluminescence Behavior," Phys. Rev. B, **36**, pp. 1662-1672, 1987.

44. M. Sugawara, T. Fujii, S. Yamazaki, and K. Nakajima, "Room Temperature Exciton Optical Absorption Peaks in InGaAsP/InP Multiple Quantum Wells," Appl. Phys. Lett., **54**, pp. 1353-1355, 1989.

45. D. Bimberg, D. Mars, J. Miller, R. Bauer, D. Oertel, and J. Christen, "Kenetics of Island Formation at the Interfaces of AlGaAs/GaAs/AlGaAs Quantum Wells Upon Growth Interruption," Superlattices and Microstuctures, **3**, pp. 79-87, 1987.

46. D. Bimberg, J. Christen, T. Fukunaga, H. Nakashima, D. Mars, and J. Miller, "Cathodoluminescence Atomic Scale Images of Monolayer Islands at GaAs/GaAlAs Interfaces," J. Vac. Sci. Tech. B, **5**, pp. 1191-1197.

47. J. Woo, S. Rhee, Y. Kim, H. Ko, W. Kim, and D. Kim, "Bimodal Roughness of Heterointerface in Quantum Wells Analyzed by Photoluminescence Excitation Spectroscopy," Appl. Phys. Lett., 66, pp. 338-340, 1995.

48. F. Juang, J. Singh, and P. Bhattacharya, "Field-dependent Linewidths and Photoluminescence Energies in GaAs-AlGaAs Multiquantum Well Modulators," Appl. Phys. Lett., **48**, pp. 1246-1248, 1986.

49. E. Schubert and W. Tsang, "Photoluminescence Line Shape of Excitons in Alloy Semiconductors," Phys. Rev. B, **34**, pp. 2991-2294, 1986.

50. R. J. Elliot, "Intensity of Optical Absorption by Excitons," Phys. Rev., **108**, pp. 1384-1389, 1957.

51. M. Shinada and S. Sugano, "Interband Optical Transitions in Extremely Anisotropic Semiconductors, I. Bound and Unbound Exciton Absorption," J. Phys. Soc. Japan, **21**, pp. 1938-1946, 1965.

52. K. Chan, "Theory of Optical Absorption Due to Unbound States of An Exciton in a Quantum Well," J. Phys. C, **20**, pp. 791-799, 1987.

53. J. Wu and A Nurmikko, "Stark Shifts on Exciton Luminescence in Quantum Wells: Effect of Coulomb Interaction," Phys. Rev. B, **36**, pp. 4902-4905, 1987.

54. K. Utaka, Y. Suematsu, K. Kobayashi, and H. Kawanishi, "GaInAsP/InP Integrated Twin-Guide Lasers with First-Order Distributed Bragg Reflectors at 1.3 μm Wavelength," Japan. J. of App. Phys., **19**, pp. L137-L140, 1980.

55. P. Chandra, L. Coldren, and K. Strege, "Refractive Index Data From $Ga_xIn_{1-x}As_yP_{1-y}$ Films, Elec. Lett., **17**, pp. 6-7, 1981.

56. R. Nahory and M. Pollack, "Threshold Dependence On Active-Layer Thickness in InGaAsP/InP D. H. Lasers," Elec. Lett., **14**, pp. 727-729, 1978.

57. G. Agrawal and N. Dutta, Long-Wavelength Semiconductor Lasers. New York: Van Nostrand Reinhold, 1986.

58. J. Weiner, D. Miller, D. Chemla, "Quadratic Electro-Optic Effect Due to the Quantum-Confined Stark Effect in Quantum Wells," Appl. Phys. Lett., **50**, pp. 842-844, 1987.

59. F. Dorgeuille and F. Devaux, "On the Transmission Performances and the Chirp Parameter of a Multiple-Quantum-Well Electroabsorption Modulator," IEEE J. of Quantum Electron.,**30**, pp. 2565-2572, 1994.

60. F. Koyama and K. Iga, "Frequency Chirping in External Modulators," IEEE J. of Lightwave Technol., **6**, pp. 87-92, 1988.

61. A. Gnauck, S. Korotky, J. Veselka, J. Nagel, C. Kemmerer, W. Minford, and D. Moser, "Dispersion Penalty Reduction Using an Optical Modulator with Adjustable Chirp," IEEE J. of Lightwave Technol., **3**, pp. 916-918, 1991.

BIBLIOGRAPHY

Agrawal, D. and Dutta, N., Long-Wavelength Semiconductor Lasers. New York: Van Nostrand Reinhold, 1986.

Bandyopadhyay, A. and Basu, P., "Modeling of Excitonic Electrorefraction in InGaAsP Multiple Quantum Wells," IEEE Journal of Quantum Electronics, **29**,pp. 2724-2730, 1993.

Bastard, G., Mendez, E., Chang, L., and Esaki, L., "Variational Calculations on a Quantum Well in an Electric Field," Physical Review B, **28**, pp. 3241-3245,1983.

Bimberg, D., Christen, J., Fukunaga, T., Nakashima, H., Mars, D., and Miller, J., "Cathodoluminescence Atomic Scale Images of Monolayer Islands at GaAs/GaAlAs Interfaces," Journal of Vacuum Science Technology B, **5**, pp. 1191-1197, 1987.

Bimberg, D., Mars, D., Miller, J., Bauer, R., Oertel. D., and Christen, J., "Kenetics of Island Formation at the Interfaces of AlGaAs/GaAs/AlGaAs Quantum Wells Upon Growth Interruption," Superlattices and Microstuctures, **3**, pp. 79-87, 1987.

Brennan, K. and Summers, C., "Theory of Resonant Tunneling in a Variably Spaced Multiquantum Well Structure: an Airy Function Approach," Journal of Applied Physics, **61**, pp. 614-623, 1987.

Brum, J. and Bastard, G., "Electric-Field-Induced Dissociation of Excitons in Semiconductor Quantum Wells," Physical Review B, **31**, pp. 3893-3898, 1985.

Chan, K., "Theory of Optical Absorption Due to Unbound States of An Exciton in a Quantum Well," Journal of Physics C, **20**, pp. 791-799, 1987.

Chandra, P., Coldren, L., and Strege, K., "Refractive Index Data From $Ga_xIn_{1-x}As_yP_{1-y}$ Films, Electronics Letters, **17**, pp. 6-7, 1981.

Chemla, D., Miller, D., Smith, P., Gossard, A., and Wiegmann, W., "Room Temperature Excitonic Nonlinear Absorption and Refraction in GaAs/AlGaAs Multiple Quantum Well Structures," IEEE Journal of Quantum Electronics, **QE-20**, pp. 265-275, 1984.

Chin, M. and Chang, W., "Theoretical Design Optimization of Multiple-Quantum-Well Electroabsorption Waveguide Modulators," IEEE Journal of Quantum Electronics, **29**, pp. 2476-2488, 1993.

Chin, M., "Optical Confinement Factor in Waveguide Electroabsorption Modulators: Design and Measurement," IEEE Photonics Technology Letters, **6**, pp. 945-948, 1994.

Cho, H. and Prucnal, P., "Effect of Parameter Variations on the Performance of GaAs/AlGaAs Multiple-Quantum-Well Electroabsorption Modulators," IEEE Journal of Quantum Electronics, **25**, pp. 1682-1690, 1989.

Datta, S., Quantum Phenomena. Modular Series on Solid State Devices, Vol. VIII. Reading, Massachusetts: Addison-Wesley Publishing Company, 1989.

Debernardi, P. and Fasano, P., "Quantum Confined Stark Effect in Semiconductor Quantum Wells Including Valence Band Mixing and Coulomb Effects," IEEE Journal of Quantum Electronics, **29**, pp. 2741-2755, 1993.

Dorgeuille, F. and Devaux, F., "On the Transmission Performances and the Chirp Parameter of a Multiple-Quantum-Well Electroabsorption Modulator," IEEE Journal of Quantum Electronics,**30**, pp. 2565-2572, 1994.

Elliot, R., "Intensity of Optical Absorption by Excitons," Physical Review, **108**, pp. 1384-1389, 1957.

Gnauck, A., Korotky, S., Veselka, J., Nagel, J., Kemmerer, C., Minford, W., and Moser, D., "Dispersion Penalty Reduction Using an Optical Modulator with Adjustable Chirp," IEEE Journal of Lightwave Technology, **3**, pp. 916-918, 1991.

Goede, O., John, L., and Hennig, D., "Compositional Disorder-Induced Broadening for Free Excitons in II-VI Semiconducting Mixed Crystals," Physica Status Solidi, **89**, pp. K183-K186, 1978.

Harwit, A. and Harris, J., "Calculated Quasi-eigenstates and Quasi-Eigenenergies of Quantum Well Superlattices in an Applied Electric Field," Journal of Applied Physics, **60**, pp. 3211-3213, 1986.

Hong, S. and Singh, J., "Excitonic Energies and Inhomogeneous Line Broadening Effects in InAlAs/InGaAs Modulator Structures," Journal of Applied Physics, **62**, pp. 1994-1999, 1987.

Juang, F., Singh, J., and Bhattacharya, P., "Field-dependent Linewidths and Photoluminescence Energies in GaAs-AlGaAs Multiquantum Well Modulators," Applied Physics Letters, **48**, pp. 1246-1248, 1986.

Kawano, K., Wakita, K., Mitomi, O., Kotaka, I., and Naganuma, M., "Design of InGaAs-InAlAs Multiple-Quantum-Well (MQW) Optical Modulators," IEEE Journal of Quantum Electronics, **28**, pp. 224-229, 1992.

Klipstein, P. and Apsley, N., "A Theory for the Electroreflectance Spectra of Quantum Well Structures," Journal of Physics C: Solid State Physics, **19**, pp. 6461-6478, 1986.

Kotaka, I., Wakita, K., Mitomi, O., Asai, H., and Kawamura, Y., "High-Speed InGaAlAs/InAlAs Multiple Quantum Well Optical Modulators with Bandwidths in Excess of 20 GHz at 1.55 μm," IEEE Photonics Technology Letters, **1**, pp. 100-101, 1989.

Koyama, F. and Iga, K., "Frequency Chirping in External Modulators," IEEE Journal of Lightwave Technology, **6**, pp. 87-92, 1988.

Lengyel, G., Jelley, K., and Engelmann, R., "A Semi-Empirical Model for Electroabsorption in GaAs/AlGaAs Multiple Quantum Well Modulator Structures," IEEE Journal of Quantum Electronics, **26**, pp. 296-1304, 1990.

Mak, G., Rolland, C., Fox, K., and Blaauw, C., "High-Speed Bulk InGaAsP-InP Electroabsorption Modulators with Bandwidths in Excess of 20 GHz," IEEE Photonics Technology Letters, **2**, pp. 730-733, 1990.

Matsuura, M. and Kamizato, T., "Subbands and Excitons in a Quantum Well in an Electric Field," Physical Review B, **33**, pp. 8385-8389, 1986.

Miller, D. et al., "Band-Edge Electroabsorption in Quantum Well Structures: The Quantum-Confined Stark Effect," Physical Review Letters, **53**, pp. 2173-2176, 1984.

Miller, D. et al., "Electric Field Dependence of Optical Absorption Near the Band Gap of Quantum-well Structures," Physical Review B, **32**, pp. 1043-1060, 1985.

Miller, D., Chemla, D., and Schmitt-Rink, S., "Relation Between Electroabsorption in Bulk Semiconductors and in Quantum Wells: The Quantum-confined Franz-Kedysh Effect," Physical Review B, **33**, pp. 6976-6982, 1986.

Miller, D., Weiner, J., and Chemla, D., "Electric-Field Dependence of Linear Optical Properties in Quantum Well Structures: Waveguide Electroabasorption and Sum Rules," IEEE Journal of Quantum Electronics, **22**, pp. 1816-1830, 1986.

Nahory, R. and Pollack, M., "Threshold Dependence On Active-Layer Thickness in InGaAsP/InP D. H. Lasers," Electronics Letters, **14**, pp. 727-729, 1978.

Nojima, S. and Wakita, K., "Optimization of Quantum Well Materials and Structures for Excitonic Electroabsorption Effects," Applied Physics Letters, **53**, pp. 1958-1960, 1988.

Ogale, S., Madhukar, A., Voillot, F., Thomsen, M., Tang, W., Lee, T., Kim, J., and Chen, P., "Atomistic Nature of Heterointerfaces in III-V Semiconductor-based Quantum-well Structures and Its Consequences for Photoluminescence Behavior," Physical Review B, **36**, pp. 1662-1672, 1987.

Rolland, C., Moore, R., Shepherd, F., and Hillier, G., "10 Gbit/s, 1.56 μm Multiquantum Well InP/InGaAsP Mach-Zehnder Optical Modulator," Electronics Letters, **29**, pp. 471-472, 1993.

Sanders, G. and Chang, Y., "Effect of Band Hybr idization on Exciton States in GaAs-AlGaAs Quantum Wells," Physical Review B, **32**, pp. 5517-5520, 1985.

Sanders, G. and Chang, Y., "Optical Properties in Modulation-doped GaAs-GaAlAs Quantum Wells," Physical Review B, **31**, pp. 6892-6895, 1985.

Sanders, G. and Bajaj, K., "Electronic Properties and Optical-Absorption Spectra of GaAs-AlGaAs Quantum Wells in Externally Applied Electric Fields," Physical Review B, **35**, pp. 2308-2320, 1987.

Sato, K., Wakita, K., and Yamamoto, M., "Strained InGaAsP Multiquantum Wells for Optical Electroabsorption Waveguide Modulators," Electronics Letters, **28**, pp. 609-610, 1992.

Schubert, E., Gobel, E., Horikoshi, Y., Ploog, K., and Queisser, H. , "Alloy Broadening in Photoluminiscence Spectra of AlGaAs," Physical Review B, **30**, pp. 813-820, 1984.

Schubert , E. and Tsang, W., "Photoluminescence Line Shape of Excitons in Alloy Semiconductors," Physical Review B, **34**, pp. 2991-2294, 1986.

Shinada, M. and Sugano, S., "Interband Optical Transitions in Extremely Anisotropic Semiconductors, I. Bound and Unbound Exciton Absorption," Journal of the Physics Society of Japan, **21**, pp. 1938-1946, 1965.

Singh, J. and Bajaj, K., "Theory of Excitonic Photoluminescence Linewidth in Semiconductor Alloys," Applied Physics Letters, **44**, pp. 1075-1077, 1984.

Singh, J. and Bajaj, K., "Role of Interface Roughness and Alloy Disorder in Photoluminescence in Quantum-well Structures," Journal of Applied Physics, **57**, pp. 5433-5437, 1985.

Singh, J., "Theory of Photoluminescence in Quantum Wells in the Presence of Transverse Electric Field: Monte Carlo Approach," Journal of Applied Physics, **59**, pp. 2953-2957, 1986.

Singh, J. and Bajaj, K., "Quantum Mechanical Theory of Linewidths of Localized Radiative Transitions in Semiconductor Alloys," Applied Physics Letters, **48**, pp. 1077-1079, 1986.

Singh, J. and Hong, S., "Theory of Electric Field-Induced Optical Modulation in Single and Multiquantum Well Structures Using a Monte Carlo Approach," IEEE Journal of Quantum Electronics, **QE-22**, pp. 2017-2021, 1986.

Stevens, P., Whitehead, M., Parry, G., and Woodbridge, K., "Computer Modeling of the Electric Field Dependent Absorption Spectrum of Multiple Quantum Well Material," IEEE Journal of Quantum Electronics, **24**, pp. 2007-2015, 1988.

Sugawara, M., Fujii, T., Kondo, M., Kato, K., Domen, K., Yamazaki, S., and Nakajima, K., "Evaluation of Exciton Absorption Peak Broadening Factors in InGaAsP/InP Multiple Quantum Wells," Applied Physics Letters, **53**, pp. 2290-2292, 1988.

Sugawara, M., Fujii, T., Yamazaki, S., and Nakajima, K., "Room Temperature Exciton Optical Absorption Peaks in InGaAsP/InP Multiple Quantum Wells," Applied Physics Letters, **54**, pp. 1353-1355, 1989.

Sugawara, M., Fujii, T., Yamazaki, S., and Nakajima, K., "Theoretical and Experimental Study of the Optical-Absorption Spectrum of Exciton Resonance in InGaAs/InP Quantum Wells," Physical Review B, **42**, pp. 9587-9507, 1990.

Sugawara, M., Fujii, T., Yamazaki, S., and Nakajima, K., "Optical Characteristics of Excitons in InGaAsP/InP Quantum Wells," Physical Review B, **44**, pp. 1782-1791, 1991.

Utaka, K., Suematsu, Y., Kobayashi, K., and Kawanishi, H., "GaInAsP/InP Integrated Twin-Guide Lasers with First-Order Distributed Bragg Reflectors at 1.3 μm Wavelength," Japanese Journal of Applied Physics, **19**, pp. L137-L140, 1980.

Weiner, J., Miller, D., Chemla, D., "Quadratic Electro-Optic Effect Due to the Quantum-Confined Stark Effect in Quantum Wells," Applied Physics Letters, **50**, pp. 842-844, 1987.

Welch, D., Wicks, G., and Eastman, L., "Luminescence Line Shape Broadening Mechanisms in GaInAs/AlInAs Quantum Wells," Applied Physics Letters, **46**, pp. 991-993, 1985.

Woo, J., Rhee, S., Kim, Y., Ko, H., Kim, W., and Kim, D., "Bimodal Roughness of Heterointerface in Quantum Wells Analyzed by Photoluminescence Excitation Spectroscopy," Applied Physics Letters, 66, pp. 338-340, 1995.

Wu, J. and Nurmikko, A., "Stark Shifts on Exciton Luminescence in Quantum Wells: Effect of Coulomb Interaction," Physical Review B, **36**, pp. 4902-4905, 1987.

Yamada, E., Wakita, K., and Nakazawa, M., "30 GHz Pulse Train Generation From a Multiquantum Well Electroabsorption Intensity Modulator," Electronics Letters, **29**, pp. 845-847, 1993.

Zucker, J., Bar-Joseph, I., Miller, B., Koren, U., and Chemla, D., "Quaternary Quantum Wells for Electro-optic Intensity and Phase Modulation at 1.3 and 1.55 μm," Applied Physics Letters, **54**, pp. 10-12, 1989.